

FIRST-PRINCIPLES COMPUTATION OF  
PHONON-LIMITED CARRIER TRANSPORT IN  
SEMICONDUCTORS

Dissertation présentée en vue de l'obtention du grade de  
Docteur en Sciences de l'Ingénieur

ROMAIN CLAES

SUPERVISORS:

Prof. Geoffroy Hautier

Prof. Gian-Marco Rignanese

MEMBERS OF THE JURY:

Dr. Alex Ganose

Prof. Alexandra Zevalkink

Prof. Yaroslav Filinchuk

Prof. Samuel Poncé (secretary)

Prof. Xavier Urbain (chairperson)



Institute of Condensed Matter  
and Nanosciences

Janvier 2024



## ABSTRACT

---

The electronic transport field is rapidly expanding, driven by its fundamental and practical significance in numerous modern technologies. Over the past decades, significant advancements have positioned theoretical approaches as crucial tools in the field, enabling the exploration of both established and novel systems and thus accelerating the discovery of new materials. However, it is imperative to rely on an accurate *ab initio* description of these properties, which are influenced by a multitude of underlying mechanisms. In this thesis, our primary focus has been on intrinsic carrier transport resulting from electron-phonon scattering. To perform high accuracy computations based on the Boltzmann transport formalism, we develop a workflow infrastructure within the Abinit software, enabling one of the pioneering high-throughput studies of carrier mobility based on first-principles. Going beyond the material screening aspect of this work, we also undertake a comprehensive review of the main approximations employed in this formalism over the last decade, highlighting how these simplifications can introduce significant errors.

In a second stage, we delve into specific systems, including the thermoelectric material  $\text{Ca}_5\text{In}_2\text{Sb}_6$ , the transparent conductive material  $\text{CuI}$ , and the tin (II) oxides family. These investigations provide insights into the unique electronic behaviour of these materials, offering potential avenues for enhancing their properties. Notably, the study of the Zintl material  $\text{Ca}_5\text{In}_2\text{Sb}_6$  reveals a decoupling between electronic and thermal transport, a very interesting behaviour for thermoelectric applications. In  $\text{CuI}$ , one of the earliest discovered transparent conductors, we predict a theoretical upper limit to hole mobility for different carrier concentration ranges, implying potential improvements in the experimental results. Finally, we show the potential for high hole mobilities in several ternary tin (II) oxides. We also highlight the significant role of specific vibrational modes in the scattering of carriers, thereby paving the way for new avenues in structural engineering to mitigate their impact.



## ACKNOWLEDGMENTS

---

I want to convey my heartfelt appreciation to all the individuals who played a crucial role in this journey without whom I would not have successfully made it through my Ph.D. program.

En premier lieu, je tiens à exprimer mes sincères remerciements à mes promoteurs, Geoffroy Hautier et Gian-Marco Rignanese. Merci Geoffroy d'avoir été présent dès les premiers pas de ma carrière scientifique, en m'offrant l'opportunité de réaliser ce stage déterminant qui m'a orienté de manière définitive vers ce que je désignais encore à l'époque comme "la chimie théorique". Merci à toi également Gian de m'avoir offert ton soutien à mi-chemin de ce doctorat et pour ton implication et tes nombreux conseils dans mes différents projets. Votre support ainsi que nos nombreuses discussions scientifiques ont été un réel moteur durant ces 4 années.

J'aimerais également remercier particulièrement Guillaume. Merci d'avoir été pour moi comme un second/troisième promoteur durant à la fois mon mémoire et ma thèse. Toujours disponible pour mes questions mais également pour une bonne bière, je suis content désormais de pouvoir te compter comme un ami! Special thanks also to Matteo who has helped me a lot during my thesis and was always available to discuss my various projects.

I would also like to sincerely thank Alex Ganose, Alexandra Zevalkink, Samuel Poncé, Yaroslav Filinchuk and Xavier Urbain for accepting to be members of my thesis committee. I'm looking forward for your feedbacks, comments and questions on such a long text. Thanks in advance for your time.

Next, I would like to thank all my colleagues and staff members from the MODL lab. First, Vinciane, for his support over these 4 years. If they only knew how many administrative formalities we had to go through... and you were always happy to help me, thank you for that! A big thanks also to Pierre-Paul, Julien, Alexandre, Victor, Giuliana, Yuqing, Henrico, Laura, Sadia, Jean-Michel, Bénédicte, Bogdan, Sam, Benoit, Henrique, Matteo, Volodia, Vishank, Maksim, Aurélie, Francesco's, Guido, Viet-Anh, Viet-Hung, Jean-Christophe, Xavier, Samuel, David, Simon, Carina, Janine, Adam, Aurélien, Nicolas, Wei, Anna, Sergio, George, Martha, Tushar, Louis, Josja, Yasmine,

Diana, Jiaqi, Thomas, Vasili, Marie-Rose, Rashmi, Ana, Hao, Maryam, Matthew, Arsalan, Samare (I hope I haven't forgotten anyone). Thank you for the discussions, conferences, minifoot matches, lunches, group meetings (and after-group meetings), beers or ribs at the Blackfriars or elsewhere, and of course for all the memories.

I would also like to thank all the members of the Hautier's group at Dartmouth: Louis (une petite fraiche au Pigeon quand tu veux), Andrew, Dylan, Yihuang, Stephan, Zhenkun, Shay, Weiru and Victor. My time at Dartmouth was memorable thanks to you.

J'aimerais également remercier ma famille pour son soutien pendant ce doctorat mais également pendant ces longues études. Merci pour votre confiance malgré les débuts difficiles. Enfin, un grand merci aux différentes personnes qui ont partagé mon quotidien pendant ces 4 années avec tout ces bons moments: Nathalie, Chloé, Louis, Lilou, Thibault Baquet, Victor, Maiëlle et bien entendu Martin et Laura (1F31D,1F618).

## PUBLICATIONS

---

All the publications authored during this PhD thesis are listed below with my contribution, ordered by publication date.

- D. M. Smiadak, **R. Claes**, N. Perez, M. Marshall, W. Peng, W. Chen, G. Hautier, G. Schierning and A. Zevalkink, Quasi-1D electronic transport and isotropic phonon transport in the Zintl  $\text{Ca}_5\text{In}_2\text{Sb}_6$ , *Materials Today Physics* **22**, 100597 (2022)  
Contributions: theoretical computations and investigations, writing of the computational part, review and editing.
- **R. Claes**, G. Brunin, M. Giantomassi, G.-M. Rignanese and G. Hautier, Assessing the quality of relaxation-time approximations with fully-automated computations of phonon-limited mobilities, *Physical Review B* **106**, 094302 (2022)  
Contributions: conceptualisation, formal analysis, investigation, writing - original draft, writing - review and editing, visualisation, supervision. (co-first author)
- H. Wang, Y. Xiong, H. Padma, Y. Wang, Z. Wang, **R. Claes**, G. Brunin, L. Min, R. Zu, M. T. Wetherington, Y. Wang, Z. Mao, G. Hautier, L.-Q. Chen, I. Dabo and V. Gopalan, Strong electron-phonon coupling driven pseudogap modulation and density-wave fluctuations in a correlated polar metal, *Nature Communications* **14**, 5769 (2023)  
Contributions: theoretical investigations of the electron-phonon coupling, review.
- J. Willis, **R. Claes**, Q. Zhou, M. Giantomassi, G.-M. Rignanese, G. Hautier, Limits to hole mobility and doping in Copper Iodide, *Chemistry of Materials* **35**, 8995 (2023)  
Contributions: conceptualisation, formal analysis, investigation, writing - original draft, writing - review and editing, visualisation, supervision.
- J. He, L. Alaerts, Y. Wang, V. Trinquet, S. Yoshida, H. Yennawar, V. Sanni, **R. Claes**, R. Katzbaer, E. Krysko, S. Sarker, R. Schaak, G.-M. Rignanese, G. Hautier, Z. Mao, V. Gopalan, Computationally

driven discovery of second harmonic generation in  $\text{EuBa}_3(\text{B}_3\text{O}_6)_3$  through inversion symmetry breaking, *accepted*

Contributions: computation of the phonon band structures, review.

- Z. Yuan, D. Dahliah, A. Pike, Y. Xiong, **R. Claes**, G. Kassa, V. Kyveryga, P. Yox, M. R. Hasan, G.-M. Rignanese, C. Chandler, I. Dabo, S. Quadir, A. Zakutayev, D. Fenning, O. G. Reid, S. Bauers, J. Liu, K. Kovnir, G. Hautier, Discovery of the zintl-phosphide  $\text{BaCd}_2\text{P}_2$  as a long carrier lifetime and stable solar cell absorber, *in review*

Contributions: computation of the transport properties, orbital analysis, review.

- **R. Claes**, S. Poncé, G.-M. Rignanese and G. Hautier, Phonon-limited electronic transport through first principles (a review), *in preparation*
- **R. Claes**, G.-M. Rignanese and G. Hautier, Potential new state-of-the-art p-type conductive semiconductor in tin (II) oxides, *in preparation*

## CONTENTS

---

Introduction	1
1 Phonon-limited transport	9
1.1 Drude model . . . . .	10
1.2 Boltzmann Transport Equation (BTE) . . . . .	12
1.2.1 Approximations to the BTE . . . . .	16
1.2.2 Interpolation schemes, dipoles and quadrupoles .	19
1.2.3 Automated calculations . . . . .	20
1.2.4 Approximations versus iterative BTE . . . . .	22
1.2.5 Empirical models . . . . .	29
1.3 Future work . . . . .	31
1.3.1 Hall transport . . . . .	31
1.3.2 Ionised impurity scattering . . . . .	33
1.3.3 Improvement of the workflow . . . . .	33
1.4 Conclusion . . . . .	34
2 Quasi-1D electronic transport and isotropic phonon transport in the Zintl $\text{Ca}_5\text{In}_2\text{Sb}_6$	37
2.1 Crystal and Electronic Structure . . . . .	38
2.2 Carrier charge transport . . . . .	41
2.3 Evidence for isotropic lattice thermal conductivity . . . .	44
2.4 Single crystals measurements . . . . .	47
2.5 Conclusion . . . . .	49
3 Limits to Hole Mobility in Copper Iodide	53
3.1 Crystal and Electronic Structure . . . . .	55
3.2 Charge Transport . . . . .	58
3.2.1 IBTE . . . . .	59
3.2.2 AMSET . . . . .	61
3.2.3 Combined approach . . . . .	65
3.3 Conclusion . . . . .	69
4 Potential new state-of-the-art p-type materials in tin (II) oxides	71
4.1 Crystal structures . . . . .	72
4.2 Decomposition of the scattering rates . . . . .	73
4.3 Transport . . . . .	75
4.3.1 SnO . . . . .	75
4.3.2 Other $\text{Sn}^{2+}$ . . . . .	81
4.4 Conclusion . . . . .	92

Conclusion	93
A Computational details	97
A.1 Details about the transport implementation in Abinit . .	97
A.2 Additional details about the workflow . . . . .	97
A.3 Quasi-1D electronic transport and isotropic phonon trans- port in the Zintl $\text{Ca}_5\text{In}_2\text{Sb}_6$ . . . . .	99
A.4 Limits to Hole Mobility in Copper Iodide . . . . .	99
A.5 Potential new state-of-the-art p-type materials in tin (II) oxides . . . . .	101
B Additional results & figures	103
B.1 High-throughput study . . . . .	103
B.1.1 Numerical results . . . . .	103
B.1.2 Additional figures . . . . .	106
B.2 Potential new state-of-the-art p-type materials in tin (II) oxides . . . . .	109
Bibliography	115

## LIST OF FIGURES

---

Figure 1	Schematic view of the energy bands in metals, semiconductors and insulators. . . . .	2
Figure 2	Schematic of the ideal transmittance with a transparent window over the entire visible spectrum. . . . .	3
Figure 3	Thermoelectric module for power generation through the Seebeck effect with a schematic diagram showing the influence of the carrier concentration on $zT$ and its related parameters. . . . .	5
Figure 1.1	Schematic representation of different scattering mechanisms in a solid. . . . .	11
Figure 1.2	Temperature dependence of mobilities in $n$ -type Si and Ge for different impurities concentrations. . . . .	12
Figure 1.3	Schematic representation of the different possible transitions due to the absorption or emission of a phonon. . . . .	15
Figure 1.4	Electron mobility with respect to the $\mathbf{k}$ - and $\mathbf{q}$ -points grids in ZnO and SnO <sub>2</sub> illustrating the effect of quadrupoles. . . . .	21
Figure 1.5	Flowchart illustrating the workflow used to automatically compute phonon-limited mobilities. . . . .	22
Figure 1.6	Carrier mobility comparison between the CRTA, SERTA and MRTA and the IBTE. . . . .	24
Figure 1.7	Absolute percentage errors of the CRTA, SERTA and MRTA in comparison with the IBTE . . . . .	26
Figure 1.8	Influence of the temperature on the electron mobility results for 3 selected materials using the MRTA, SERTA and IBTE approaches. . . . .	28
Figure 1.9	Influence of the temperature on the hole mobility results for CsAu using the MRTA, SERTA and IBTE approaches. . . . .	29
Figure 2.1	Unit cell of Ca <sub>5</sub> In <sub>2</sub> Sb <sub>6</sub> . . . . .	39
Figure 2.2	Band structure of Ca <sub>5</sub> In <sub>2</sub> Sb <sub>6</sub> . . . . .	40
Figure 2.3	Fermi surface of Ca <sub>5</sub> In <sub>2</sub> Sb <sub>6</sub> . . . . .	41
Figure 2.4	Computed and experimental mobilities for polycrystalline Ca <sub>5</sub> In <sub>2</sub> Sb <sub>6</sub> . . . . .	43

Figure 2.5	Computed and experimental Seebeck coefficient for polycrystalline $\text{Ca}_5\text{In}_2\text{Sb}_6$ . . . . .	44
Figure 2.6	Computed electronic thermal conductivity for polycrystalline $\text{Ca}_5\text{In}_2\text{Sb}_6$ . . . . .	45
Figure 2.7	Computed and experimental $zT$ for polycrystalline $\text{Ca}_5\text{In}_2\text{Sb}_6$ . . . . .	46
Figure 2.8	Phonon dispersion of $\text{Ca}_5\text{In}_2\text{Sb}_6$ with mode Grüneisen parameters. . . . .	47
Figure 2.9	Computed mode Grüneisen parameters as a function of the wavevector. . . . .	48
Figure 2.10	Computed and experimental resistivity for single crystal of $\text{Ca}_5\text{In}_2\text{Sb}_6$ . . . . .	49
Figure 3.1	Zinblende crystal structure of CuI. . . . .	55
Figure 3.2	Electronic band structure of CuI. . . . .	56
Figure 3.3	Schematic molecular orbital diagram of CuI. . . . .	57
Figure 3.4	Top of the valence bands of CuI around $\Gamma$ with and without SOC. . . . .	58
Figure 3.5	Effect of the SOC on the phonon dispersion and hole mobility in CuI . . . . .	60
Figure 3.6	CuI phonon dispersion computed with SOC and the related spectral decomposition of the hole scattering rates. . . . .	61
Figure 3.7	Atomic displacements of CuI corresponding to the longitudinal optical phonon mode at $\Gamma$ . . . . .	62
Figure 3.8	CuI hole mobility against T computed with different methods. . . . .	62
Figure 3.9	CuI hole mobility as a function of temperature at two carrier concentrations. . . . .	63
Figure 3.10	Experimental and computed hole mobility as a function of carrier concentration. . . . .	67
Figure 4.1	Schematic molecular orbital diagram of SnO with the contribution of the ternary atom for the other systems . . . . .	73
Figure 4.2	Crystal structures (conventional cell) of SnO, $c\text{-K}_2\text{Sn}_2\text{O}_3$ , $\text{Rb}_2\text{Sn}_2\text{O}_3$ and $\text{TiSnO}_3$ . . . . .	74
Figure 4.3	IBTE hole drift mobility of SnO against temperature compared with experimental results. . . . .	77
Figure 4.4	Hole linewidths and the two parameters resulting from the linewidths decomposition ( $J$ and $G^2$ ) near the VBM of SnO . . . . .	79

Figure 4.5	IBTE hole drift mobility in SnO as a function of the temperature showing the change in the temperature trend around 100K. . . . .	80
Figure 4.6	SnO phonon dispersion with the related PDOS and spectral decomposition of the scattering rates	81
Figure 4.7	Schematic view of the different transitions possible from two initial states located at two different energy. . . . .	82
Figure 4.8	Principal atomic displacements that couple with the holes in SnO and the related -COHP and DOS due to these phonon modes . . . . .	83
Figure 4.9	Hole linewidths, $G^2$ parameters and $J$ parameters of the different $\text{Sn}^{2+}$ . . . . .	85
Figure 4.10	Fermi surface of $c\text{-K}_2\text{Sn}_2\text{O}_3$ at an energy close to the VBM showing the different pockets that allow intervalley transitions. . . . .	86
Figure 4.11	The function $-v_{\text{VB}}^2 \tau_{\text{VB}} \frac{\partial f}{\partial \epsilon}$ , convoluted with $\delta(\epsilon - \epsilon_{\text{VB}})$ in the valence band for the different materials studied in this work. . . . .	87
Figure 4.12	Phonon dispersion and modes analysis in $c\text{-K}_2\text{Sn}_2\text{O}_3$ . . . . .	88
Figure 4.13	Phonon dispersion and modes analysis in $r\text{-K}_2\text{Sn}_2\text{O}_3$ . . . . .	89
Figure 4.14	Phonon dispersion and modes analysis in $\text{Rb}_2\text{Sn}_2\text{O}_3$	90
Figure 4.15	Phonon dispersion and modes analysis in $\text{TiSnO}_3$	91
Figure A.1	Flowchart illustrating the workflow used to automatically compute phonon-limited mobilities. . .	98
Figure B.1	Mobility wall-time for all materials in the high-throughput study . . . . .	106
Figure B.2	Relative change between the SERTA/MRTA and the IBTE against well-known cheap material descriptors (i.e., the effective mass $m_e$ , the static and high-frequency dielectric constants $\epsilon_0$ and $\epsilon_\infty$ , and the maximum LO frequency $\omega_{\text{LO}}$ ). . . .	107
Figure B.3	Relative change between the SERTA/MRTA and the IBTE against well-known cheap material descriptors (i.e., the average atomic mass, the Debye temperature $T_{\text{D}}$ , the Fröhlich constant $\alpha_{\text{F}}$ and the total number of pockets taken into account in our calculations $N_c$ or $N_v$ ). . . . .	108

Figure B.4	Electronic band structure of SnO. . . . .	109
Figure B.5	Electronic band structure of $c$ -K <sub>2</sub> Sn <sub>2</sub> O <sub>3</sub> . . . . .	110
Figure B.6	Electronic band structure of $r$ -K <sub>2</sub> Sn <sub>2</sub> O <sub>3</sub> . . . . .	110
Figure B.7	Electronic band structure of Rb <sub>2</sub> Sn <sub>2</sub> O <sub>3</sub> . . . . .	111
Figure B.8	Electronic band structure of TiSnO <sub>3</sub> . . . . .	111
Figure B.9	Convergence of the IBTE hole mobility as a function of the $\mathbf{k}$ - and $\mathbf{q}$ -point grids in SnO. . . . .	112
Figure B.10	Convergence of the IBTE hole mobility as a function of the $\mathbf{k}$ - and $\mathbf{q}$ -point grids in $c$ -K <sub>2</sub> Sn <sub>2</sub> O <sub>3</sub> . . . . .	112
Figure B.11	Convergence of the IBTE hole mobility as a function of the $\mathbf{k}$ - and $\mathbf{q}$ -point grids in $r$ -K <sub>2</sub> Sn <sub>2</sub> O <sub>3</sub> . . . . .	113
Figure B.12	Convergence of the IBTE hole mobility as a function of the $\mathbf{k}$ - and $\mathbf{q}$ -point grids in Rb <sub>2</sub> Sn <sub>2</sub> O <sub>3</sub> . . . . .	113
Figure B.13	Convergence of the IBTE hole mobility as a function of the $\mathbf{k}$ - and $\mathbf{q}$ -point grids in TiSnO <sub>3</sub> . . . . .	114

## ACRONYMS

---

BTE	Boltzmann Transport Equation
BZ	Brillouin zone
CB	Conduction band
CBM	Conduction band minimum
CMOS	Complementary metal-oxide-semiconductors
CRTA	Constant Relaxation Time Approximation
DFPT	Density-functional perturbation theory
DFT	Density-functional theory
E-ph	Electron-phonon
EPA	Electron-phonon averaged
FET	Field-effect transistor
FoM	Figure-of-merit
GGA	Generalised-gradient approximation
IBTE	Iterative Boltzmann Transport Equation
ITO	Indium tin oxide
KS	Kohn-Sham
LO	Longitudinal optical
ML	Machine Learning
MLWF	Maximally localised Wannier function
MRTA	Momentum Relaxation Time Approximation
NEGF	Non-Equilibrium Green's Function
RTA	Relaxation Time Approximation

SERTA Self-Energy Relaxation Time Approximation

SKW Shankland-Koelling-Wood

SOC Spin-orbit coupling

TCM Transparent conducting material

TCO Transparent conductive oxide

TO Transverse optical

VB Valence band

VBM Valence band minimum

## INTRODUCTION

---

Materials science is a dynamic field that investigates the properties, behaviour, and applications of various materials, each of which plays a unique role in shaping our modern world. Among these materials, three distinct categories stand out: metals, insulators, and semiconductors. These families of materials are defined by their ability to conduct electricity, and they form the foundation of our understanding of electronic materials. Within this triad, semiconductors hold a particularly intriguing position, as they exhibit properties that lie between those of metals and insulators. In fact, a semiconductor is commonly characterised by its electrical resistivity, typically falling within the broad range of  $10^{-2}$  to  $10^9 \Omega \text{ cm}$  [1].

In an isolated atom, the electrons occupy particular and distinct energy levels. However, when two atoms come together to form a covalent bond, the energy levels of these electrons split into two different energy levels and electrons fill them following Pauli's exclusion principle. But as the number of atoms increases, these two levels are themselves subdivided into other very close energy levels and, for infinite number of atoms, a continuous energy band is formed. These bands, corresponding to the energy levels that are allowed to the electrons of the elements forming the solid material, are separated by forbidden energy levels. The electrons occupy energy bands from the lowest levels up to the Fermi energy. The energy range where no electronic states exist is called the band gap and can also be used to differentiate metals, insulators and semiconductors. As depicted in Figure 1, insulators are distinguished by their wide energy band gap, denoting the energy separation between two key bands: the valence band (VB), fully occupied by electrons, and the conduction band (CB), which remains unoccupied. In contrast, metals feature a Fermi energy situated within an incompletely filled energy band linked to an overlap between the VB and the CB. Finally, a semiconductor is often described as an insulator with a relatively narrow band gap, typically not exceeding 3 eV [1]. As a result, the transition from the VB to the CB is possible for thermally excited electrons. Of course, the size of the band gap directly influences the optical properties of semiconductors, leading to a diverse range of potential applications.

In an era marked by the urgent need for sustainable technological solutions, the quest for innovative materials plays a pivotal role in addressing pressing global challenges. In this thesis, the focus will be on two classes of materials: transparent conductors and thermoelectric materials; each contributing significantly to diverse fields with overarching implications for environmental sustainability. On the one hand, transparent conductive materials serve as the backbone for various contemporary technologies, finding applications in touchscreens, solar panels, and flexible electronics for instance. With the relentless march of technology towards ever-smaller and more integrated devices, the demand for transparent conductive materials has surged. Yet, the challenge lies in ensuring that these materials not only meet technological requirements but also align with sustainability goals. The environmental impact of their production, usage, and disposal must be carefully considered to minimise the carbon footprint associated with these critical components. On the other hand, thermoelectric materials emerge as a promising avenue in the pursuit of sustainable energy solutions. Indeed, thermoelectrics have the unique ability to convert waste heat into electricity, presenting a valuable opportunity to harness and re-purpose energy that would otherwise be lost. While the realms of transparent conductive and thermoelectric materials may appear distant at first glance, a unifying factor lies in their shared requirement for high electronic transport properties — the central focus of this thesis.

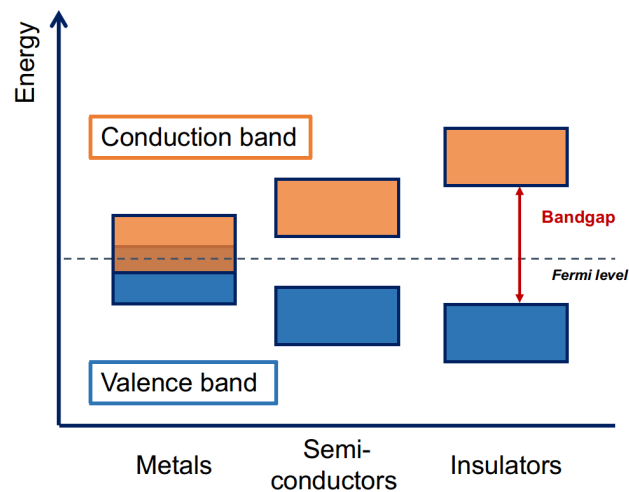


**Figure 1:** Schematic view of the energy bands in metals, semiconductors and insulators.

## TRANSPARENT CONDUCTIVE MATERIALS

Transparent conductive materials (TCMs) are a class of materials that possess the unique combination of an high transparency and high electrical conductivity, two properties typically considered incompatible. In fact, while high conductivity is a characteristic of metallic systems, high transparency is usually associated with insulators that have a wide band gap. Transparency is defined by a band gap exceeding 3.3 eV, ensuring excellent optical transmission in the visible spectrum, spanning from  $\sim 1.60$  to 3.30 eV (equivalent to wavelengths between 380 and 700 nm), as illustrated in Fig. 2. To put it simply, this means that TCMs must allow visible light to pass through without significant absorption. It is therefore essential to minimise the reflection by free carrier but also the absorption by interband optical transition to maximise the transparent window in order to have good TCMs. Nonetheless, the reflection edge is inherently tied to the carrier concentration, which also affects electrical conductivity. Achieving high electrical conductivity necessitates a high carrier concentration but this could lead to the opacity of the material. Therefore, it is often necessary to move the cursor from one side to the other depending on the application [2].

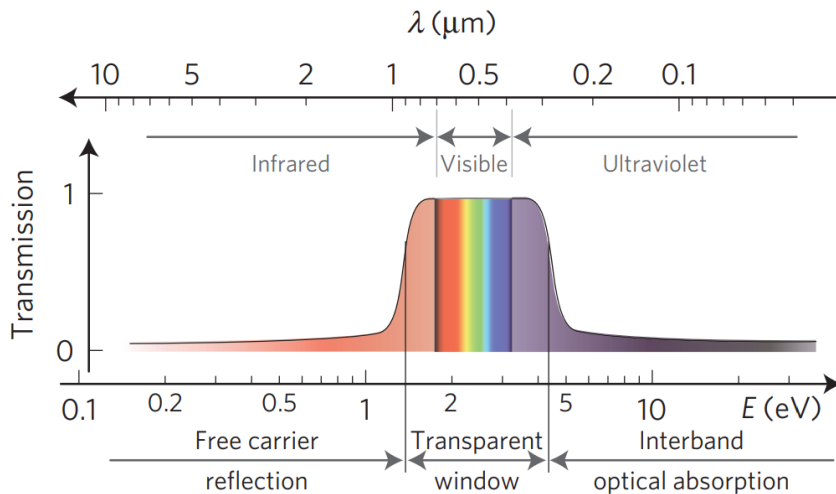


**Figure 2:** Schematic of the ideal transmittance with a transparent window over the entire visible spectrum. Taken from Ref. [2].

The field of TCMs is predominantly governed by oxides (TCOs) with only a few exceptions such as CuI who will be introduced in Chap. 3.

In fact, the TCO market is mainly ruled by *n*-type TCOs (i.e., the charge carriers are electrons) such as indium tin oxide ( $\text{In}_2\text{O}_3$  doped with Sn), commonly referred to as ITO, zinc oxide (ZnO) or tin(IV) oxide ( $\text{SnO}_2$ ) [3–5]. Notably, recent advancements have introduced promising contenders in the field, such as  $\text{BaSnO}_3$ , which displays one of the highest recorded mobilities among TCOs ( $320\text{ cm}^2\text{ V}^{-1}\text{ s}^{-1}$ ) [6], and  $\text{Ga}_2\text{O}_3$  characterised by its wide band gap [7]. Conversely, the availability of good *p*-type TCOs (i.e., the charge carriers are holes) has been limited, primarily attributed to their considerably lower carrier mobility when compared to *n*-type materials. This absence of effective *p*-type materials has significantly diminished the appeal of semiconducting TCOs, as it rendered the formation of *p-n* junctions exclusively from TCOs an unattainable goal. Since *p-n* junctions are essential in the design of various semiconductor devices, the dearth of viable *p*-type TCOs emerges as a substantial impediment [8]. Moreover, other applications such as photovoltaics and solar-cell water-splitting would also greatly benefit from *p*-type electrodes [9, 10]. Currently, the highest mobilities for *p*-type materials are found in SnO [11],  $\text{CuAlO}_2$  [12],  $\text{Ba}_2\text{BiTaO}_6$  [13] or  $(\text{CuS}_2)(\text{Sr}_3\text{Sc}_2\text{O}_5)$  [14], yet they still lag behind their *n*-type counterparts by an order of magnitude. Nonetheless, specific classes of materials hold promise for achieving high mobility *p*-type TCOs. For instance, this is the case of Sn(II) oxides, which will be the central focus of the Chap. 4.

#### THERMOELECTRIC MATERIALS

Thermoelectric materials possess the unique ability to transform a temperature gradient into electricity (and vice versa). In fact, the thermoelectric effect encompasses three phenomena: the Seebeck effect, responsible for converting temperature differences into electricity; the Peltier effect, which involves generating temperature differences with the application of a voltage; and the Thomson effect, which characterises reversible heating or cooling when both a temperature gradient and an electric current are present. In this thesis, we will center our attention on the power generation in the context of energy wasted, and therefore the Seebeck effect.

When a temperature gradient is applied to a thermoelectric material, mobile charge carriers begin to diffuse from the hot to the cold end as shown in Fig. 3(a) [15–17]. This diffusion results in the establishment of an electric field within the material and in either a positive or negative

net charge at the cold end of the material, depending on the majority carrier present [15, 16, 18]. Thermoelectric materials are typically classified using a figure-of-merit (FoM) known as  $zT$ . This FoM depends on the Seebeck coefficient ( $\alpha$ ), which describes the voltage generated when a temperature gradient is applied, as well as the electrical ( $\sigma$ ) and thermal conductivity ( $\kappa$ ) of the material and the temperature ( $T$ ) following:

$$zT = \frac{\alpha^2 \sigma T}{\kappa} = \frac{\alpha^2 \sigma T}{\kappa_l + \kappa_e} \quad (0.1)$$

with  $\kappa_l$  and  $\kappa_e$  the lattice and electrical part of the thermal conductivity, respectively.

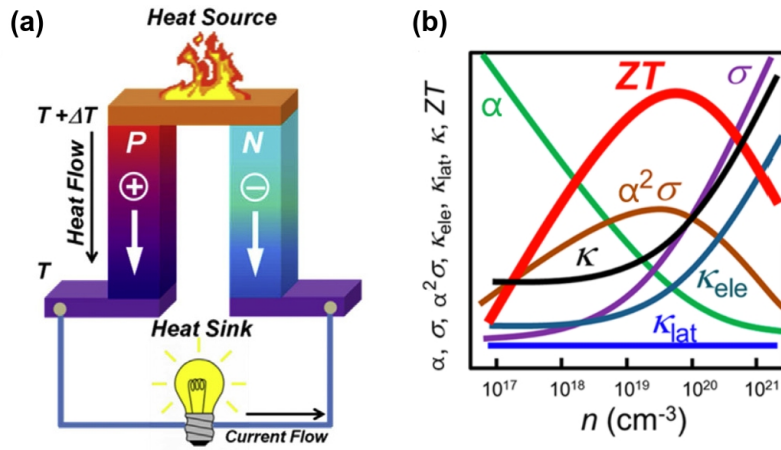


**Figure 3:** (a) Illustration of a thermoelectric module for power generation through the Seebeck effect. Taken from Ref. [15]. (b) Schematic diagram showing the influence of the carrier concentration ( $n$ ) on  $zT$  and its related parameters. Taken from Ref. [19].

In short, for a material to be considered a good thermoelectric, it should possess both a high electrical conductivity to facilitate efficient carrier flow within the material and a high Seebeck coefficient, coupled with low thermal conductivity to maintain a significant temperature gradient between its two ends. Typically, a material is regarded as a good thermoelectric candidate when its  $zT$  value exceeds 1. However, interesting thermoelectrics are difficult to obtain due the strong correlation between these different parameters. For instance, the Wiedemann-

Franz law directly links the electrical conductivity to the electrical part of the thermal conductivity ( $\kappa_e$ ) through the Lorentz number ( $L_0$ ):

$$L_0 = \frac{\kappa_e}{\sigma T}. \quad (0.2)$$

On the other hand, the electrical conductivity increases with the carrier concentration ( $n$ ) which in turn tends to reduce the Seebeck coefficient due to scattering. These different correlations with the carrier concentration are summarised in Fig. 3(b).

The thermoelectric field has long been dominated by a few materials such as PbTe, which still exhibits one of the highest FoM ( $zT = 2.6$ ) [20], or Bi<sub>2</sub>Te<sub>3</sub>, which can operate at lower temperature (around 450K) [21]. In a recent pursuit of environmentally friendly thermoelectric materials, scientists aimed to eliminate Pb and Te from the equation. Notably, chalcogenides based on tin or copper have demonstrated promising outcomes [22–24], exemplified by a FoM exceeding 2 in SnSe at high temperatures (around 1000K). Additional classes of materials, including skutterudites (characterised by a general formula A<sub>y</sub>M<sub>4</sub>X<sub>12</sub> where A represents a positively charged filler atom, M a transition metal, and X a pnictogen atom), chalcopyrites, Mg-based Zintl materials or ionic conductors, have also been investigated with noteworthy results [22, 25–27]. For example, high thermoelectric modules have been successfully obtained by substituting Bi<sub>2</sub>Te<sub>3</sub> with MgAgSb or Mg<sub>3</sub>(Sb,Bi)<sub>2</sub> [22, 28]. In addition, significant progress has also been made through different approaches such as band engineering or structural manipulations in order to directly improve the FoM of these compounds. For instance, band engineering has been realised by introducing point defects in SnTe [29], PbTe [30] or Mg<sub>2</sub>Si [31]. High-performance materials have also been found through composition tuning in the half-Heusler and skutterudite families [16, 32, 33]. Finally, materials exhibiting an anisotropic crystal structure, such as Zintl phases, can offer the potential to effectively decouple thermal and electrical conductivities (see Chap. 2) [26, 34, 35].

#### SCOPE OF THIS WORK

Computing the transport properties of semiconductors plays a pivotal role in comprehending and advancing the development of novel materials across a multitude of applications. This not only offers a promising avenue for material discovery but also serves as an invaluable resource for experimental researchers. It enables them to assess the potential

of a material before embarking on the synthesis process, effectively streamlining their efforts and resources. The first part of this thesis will delve into the methodology employed, with a focus on its automation capabilities that facilitate transport calculations across diverse systems. Specifically, Chap. 1 places a primary emphasis on the Boltzmann transport approach and its associated approximations. This chapter will showcase the workflow developed allowing the automation of transport calculations and present the mobility results for over 50 different materials while assessing the quality of the different approximations to the Boltzmann transport formalism. This also represents one of the pioneering high-throughput studies of transport properties based on first-principles. In the second part of this thesis, a focus is made on specific systems for different applications. In Chap. 2, the thermoelectric properties of a Zintl phase material are computed in order to fit experimental results using an approximation of the Boltzmann transport equation. Through a combination of experimental and theoretical efforts, we successfully demonstrate the quasi-1D electronic transport in the  $\text{Ca}_5\text{In}_2\text{Sb}_6$  Zintl phase. Transitioning to TCMs, Chap. 3 delves into an exploration of the transport properties of CuI, employing both the methodology established in the first chapter and different models. Finally, Chap. 4 centers on an in-depth analysis of hole mobility in multiple tin (II) oxides, with the aim of enhancing our comprehension of the transport phenomena within these materials.



Describing phonon-limited transport remains a complex task, especially when it comes to determining the scattering rates involved. One of the first attempts to address this challenge was made by Bloch in 1929 [36] even before the term "phonons" was coined. He discussed the interaction between the "elastic waves of the lattice" and electrons. From then on, several experimental-based approaches have been developed to further understand the interactions between phonons and electrons. These approaches aim to break down the overall electron-phonon (e-ph) interaction into different contributions, such as acoustic and optical deformation potential scattering or polar optical phonon scattering. In the past two decades, a remarkable advancement has taken place with the emergence of accurate theoretical methods and codes that allow for the computation of electronic transport quantities from first principles, without relying on any experimental parameters. These significant progresses have also enabled researchers to move beyond the simplistic view offered by the Drude model and overcome the limitations associated with working exclusively with single parabolic band systems. All these advancements have opened up unprecedented opportunities to explore and gain a deeper understanding of electronic transport phenomena in materials.

The fundamental physics underlying phonon-limited transport can be described using various methodologies. Most of these methods are based on density-functional theory (DFT) for ground-state properties and density-functional perturbation theory (DFPT) for vibrational properties [37, 38]. The basics of DFT and DFPT can be found in different textbooks [39–41]. After starting with the well-known Drude model (Sec. 1.1), our main focus will revolve around the widely utilised Boltzmann transport formalism (Sec. 1.2), which elucidates the behaviour of charge carriers within a solid as they respond to an applied electric field. In this framework, carriers are characterised as wave packets that follow equations of motion between successive scattering events. Of course, alternative methodologies exist such as the Landauer(-Büttiker) method, which addresses transport as a ballistic problem; the Kubo formalism, which interprets transport in terms of

the material’s linear response to time-dependent external perturbations; and the Non-Equilibrium Green’s Function (NEGF) approach, which is a non-perturbative theory allowing to study dynamical systems far from equilibrium, but they are beyond the scope of this work. The main approximations of the Boltzmann transport formalism are presented in Sec. 1.2.1 and then compared to the exact solution of the Boltzmann transport equation in Sec. 1.2.4. The different strategies of interpolation to obtain the e-ph quantities are discussed in Sec. 1.2.2 and follow by a description of our automated first-principles method to compute the phonon-limited mobility within Abinit (Sec. 1.2.3). This framework allows us to conduct one of the first high-throughput studies of phonon-limited mobility using a first-principles approach. However, these calculations remain rather limited to small systems due to the computational resources needed to obtain accurate results. Consequently, alternative approaches have gained significant traction within the scientific community. The use of empirical models is one of them and is the focus of the Sec. 1.2.5. This chapter is based in part on Ref. [42].

## 1.1 DRUDE MODEL

As electrons and holes are charged particles, they can begin to flow when exposed to an electric field. This motion gives rise to the drift current, which is the fundamental mechanism underlying the electrical conductivity observed in solid materials. The relationship between the current density  $\mathbf{J}$ , the electrical conductivity  $\sigma$ , and the electric field  $E$  is described by the Ohm’s law:

$$\mathbf{J} = \sigma \mathbf{E}. \quad (1.1)$$

Electrical conductivity is a material property that relies on both the mobility of charge carriers within the material  $\mu$ , which indicates how easily electrons can move through the lattice under the influence of an electric field, and the density of charge carriers in the material  $n$ :

$$\sigma = n\mu. \quad (1.2)$$

Through the mobility, the electrical conductivity is directly dependent on the purity, structure and temperature of the crystal. In fact, several mechanisms can scatter the carriers in materials as shown in Fig. 1.1. For instance, impurities, grain boundaries, vacancies are all extrinsic factors

that can scatter the carriers inside a material. On the other hand, e-ph coupling is a crucial intrinsic scattering mechanisms. This means that, in a hypothetical perfect crystal without any defects/impurities, only the interactions of electrons with phonons or other electrons are responsible for the scattering of the carriers and therefore limit the mobility (with the latter having much less impact overall [1]). As depicted in Fig. 1.2, at lower temperatures when lattice vibrations are less pronounced, scattering by defects prevails as the primary mechanism. However, with rising temperature, the number of phonons increases, leading to phonon scattering becoming the dominant mechanism in most semiconductors at room temperature [1, 43]. This is why the focus is made on the phonon-limited mobility in this thesis.

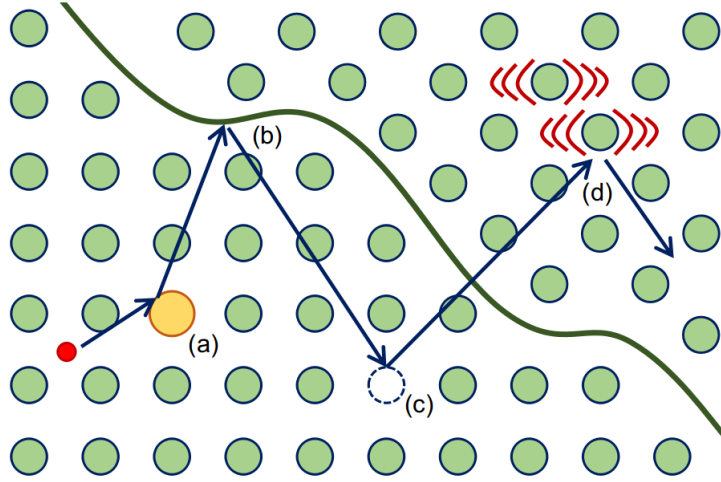


**Figure 1.1:** Schematic representation of different scattering mechanisms in a solid: (a) impurity, (b) grain boundary, (c) vacancy and (d) phonon scattering.

In the Drude model, the carrier mobility is defined by

$$\mu = \frac{e\tau}{m^*}, \quad (1.3)$$

where  $\tau$  is the average lifetime, *i.e.* the time between two scattering events, and  $m^*$  is the effective mass of the carriers. The latter is directly related to the band structure of the material with

$$\frac{1}{m_{\alpha\beta}^*} = \frac{\partial^2 \epsilon}{\partial k_\alpha \partial k_\beta} \quad (1.4)$$

with  $\epsilon$  the band energy and  $\mathbf{k}$  the wavevector.

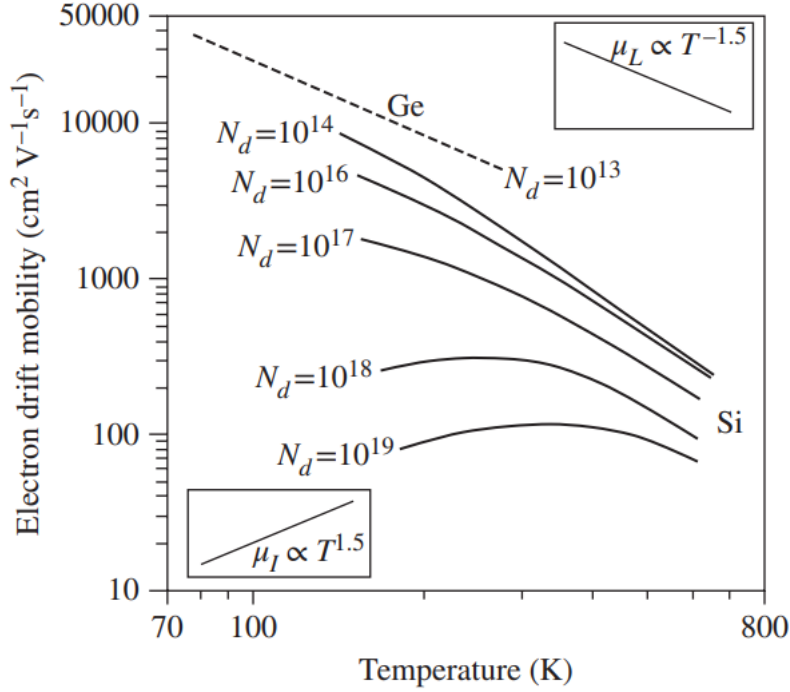


**Figure 1.2:** Temperature dependence of mobilities in *n*-type Si and Ge for different impurities concentrations. The insets show the trend obtained from simple theory for lattice ( $\mu_L$ ) and ( $\mu_I$ ) impurity scattering limited mobility. Taken from Ref. [43].

However, it is important to note that the expressions we have discussed here are tailored specifically for certain cases within the single parabolic band picture. In other words, many materials can not be investigated using the Drude model as they strongly deviate from this simple model. For instance, multiple bands, strong anisotropy or the presence of different pockets in the conduction/valence bands are all examples of phenomenon that are not taken into account. Consequently, it becomes crucial to adopt more versatile approaches such as the Boltzmann Transport Equation described in the next section.

## 1.2 BOLTZMANN TRANSPORT EQUATION (BTE)

Here, we focus on the final equations of the BTE. Their derivation can be found in the following Refs. [44–47]. We consider the case

of electrons only but similar expressions exist for holes. The current density expresses the number of electrons crossing an unit area per unit of time and can be written as

$$J_\alpha = \frac{-1}{\Omega} \sum_{n \in \text{CB}} \int \frac{d\mathbf{k}}{\Omega_{\text{BZ}}} f_{n\mathbf{k}}(\mathbf{E}) v_{n\mathbf{k},\alpha}. \quad (1.5)$$

In this equation,  $f_{n\mathbf{k}}(\mathbf{E})$  is the occupation function of a given state  $n\mathbf{k}$ , where  $n$  is the band index in the conduction band (CB) and  $\mathbf{k}$  the wave vector,  $\Omega$  and  $\Omega_{\text{BZ}}$  refer respectively to the volume of the unit cell and first Brillouin zone (BZ) and,  $\alpha$  stands for the Cartesian coordinates. As electrons are moving in the opposite direction to the current density, the latter takes on a negative sign. Finally,  $v_{n\mathbf{k},\alpha}$  is the velocity of the electrons defined as  $\mathbf{v}_{n\mathbf{k}} = \nabla_{\mathbf{k}} \varepsilon_{n\mathbf{k}}$ , with  $\varepsilon_{n\mathbf{k}}$  the corresponding band structure of the material [44, 45, 48, 49]. As the electron mobility is defined as the derivative of the current with respect to the electric field  $\mathbf{E}$ , we obtain

$$\mu_{e,\alpha\beta} = \frac{-1}{\Omega n_e} \sum_{n \in \text{CB}} \int \frac{d\mathbf{k}}{\Omega_{\text{BZ}}} \left. \frac{\partial f_{n\mathbf{k}}}{\partial E_\beta} \right|_{\mathbf{E}=0} v_{n\mathbf{k},\alpha}, \quad (1.6)$$

where  $n_e$  is the electron concentration. As for the current density, the knowledge of  $f_{n\mathbf{k}}(\mathbf{E})$  is crucial but to evaluate it, several mechanisms need to be taken into account. If we assume a system with no change in temperature and a time-independent electric field, the steady-state solution of  $f_{n\mathbf{k}}(\mathbf{E})$  can be described by three terms: the in- and out-diffusion of the carriers (D), the external forces (F) and the scattering of the carriers (S). As the net change of  $f_{n\mathbf{k}}(\mathbf{E})$  is zero in steady-state, we obtain the Boltzmann transport equation by adding up the different contributions [46, 47]:

$$\frac{\partial f_{n\mathbf{k}}}{\partial t} = 0 = \left( \frac{\partial f_{n\mathbf{k}}}{\partial t} \right)_{\text{D}} + \left( \frac{\partial f_{n\mathbf{k}}}{\partial t} \right)_{\text{F}} + \left( \frac{\partial f_{n\mathbf{k}}}{\partial t} \right)_{\text{S}}. \quad (1.7)$$

In this equation, the change of  $f_{n\mathbf{k}}(\mathbf{E})$  due to carrier diffusion is zero as the distribution function is not space dependent. In the case of external forces (F), we can consider two distinct scenarios: (1) the influence of an electric field only, resulting in the *so-called* drift mobility, and (2) the combined impact of both an electric and a magnetic field, giving rise to the Hall mobility. Here, we will only talk about the drift transport.

The change of  $f_{n\mathbf{k}}(\mathbf{E})$  due to an electric field is defined as [44, 46, 47]

$$\left( \frac{\partial f_{n\mathbf{k}}}{\partial t} \right)_{\text{E}} = -\frac{\partial \mathbf{k}}{\partial t} \cdot \nabla_{\mathbf{k}} f_{n\mathbf{k}} = \mathbf{E} \cdot \nabla_{\mathbf{k}} f_{n\mathbf{k}}. \quad (1.8)$$

Therefore, Eq. (1.7) now becomes

$$-\left(\frac{\partial f_{n\mathbf{k}}}{\partial t}\right)_E = -\mathbf{E} \cdot \nabla_{\mathbf{k}} f_{n\mathbf{k}} = \left(\frac{\partial f_{n\mathbf{k}}}{\partial t}\right)_S. \quad (1.9)$$

Without any electric field, the occupation function  $f_{n\mathbf{k}}(\mathbf{E})$  reduces to the Fermi-Dirac distribution which is defined by  $f_{n\mathbf{k}}^0 = 1/(e^{(\varepsilon_{n\mathbf{k}} - \varepsilon_F)/k_B T} + 1)$ , where  $T$  is the temperature,  $k_B$  is the Boltzmann constant,  $\varepsilon_F$  is the Fermi level, and  $\varepsilon_{n\mathbf{k}}$  is the energy of an electron in the state  $n\mathbf{k}$ . Here, we consider a small electric field which implies that  $f_{n\mathbf{k}}(\mathbf{E})$  is relatively close to the equilibrium Fermi-Dirac distribution. Using the low-field approximation, we can therefore approximate  $\mathbf{E} \cdot \nabla_{\mathbf{k}} f_{n\mathbf{k}}(\mathbf{E}) \approx \mathbf{E} \cdot \nabla_{\mathbf{k}} f_{n\mathbf{k}}^0$ . Using the definition of the velocity, we find

$$\nabla_{\mathbf{k}} f_{n\mathbf{k}}^0 = \frac{\partial f_{n\mathbf{k}}^0}{\partial \varepsilon_{n\mathbf{k}}} \nabla_{\mathbf{k}} \varepsilon_{n\mathbf{k}} = \frac{\partial f_{n\mathbf{k}}^0}{\partial \varepsilon_{n\mathbf{k}}} \mathbf{v}_{n\mathbf{k}} \quad (1.10)$$

and finally, we obtain the linearised Boltzmann transport equation:

$$-\mathbf{E} \cdot \mathbf{v}_{n\mathbf{k}} \frac{\partial f_{n\mathbf{k}}^0}{\partial \varepsilon_{n\mathbf{k}}} = \left(\frac{\partial f_{n\mathbf{k}}}{\partial t}\right)_S. \quad (1.11)$$

In a solid, several mechanisms can take place to scatter the electrons: (1) extrinsic mechanisms such as impurities, defects, or grain boundaries for instance, and (2) intrinsic mechanisms due to, for example, electron-phonon or electron-electron interactions. Here, the focus is made on the intrinsic scattering which does not rely on the quality of the sample studied. It is the most important one at room temperature where the vibrations of the atoms are already significant. Consequently, by using Fermi's golden rule, four processes can take place as shown in Fig. 1.3: an out-of-state transition where electrons in the state  $n\mathbf{k}$  can absorb or emit a phonon  $\omega_{\mathbf{q}\nu}$  to go to the state  $m\mathbf{k} + \mathbf{q}$  or an in-state transition where electrons in the state  $m\mathbf{k} + \mathbf{q}$  can emit or absorb a phonon  $\omega_{\mathbf{q}\nu}$  to go to the state  $n\mathbf{k}$  [44, 45]. The probability that a given phonon allows the transition between 2 states is determined by the

square of the electron-phonon coupling matrix elements,  $g_{mnv}(\mathbf{k}, \mathbf{q})$ . Therefore, Eq.(1.11) becomes [44]

$$\begin{aligned}
-\mathbf{E} \cdot \mathbf{v}_{n\mathbf{k}} \frac{\partial f_{n\mathbf{k}}^0}{\partial \varepsilon} &= 2\pi \sum_{m,\nu} \int_{\text{BZ}} \frac{d\mathbf{q}}{\Omega_{\text{BZ}}} |g_{mnv}(\mathbf{k}, \mathbf{q})|^2 \\
&\times [(1 - f_{n\mathbf{k}})f_{m\mathbf{k}+\mathbf{q}}\delta(\varepsilon_{n\mathbf{k}} - \varepsilon_{m\mathbf{k}+\mathbf{q}} + \omega_{\mathbf{q}\nu})(1 + n_{\mathbf{q}\nu}) \\
&+ (1 - f_{n\mathbf{k}})f_{m\mathbf{k}+\mathbf{q}}\delta(\varepsilon_{n\mathbf{k}} - \varepsilon_{m\mathbf{k}+\mathbf{q}} - \omega_{\mathbf{q}\nu})n_{\mathbf{q}\nu} \\
&- f_{n\mathbf{k}}(1 - f_{m\mathbf{k}+\mathbf{q}})\delta(\varepsilon_{n\mathbf{k}} - \varepsilon_{m\mathbf{k}+\mathbf{q}} - \omega_{\mathbf{q}\nu})(1 + n_{\mathbf{q}\nu}) \\
&- f_{n\mathbf{k}}(1 - f_{m\mathbf{k}+\mathbf{q}})\delta(\varepsilon_{n\mathbf{k}} - \varepsilon_{m\mathbf{k}+\mathbf{q}} + \omega_{\mathbf{q}\nu})n_{\mathbf{q}\nu}],
\end{aligned} \tag{1.12}$$

where  $\delta$  is the Dirac delta function and  $n_{\mathbf{q}\nu}$  is the Bose-Einstein occupation. This Dirac delta function is set to have a value of 0 except when the transition is allowed by energy and momentum conservation. In practice, it is convenient to replace this  $\delta$  distribution by a Lorentzian or a Gaussian using a small broadening parameter, an adaptive broadening [50] or using a linear tetrahedron method as proposed by Blöchl, [51] bypassing the need of a convergence study.

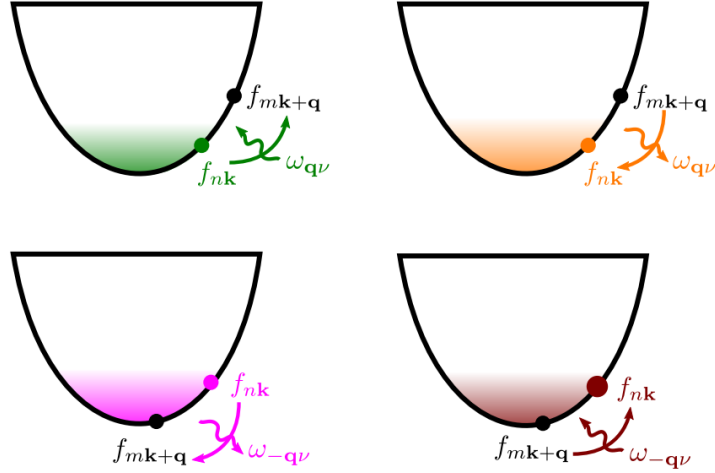


**Figure 1.3:** Out-of-state transition of an electron from a state  $n\mathbf{k}$  to a state  $m\mathbf{k} + \mathbf{q}$  by absorption (in green) or emission of a phonon  $\omega_{\mathbf{q}\nu}$  (in purple) and in-state transition of an electron from a state  $m\mathbf{k} + \mathbf{q}$  to a state  $n\mathbf{k}$  by emission (in orange) or absorption of a phonon  $\omega_{\mathbf{q}\nu}$  (in brown). Taken from Ref. [44].

The matrix elements  $g_{mnv}(\mathbf{k}, \mathbf{q})$  can be expressed as

$$g_{mnv}(\mathbf{k}, \mathbf{q}) = \langle u_{m\mathbf{k}+\mathbf{q}}^{\text{KS}} | \Delta_{\mathbf{q}\nu} V^{\text{KS}} | u_{n\mathbf{k}}^{\text{KS}} \rangle, \tag{1.13}$$

where  $u_{n\mathbf{k}}^{\text{KS}}$  and  $u_{m\mathbf{k}+\mathbf{q}}^{\text{KS}}$  are the Bloch-periodic components of the Kohn-Sham electron wave functions and  $\Delta_{\mathbf{q}\nu} V^{\text{KS}}$  is the phonon-induced vari-

ation of the self-consistent potential experienced by electrons [48, 49, 52]. In other words, if the initial state wave function  $u_{n\mathbf{k}}^{\text{KS}}$  perturbed by the phonon is close to the final state wave function  $u_{m\mathbf{k}+\mathbf{q}}^{\text{KS}}$ , the transition will be likely and therefore  $g_{mnv}(\mathbf{k}, \mathbf{q})$  important. By taking the derivatives of each side of Eq. (1.12) with respect to the electric field  $\mathbf{E}$ , we obtain

$$\begin{aligned} \left. \frac{\partial f_{n\mathbf{k}}}{\partial E_\beta} \right|_{\mathbf{E}=0} &= \frac{\partial f_{n\mathbf{k}}^0}{\partial \varepsilon_{n\mathbf{k}}} v_{n\mathbf{k},\beta} \tau_{n\mathbf{k}}^0 + 2\pi \tau_{n\mathbf{k}}^0 \sum_{m,\nu} \int \frac{d\mathbf{q}}{\Omega_{\text{BZ}}} |g_{mnv}(\mathbf{k}, \mathbf{q})|^2 \\ &\times \left[ (1 + n_{\mathbf{q}\nu} - f_{n\mathbf{k}}^0) \delta(\varepsilon_{n\mathbf{k}} - \varepsilon_{m\mathbf{k}+\mathbf{q}} + \omega_{\mathbf{q}\nu}) \right. \\ &\left. + (n_{\mathbf{q}\nu} + f_{n\mathbf{k}}^0) \delta(\varepsilon_{n\mathbf{k}} - \varepsilon_{m\mathbf{k}+\mathbf{q}} - \omega_{\mathbf{q}\nu}) \right] \left. \frac{\partial f_{m\mathbf{k}+\mathbf{q}}}{\partial E_\beta} \right|_{\mathbf{E}=0}, \end{aligned} \quad (1.14)$$

with the relaxation time  $\tau_{n\mathbf{k}}^0$  defined as

$$\begin{aligned} \frac{1}{\tau_{n\mathbf{k}}^0} &= 2\pi \sum_{m,\nu} \int \frac{d\mathbf{q}}{\Omega_{\text{BZ}}} |g_{mnv}(\mathbf{k}, \mathbf{q})|^2 \times \left[ (n_{\mathbf{q}\nu} + f_{m\mathbf{k}+\mathbf{q}}^0) \delta(\varepsilon_{n\mathbf{k}} - \varepsilon_{m\mathbf{k}+\mathbf{q}} + \omega_{\mathbf{q}\nu}) \right. \\ &\left. + (n_{\mathbf{q}\nu} + 1 - f_{m\mathbf{k}+\mathbf{q}}^0) \delta(\varepsilon_{n\mathbf{k}} - \varepsilon_{m\mathbf{k}+\mathbf{q}} - \omega_{\mathbf{q}\nu}) \right], \end{aligned} \quad (1.15)$$

and Eq. (1.6) can therefore be used to obtain the mobility. However, the main problem in solving Eq. (1.14) lies in the interdependence between  $\frac{\partial f_{n\mathbf{k}}}{\partial E_\beta}$  (initial state  $n\mathbf{k}$ ) and  $\frac{\partial f_{m\mathbf{k}+\mathbf{q}}}{\partial E_\beta}$  (final state  $m\mathbf{k} + \mathbf{q}$ ). This system of linear equations needs to be solved iteratively but, for years, solving the iterative Boltzmann transport equation (IBTE) has been left aside in favour of methods based on approximations due to the lack of implementations [42, 44, 45, 48, 53]. In addition to the iterative BTE solver used here, several alternative exist to solve the BTE exactly such as the variational [54, 55] and relaxons solvers [55] or the Rode iterative method [56, 57].

### 1.2.1 Approximations to the BTE

#### *Constant relaxation-time approximation*

One of the easiest ways to bypass the problem is by making the simplifying assumption that all relaxation times are equal to a constant for all states (i.e.,  $\tau_{n\mathbf{k}} = \tau$ ). This approach, known as the constant relaxation-time approximation (CRTA), fixes the relaxation time  $\tau$  to a specific value, rendering the mobility dependent solely on the band

structure. Consequently, there is no need to calculate the expensive electron-phonon matrix elements, drastically reducing the required computational resources. The CRTA has found widespread applications in various contexts and is, for instance, implemented in the BoltzTrap software [58, 59]. In fact, it has been extensively employed in the past to effectively mimic and comprehend experimental results by fitting the relaxation time to match the experimental data [59–61] (see also Chap. 2) but also in high-throughput studies, enabling the ranking of large sets of materials using a common lifetime, [62–65] (or, equivalently, by evaluating the transport effective mass [4, 66]). While the ranking based on the effective mass or Seebeck coefficient demonstrates a strong correlation with experimental results [63, 67] (as these two parameters are not directly influenced by the carrier lifetime), the ranking based on conductivity/mobility exhibits a considerably weaker alignment with both experimental data [67] and the exact IBTE solution [42]. Therefore, while the CRTA offers computational advantages, it is essential to exercise caution and consider its limitations when interpreting the obtained results. In some materials, anisotropic scattering rates or varying relaxation times across different states could significantly impact the accuracy of the results.

#### *Self-energy relaxation time approximation*

Another way to get rid of the problematic iterative part of Eq. (1.14) is to neglect the second term on the right-hand side. This approach is known as the self-energy relaxation time approximation (SERTA) which simplifies Eq.(1.14) to

$$\frac{\partial f_{nk}}{\partial E_\beta} = \frac{\partial f_{nk}^0}{\partial \varepsilon_{nk}} v_{nk,\beta} \tau_{nk}^0. \quad (1.16)$$

and is equivalent to completely ignoring the effects of scattering back in the state  $n\mathbf{k}$  [45]. By using the SERTA, the electron lifetimes can be computed following Eq. (1.15) and the mobility is directly given by

$$\mu_{e,\alpha\beta}^{\text{SERTA}} = \frac{-e}{\Omega n_e} \sum_{n \in \text{CB}} \int \frac{d\mathbf{k}}{\Omega_{\text{BZ}}} \frac{\partial f_{nk}^0}{\partial \varepsilon_{nk}} v_{nk,\alpha} v_{nk,\beta} \tau_{nk}^0. \quad (1.17)$$

#### *Momentum relaxation-time approximation*

In order to take into account the back-scattering processes, one can also add a geometrical factor favouring forward scattering to the SERTA.

This leads to the *so-called* momentum relaxation-time approximation (MRTA) which is based on two approximations: (i) the linear response coefficients  $\frac{\partial f_{nk}}{\partial E_\beta}$  are taken to possess only a component in the direction of the band velocity, such that the electron lifetimes are defined as scalar quantities, and (ii) the probability of in and out-of-state scattering is assumed to be the same [42, 44, 53, 68]. In this approach, the electron lifetimes are given by

$$\begin{aligned} \frac{1}{\tau_{nk}^0} = & 2\pi \sum_{m,\nu} \int \frac{d\mathbf{q}}{\Omega_{\text{BZ}}} |g_{m\nu}(\mathbf{k}, \mathbf{q})|^2 \left( 1 - \frac{\mathbf{v}_{nk} \cdot \mathbf{v}_{m\mathbf{k}+\mathbf{q}}}{|\mathbf{v}_{nk}|^2} \right) \\ & \times \left[ (n_{\mathbf{q}\nu}^0 + f_{m\mathbf{k}+\mathbf{q}}^0) \delta(\varepsilon_{nk} - \varepsilon_{m\mathbf{k}+\mathbf{q}} + \omega_{\mathbf{q}\nu}) \right. \\ & \left. + (n_{\mathbf{q}\nu}^0 + 1 - f_{m\mathbf{k}+\mathbf{q}}^0) \delta(\varepsilon_{nk} - \varepsilon_{m\mathbf{k}+\mathbf{q}} - \omega_{\mathbf{q}\nu}) \right]. \end{aligned} \quad (1.18)$$

with  $\left( 1 - \frac{\mathbf{v}_{nk} \cdot \mathbf{v}_{m\mathbf{k}+\mathbf{q}}}{|\mathbf{v}_{nk}|^2} \right)$  the efficiency factor that favours forward scattering geometrically in order to take better into account the relative changes in the electron velocity due to the different scattering processes [42, 44, 53, 68]. These lifetimes are then used in the same equation as SERTA (Eq. (1.17)) in order to compute the electron mobility.

#### *Other approximations*

Finally, among the various other approximations, one noteworthy approach is the electron-phonon averaged (EPA) approximation [55, 69]. This method relies on an energy-dependent averaging of phonon energies and a coarse-mesh treatment for the electron-phonon matrix elements. Remarkably, the EPA approximation has shown promising results when applied to half-Heusler compounds in the context of thermoelectric properties [69]. Likewise, EPIC STAR [70] effectively reduces scattering rates by leveraging an energy-dependent averaged scattering rate through a generalised Eliashberg function for short-range e-ph scattering. On the other hand, long-range POP scattering are treated using a first-principles approach, addressing the problematic case where the matrix elements varies rapidly with  $\mathbf{q}$  as it can be the case for POP scattering. Additionally, EPIC STAR offers a model-based approach to tackle impurity scattering [70].

### 1.2.2 Interpolation schemes, dipoles and quadrupoles

Nowadays, the majority of cutting-edge algorithms designed for the computation of electron-phonon (e-ph) quantities using first-principles methodologies offer the option to employ either the iterative approach or approximations [42, 55, 71, 72]. The divergence among these algorithms lies in their strategies for acquiring these e-ph quantities and the specific interpolation techniques they employ. In fact, the main problem in obtaining accurate e-ph mobilities is the need to obtain matrix elements on very dense  $\mathbf{k}$ - and  $\mathbf{q}$ -point grids. One way to reduce the computational cost is to interpolate the e-ph matrix elements using Fourier transforms. For instance, EPW [71, 73], PERTURBO [72] and PHOEBE [55] rely on an interpolation framework that exploits the spatial arrangement of Wannier functions within real space, facilitating the calculation of e-ph matrix elements at a relatively economical computational expense. These maximally localized Wannier functions (MLWFs) are constructed using the Wannier90 code [74, 75]. However, despite substantial advancements in recent times [76–79], the generation of these MLWFs can remain intricate for systems that are more difficult to interpret in terms of chemical orbitals, posing challenges to the automation of material database computations. In contrast, the Abinit [80, 81] software adopts an alternative strategy based on the interpolation of the perturbed potential directly. This approach offers the advantage of circumventing the need for Wannier functions, although demanding more memory and time compared to the Wannier-based approaches. Nevertheless, through the recent implementation of various optimisation techniques [48], it has recently enabled pioneering first-principles medium-throughput explorations of mobility [42].

Regarding the interpolation, the short-range interactions pose no major challenge, as these contributions rapidly approach zero beyond the boundaries of the real-space box. In contrast, handling long-range interactions in semiconductors proves to be more intricate, owing to their connection with non-analyticities as  $\mathbf{q}$  approaches 0. In such cases, Fourier interpolation is inadequate, and specific analytical models must be employed to address these interactions, such as the dipole interaction prevalent in polar materials [37, 82]. Recently, the significance of incorporating dynamical quadrupoles has come to the forefront as a crucial factor in achieving accurate transport results [48, 52, 83, 84]. In contrast to dipoles, which are only present in polar materials, dynamical quadrupoles are non-zero in all noncentrosymmetric crystals,

but also in centrosymmetric ones if one or more atoms are placed at noncentrosymmetric sites, making them important for the computation of transport properties in a lot of materials [48, 52, 83–86]. The effect of these quadrupoles on the mobility typically ranges between 5-6% and 45% depending on the system [85]. As illustrated in Fig. 1.4, the effect of these quadrupoles differs between materials, with a pronounced influence in ZnO, possibly attributed to its strong piezoelectric properties [87, 88], while the effect on SnO<sub>2</sub> is comparatively minimal.

Importantly, when using a Wannier interpolation-based scheme, a Berry connection term appears at the same second-order as dynamical quadrupoles which has been shown to be of similar importance [86, 89]. Finally, we mention that in 2D materials the long-range electrostatics has to be treated carefully [86, 89, 90] and used in conjunction with out-of-plane truncation schemes [91].

### 1.2.3 Automated calculations

The computation of the phonon-limited mobility is a rather complex task involving many steps. It typically requires an important human time and intervention. As a result, its automation was only realised for very specific cases [92]. Our approach, based on the *Abinit* software and detailed in Ref. [48] (or summarised in the App. A.1), takes advantage of (i) the tetrahedron integration scheme to reduce the number of e-ph transitions to be computed<sup>1</sup>, (ii) a Fourier interpolation of the scattering potentials in  $\mathbf{q}$  space including the proper treatment of dipole and quadrupole contributions, and (iii) exact KS wavefunctions that are computed only for the  $\mathbf{k}$ -points lying inside a small energy window around the band edges. To fully automate all the different parts of the computation, including the convergence studies for the BZ sampling, we have developed a workflow within the *AbiPy* python package [93]. The main steps are schematically represented in Fig. 1.5, with more details given in App. A.2. The ingredients needed in Eq. (1.14) are the KS wave functions on the dense mesh for the electronic part (in purple in Fig. 1.5) and the density-functional perturbation theory (DFPT) scattering potentials and the interatomic force constants on a coarse mesh (typical of DFPT, see Ref. [94]) for the phonon part (in

<sup>1</sup> By employing the tetrahedron method, one can effectively pinpoint, for a specified  $\mathbf{k}$ -point, the subset of  $\mathbf{q}$ -points within the IBZ that actively contribute to Eq. (1.15). Theoretically, a comparable optimisation approach can be applied to both Lorentzian and Gaussian broadening techniques.

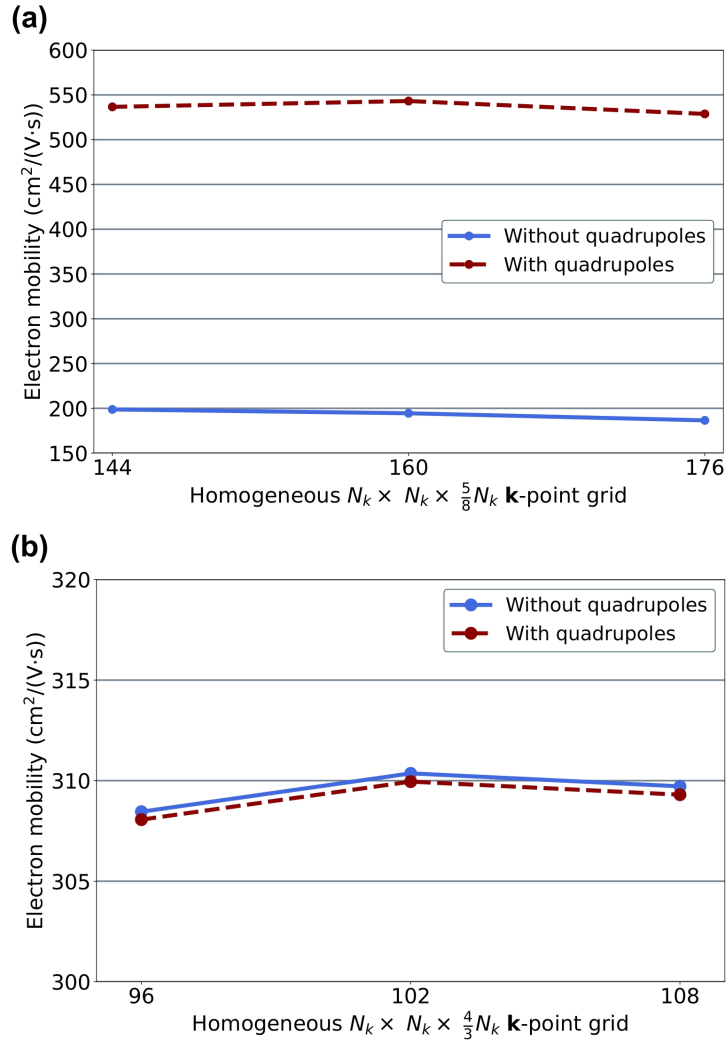


**Figure 1.4:** Convergence (last three points) of the (SERTA) electron mobility with respect to the  $\mathbf{k}$ - and  $\mathbf{q}$ -points grids ( $N_k=N_q$ ) in (a) ZnO and (b) SnO<sub>2</sub> (in the x-direction). The blue lines include only the dipoles contribution to the long-range interaction whereas the red lines include both dipoles and quadrupoles contributions.

blue in Fig. 1.5). The latter can be easily computed with another AbiPy workflow, although it is possible to start from a database of previous DFPT computations [94, 95]. The first step of the workflow consists in a ground-state calculation (in orange in Fig. 1.5), with basic parameters reused from the DFPT database. This allows to determine the wave

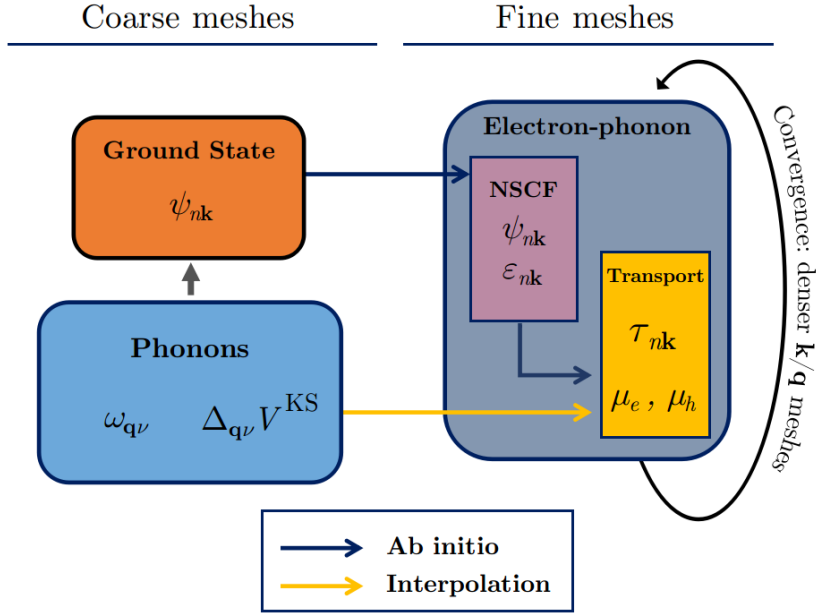


**Figure 1.5:** Flowchart illustrating the workflow used to automatically compute phonon-limited mobilities.

functions on the fine mesh using a two-step procedure described in Ref. [48] and in App. A.2. All the ingredients required to compute the mobility on a given dense mesh are then readily available. Since a convergence study is needed with respect to this dense mesh, we perform the previous steps multiple times for meshes of increasing density. Usually, we choose that the convergence is assumed to be reached when three consecutive grids lead to mobilities maximum 5% away from each other.

#### 1.2.4 Approximations versus iterative BTE

Even though the CRTA, SERTA, and MRTA have been widely used in the literature to characterise the transport of electrons or holes, the validity of such approximations has not yet been tested in a systematic way. Using our automated mobility computations, we are now able to conduct such an analysis. Here, we analyze the phonon-limited transport in 54 different semiconductors, including 54 electron and 13 hole mobilities. This allows us to directly probe the quality of these different approximations to the IBTE. These 54 semiconductors

have been selected by the following procedure. In order to reduce the total computation time, we consider only those semiconductors for which phonon properties are available in the Materials Project database [94, 96] and discard materials with imaginary phonon frequencies (vibrational instabilities) or those that are predicted to be thermodynamically unstable, *i.e.* with an energy above hull larger than 50 meV/atom. The results of Ref. [63] have then been used to remove all materials for which the average transport effective mass is larger than one. Finally, we enforce two additional constraints that are needed in order to be compatible with the previous DFPT calculations performed with PBEsol scalar-relativistic norm-conserving pseudopotentials including non-linear core correction (NLCC) [97]. First, we have considered systems with a single conduction/valence band within an energy window of 0.25 eV above/below the minimum/maximum. The motivation is that spin-orbit coupling (SOC) has been shown to have a significant impact on phonon-limited mobilities [85, 98, 99]. Restricting our database to systems with a single band allows us to avoid the worst-case scenario of degenerate hole states that are split by SOC although it is clear that a proper treatment of relativistic effects in mobility calculations would require the inclusion of SOC effects both at the electronic and vibrational level. Secondly, we have considered only space groups for which the dynamical quadrupoles  $Q^*$  are zero by symmetry<sup>2</sup>. As recently shown in Refs. [48, 52, 83–85], dynamical quadrupoles play a crucial role for obtaining reliable phonon-limited mobilities in semiconductors. Unfortunately, the DFPT computation of  $Q^*$  is presently limited to norm-conserving pseudopotentials without NLCC, hence we decided to restrict the discussion to high-symmetry structures. Overall, our screening criteria led to 54 materials (37 in the  $Fm\bar{3}m$  space group, 16 in  $Pm\bar{3}m$  and one belonging to the tetragonal  $P4/mmm$  space group) and 67 mobilities (54 electron and 13 hole mobilities). Although our dataset mostly consists of cubic systems, we expect our analysis to hold for other structures as well. For the reader’s information, Fig. B.1 displays the different calculation wall-times needed to obtain the carrier mobility with a converged grid for all the materials in our dataset.

Fig. 1.6 shows this comparison of the CRTA (a) and SERTA/MRTA (b) mobilities with the IBTE results for all the systems in our dataset at 300K. The numerical results can be found in Table B.1.1. Obviously, the CRTA mobility for a given material can be made exactly equal to the

<sup>2</sup> Dynamical quadrupoles are non-zero in all non-centrosymmetric crystals, but also in centrosymmetric ones if one or more atoms are placed at non-centrosymmetric sites.

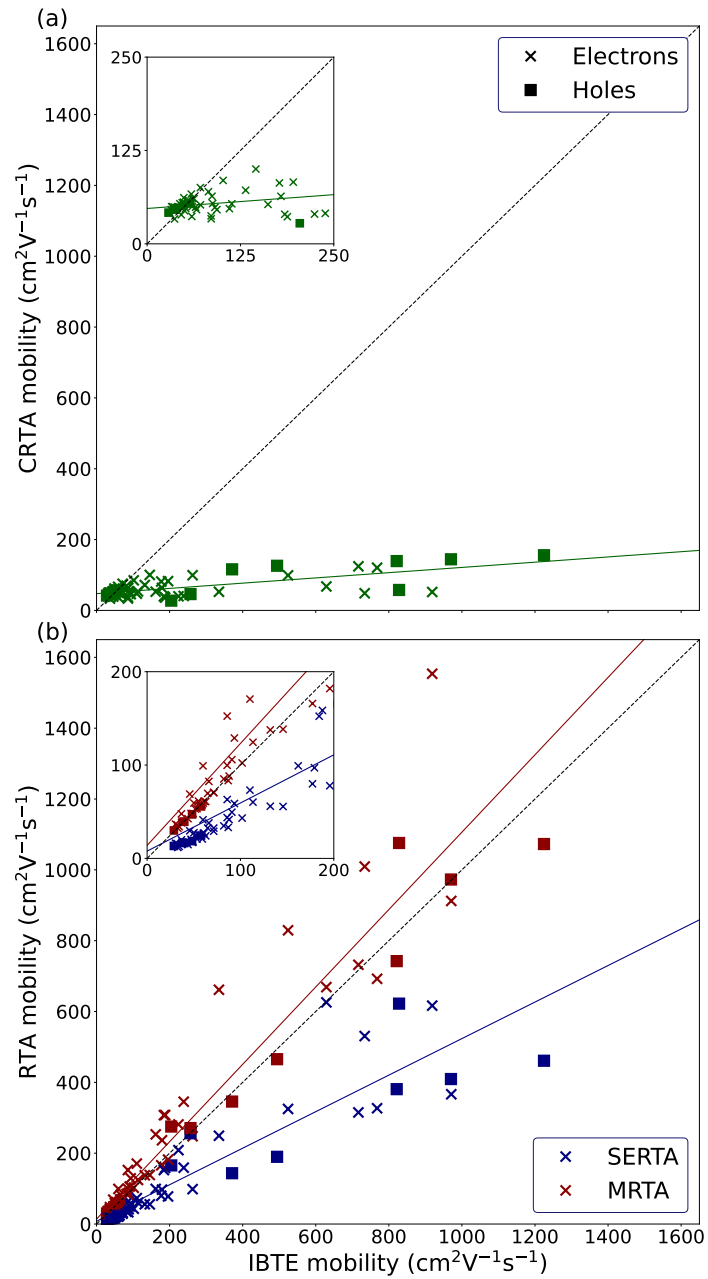


**Figure 1.6:** Comparison of the (a) CRTA, and (b) SERTA, MRTA with the IBTE electron mobilities at 300 K. For the CRTA, the chosen lifetime minimises the mean absolute error. MRTA mobilities are in red whereas SERTA mobilities are in blue. The black dotted lines represent the IBTE results. The green, blue, and red solid lines are linear fits of the CRTA, SERTA, and MRTA results, respectively.

IBTE value by an appropriate choice of  $\tau$  for a specific T. In our dataset, a wide variety of lifetimes would have to be used ranging from 7 fs for CsBr to 188 fs for KMgH<sub>3</sub>. Considering the complete set of materials, a lifetime of 10.6 fs minimises the mean absolute percentage error but, as can be seen from Fig. 1.6(a), the agreement with the IBTE is only valid for low IBTE mobilities, as most of the systems in the dataset have an IBTE mobility lower than  $100 \text{ cm}^2\text{V}^{-1}\text{s}^{-1}$  (see the insets of Fig. 1.6). However, even in this region, a material with a low CRTA mobility may show a large relative error (see Fig. 1.7(a)). It is clear from Fig. 1.6(a) that the correlation is weak between the CRTA and IBTE results. A large (low) CRTA result does not guarantee a large (low) IBTE mobility. One can also compute Spearman's rank correlation coefficient  $\rho$  in order to quantify the ranking capability of CRTA. A value of  $\rho^{\text{CRTA}} = 0.45$  is obtained, indicating that the CRTA is overall not able to correctly rank materials from our dataset. This analysis therefore highlights the importance of going beyond the CRTA for accurate results. In particular, in material screening or high-throughput computing where this approach has been very popular, this indicates that the CRTA mobility or, equivalently, the transport effective mass [4, 63], should be used with extreme caution as a first filter to identify materials with high mobility and should be followed by a higher-level analysis of the transport if possible.

It is also clear from Fig. 1.6(b) that the SERTA and MRTA both perform better than the CRTA. In particular, in terms of ranking materials of our dataset, both of them prove to be adequate, with  $\rho^{\text{SERTA}} = 0.97$  and  $\rho^{\text{MRTA}} = 0.98$ . Additionally, Figs. 1.6(b) and 1.7(b) show that the MRTA performs overall better than the SERTA in approximating the IBTE, with a mean absolute percentage error of 18% for the former and 48% for the latter. In the materials investigated here, the MRTA mobility is always higher than the one predicted by the SERTA. Indeed, we specifically selected materials with a single band, that is often located around  $\Gamma$  in the BZ. In this case, intravalley scattering largely dominates, in particular with small wave vectors  $\mathbf{q}$  because the effective masses are lower than 1, hence the bands are relatively dispersive [48]. Note that intravalley scattering plays a crucial role even in cases where the band extrema are not at  $\Gamma$ . If the important wave vectors  $\mathbf{q}$  are small, then  $\alpha^{\text{MRTA}}$  is between 0 and 1, and the mobility increases from the SERTA to the MRTA. However, when compared to the IBTE, there is no general rule for the MRTA and it can underestimate or overestimate the mobility implying that the efficiency factor shown in Eq. (1.18) may

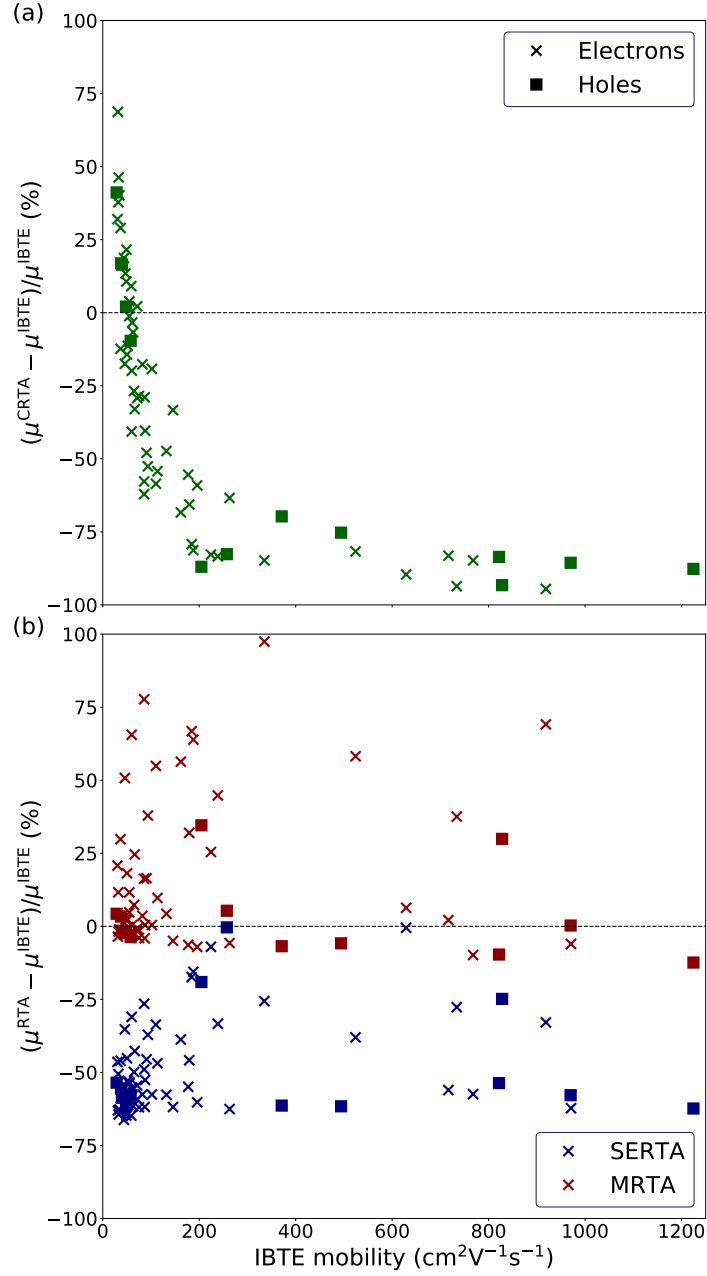


**Figure 1.7:** Absolute percentage errors of the (a) CRTA (in green), (b) SERTA, and MRTA (in blue and red, respectively) compared to the exact IBTE mobilities. For the CRTA, a constant lifetime of 10.3 fs was used for all the materials from the dataset in order to minimise the mean absolute error.

under or overestimate the back-scattering events. Since our results were performed at 300 K, some deviations could be observed at higher/lower temperatures [100, 101]. However, we do not expect significant changes in the trends and these small differences seems dependent on the material investigated as shown in Fig. 1.8 and 1.9.

In the literature, SERTA has often emerged as the most satisfactory approach. Indeed, for the few systems investigated so far (such as Si [45, 48, 98] or GaAs [48, 102]), it is predicted that the SERTA mobilities are closer to experimental data than the MRTA or IBTE results. Indeed, in Si, the differences between the SERTA, MRTA, and IBTE mobilities are lower than 5%, all of them being very close to experimental data [45, 48, 98]. However, in GaAs, there is a large spread in the reported computed mobilities, which can partly be explained by the different transport formalisms used for the computations, since the SERTA (MRTA) underestimates (overestimates) the IBTE solution by 52% (4%) [48, 101]. Our results demonstrate that large and difficult to predict errors can be present when using SERTA or MRTA.

From Fig. 1.6 and Table B.1.1, it is clear that some outliers show very important deviations from the IBTE mobility. For instance, in SrO, KH,  $\text{KMgH}_3$  and MgO, the MRTA leads to errors larger than 60% when compared to the exact IBTE solution.

While MRTA is performing better than SERTA, it seems impossible to estimate when the MRTA approach will fail (see Figs. B.2 and B.3 for a comparison of the relative error of these methods against some common material descriptors). This indicates that both the SERTA and MRTA can be unreliable for some specific systems and the IBTE should always be preferred. In particular, before comparing computed mobilities to experimental data, we believe it is crucial to first make sure that any approximation used in the process is reliable, or at least to quantify the error on the final quantity. We point out that using spatial and time-reversal symmetries, and a similar filtering method as presented in Ref. [48], solving the IBTE can be seen as a post-processing of the SERTA that does not lead to a significant increase of computational time nor memory. It is also worth noting that the type of charge carrier does not seem to affect these results.

The computed IBTE mobilities overestimate the experimental data, which is expected since other sources of scattering (e.g., impurity scattering) are completely ignored. In addition, most of the experimental mobilities reported in the literature are measured using the Hall effect and it is therefore necessary to weight computational results by a

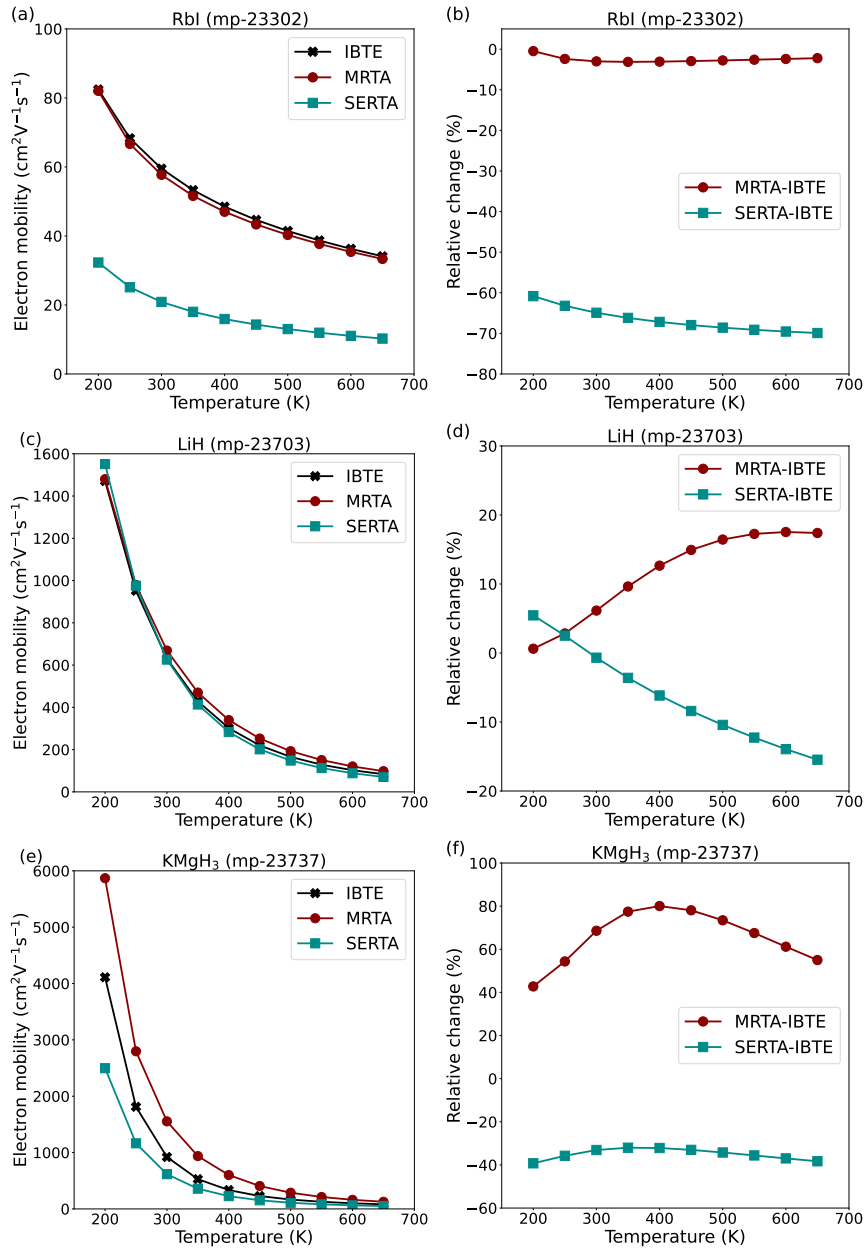


**Figure 1.8:** Influence of the temperature on the mobility results obtained with the MRTA, SERTA and IBTE approaches for 3 selected *n*-type materials (i.e., materials with a small or a large relative between RTA and IBTE).

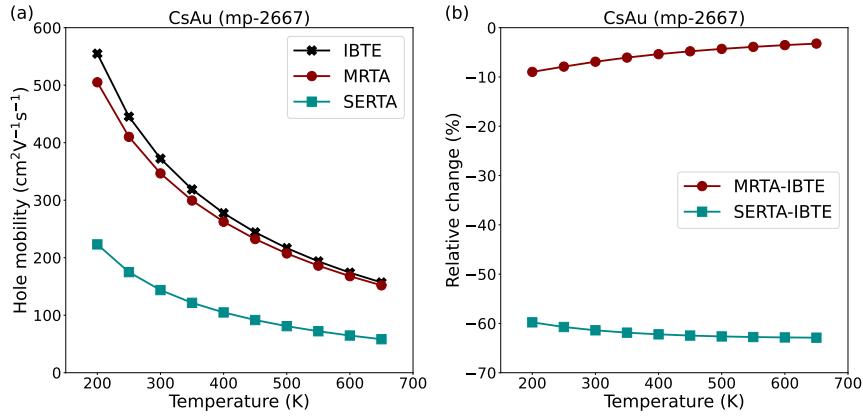


**Figure 1.9:** Influence of the temperature on the mobility results obtained with the MRTA, SERTA and IBTE approaches for  $p$ -type CsAu.

material-dependent Hall factor that typically ranges between 0.7 and 2 [85].

In essence, our results show that SERTA and to a lesser degree MRTA are not reliable in general and that they are in many cases not good approximations to the IBTE. This should be kept in mind when looking at previously-published results using any of these approaches. The fact that the SERTA/MRTA agree with experiments for a few systems is not sufficient to establish these methods as a standard. Given that IBTE does not require more computational power, it should be the recommended approach for computing transport properties.

### 1.2.5 Empirical models

While the previous section demonstrates the feasibility of computing phonon-limited mobility in a high-throughput manner, it is important to keep in mind that this approach is still currently limited to small-scale systems. In fact, due to the intricate nature of the task and the computational resources required to reach accurate results, alternative approaches have garnered attention within the scientific community. Among these, empirical models have emerged as a prominent choice, facilitating rapid calculations albeit at the expense of the accuracy of fully first principles methods. Empirical and semi-empirical models, for instance for lifetimes calculations, have been formulated and implemented since the early 1930s [36, 103–105], and still provide the basis of model-based contemporary approaches. Usually, the different

scattering interactions are split into different models which depend on specific parameters obtainable experimentally or theoretically. For instance, Fröhlich described the coupling between polar optical phonons and electrons in polar materials, *the so-called Fröhlich interaction*, using the isotropic dielectric constants and the longitudinal optical (LO) frequency as descriptors [103]. Subsequently, Vogl extended this model to encompass the anisotropy of dielectric constants and the involvement of multiple LO modes [106]. This extended version is actually still used directly [107, 108] or as a foundational framework for contemporary research in the field [109, 110].

Recently, a notable advancement has been made with the work of Ganose *et al.* [53], who introduced a model-based software called AMSET for efficiently calculating anisotropic transport properties using first-principles data. This approach enables the computation of anisotropic acoustic deformation potentials, piezoelectric effects, ionised impurity interactions, and polar e-ph scattering. In AMSET, models are used at the level of the e-ph matrix elements as this stage remains the main bottleneck in the BTE framework in terms of computational resources needed. AMSET presents a method that supports anisotropic materials, relies on routinely available inputs and is mostly based on the MRTA. In fact, with the exception of polar e-ph coupling, all the previously mentioned mechanisms can be categorised as elastic interactions, where there is no substantial change in energy during the collisions between electrons and phonons (or impurities); the primary change is in terms of momentum and the MRTA can be used to compute the scattering rates. However, this approximation falls short when considering polar phonons, where significant energy changes are anticipated due to the high frequency of these phonons. Hence, inelastic scattering is non-commutative, meaning that the likelihood of scattering from a state  $n\mathbf{k}$  to a state  $m\mathbf{k} + \mathbf{q}$  is not identical to scattering from  $m\mathbf{k} + \mathbf{q}$  to  $n\mathbf{k}$ . As a result, the MRTA framework can be problematic for inelastic scattering processes as one of the primary condition is not fulfilled, prompting the use of the SERTA instead [44, 53]. However, as discussed previously, SERTA is frequently associated with significant underestimations when compared to the IBTE solution [42, 71, 85]. This discrepancy can pose challenges when dealing with materials in which the polar e-ph coupling plays a pivotal role, as exemplified in the next chapter (Chap. 3) in the case of CuI [99]. Nevertheless, AMSET has proven to be a useful methodology for efficiently computing large material databases at a lower cost, consistently demonstrating strong agreement with experimental

results. This has positioned AMSET as a front-runner in the transport field, particularly in the quest for new materials with high mobility. Notably, recent efforts have harnessed AMSET for high-throughput computational tasks, leveraging machine learning to generate inputs used in the AMSET models across a dataset spanning over more than 20000 materials [111].

### 1.3 FUTURE WORK

This section is dedicated to some ideas about the next big steps that need to be implemented in *Abinit*. One of the priorities is probably to provide access to Hall mobility, enabling better comparison with experimental results while reducing the gap with other codes that already enable this type of calculation. The computation of ionised-impurity scattering can also greatly enhance our understanding of transport phenomena. Initially, it can be harnessed through the use of empirical models, and eventually, it may be employed through a first-principles approach. Additionally, the transition to an infrastructure that facilitates improved workflow management stands as a pivotal necessity for the continuity of high-throughput research.

#### 1.3.1 *Hall transport*

Overall, experimental measurements are done via the Hall effect and computing the Hall mobility becomes crucial in order to facilitate the comparison between theoretical and experimental results. Notably, experimental Hall measurements are more prevalent than drift time-of-flight measurements, primarily due to their simplicity and often higher accuracy. These Hall measurements are conducted under the additional influence of an external magnetic field  $\mathbf{B}$ , which exerts an additional Lorentz force on the charge carriers, consequently altering their mobility. This results in the BTE being extended to include a new

term that characterises the behaviour of charge carriers in the presence of a magnetic field and Eq. (1.14) is now written as [44, 85, 112]

$$\begin{aligned}
& [1 - \tau_{nk}^0 (\mathbf{v}_{nk} \times \mathbf{B}) \cdot \nabla_{\mathbf{k}}] \left. \frac{\partial f_{nk}}{\partial E_{\beta}}(\mathbf{B}) \right|_{\mathbf{E}=0} = \frac{\partial f_{nk}^0}{\partial \varepsilon_{nk}} v_{nk,\beta} \tau_{nk}^0 \\
& + 2\pi \tau_{nk}^0 \sum_{m,\nu} \int \frac{d\mathbf{q}}{\Omega_{\text{BZ}}} |g_{m\nu}(\mathbf{k}, \mathbf{q})|^2 \\
& \times [(1 + n_{\mathbf{q}\nu} - f_{nk}^0) \delta(\varepsilon_{nk} - \varepsilon_{m\mathbf{k}+\mathbf{q}} + \omega_{\mathbf{q}\nu}) \\
& + (n_{\mathbf{q}\nu} + f_{nk}^0) \delta(\varepsilon_{nk} - \varepsilon_{m\mathbf{k}+\mathbf{q}} - \omega_{\mathbf{q}\nu})] \left. \frac{\partial f_{m\mathbf{k}+\mathbf{q}}}{\partial E_{\beta}}(\mathbf{B}) \right|_{\mathbf{E}=0}.
\end{aligned} \tag{1.19}$$

As we consider small magnetic fields, their effect on the electronic and vibrational properties can be disregarded and evaluated at  $\mathbf{B}=0$ . When a magnetic field is applied in the direction  $\hat{\mathbf{B}}$ , it induces an orthogonal flow of charge carriers that can be described using the linear response of the mobility to this magnetic field [71, 85]

$$\mu_{\alpha\beta}^{(2)}(\hat{\mathbf{B}}) = - \lim_{\mathbf{B} \rightarrow 0} \frac{1}{|\mathbf{B}|} \left[ \frac{1}{n_C \Omega} \sum_n \int \frac{d\mathbf{k}}{\Omega_{\text{BZ}}} v_{nk,\alpha} \frac{\partial f_{nk}}{\partial E_{\beta}}(\mathbf{B}) - \mu_{\alpha\beta} \right]. \tag{1.20}$$

Therefore, we can linked the Hall mobility  $\mu^{\text{H}}$  directly to the drift mobility  $\mu$  using the Hall factor  $r^{\text{H}}$  following

$$\mu_{\alpha\beta}^{\text{H}}(\hat{\mathbf{B}}) = \sum_{\gamma} r_{\alpha\gamma}^{\text{H}}(\hat{\mathbf{B}}) \mu_{\gamma\beta}, \tag{1.21}$$

with the dimensionless Hall factor defined as [71, 85]

$$r_{\alpha\gamma}^{\text{H}}(\hat{\mathbf{B}}) = \sum_{\delta} \mu_{\alpha\gamma}^{-1} \mu_{\gamma\delta}^{(2)}(\hat{\mathbf{B}}) \mu_{\delta\beta}^{-1}. \tag{1.22}$$

The Hall factor is material-dependent and also varies with the intensity of the magnetic field, the temperature and the doping. Usually,  $r^{\text{H}}$  varies between 0.7 and 1.9 at room temperature but can change considerably with T [85]. For instance, a value around 1.15 is found for Si and GaAs [85, 113]. This Hall factor can be determined experimentally with the Hall coefficient  $R^{\text{H}}$  that is determined when performing a Hall effect experiment [1]

$$R^{\text{H}} = \frac{\mu^{\text{H}}}{\sigma} = \frac{1}{n} r^{\text{H}}. \tag{1.23}$$

This Hall coefficient is also often used experimentally to determine the number of carriers as well as the nature of the carriers that conduct the current inside a material: a negative (positive)  $R^{\text{H}}$  result in an electron (hole) conduction [1].

### 1.3.2 *Ionised impurity scattering*

At room temperature in high-purity crystals, e-ph scattering typically dominates. However, when carrier concentrations exceed  $10^{15}$ - $10^{16}$   $\text{cm}^{-3}$ , the influence of ionised impurities becomes significant [1]. In fact, numerous semiconductor applications need the introduction of free carriers through the incorporation of dopant elements to ensure their functionality and performance. Hence, the ability to compute their interactions with carriers becomes crucial, and various approaches are available for this purpose. For instance, one can employ semi-empirical models like the Brooks-Herring formula [105, 114]. Nevertheless, the majority of these models relies on a simplified single parabolic band picture, limiting their accuracy for materials with multiple bands or valleys, or with strong anisotropy. To address this limitation, an enhanced integration scheme can be employed such as the one implemented in the AMSET software [53]. Still based on the Brooks-Herring model, AMSET employs a linear-tetrahedron approach that enables the evaluation of Coulomb-based impurity scattering even in complex systems with non-parabolic bands. In EPW, the approach is based on multiple approximations, including a randomized distribution of point charges and seems very promising in materials such as Si, Si-C, and GaP, showing good agreement with experimental data [71, 115].

### 1.3.3 *Improvement of the workflow*

In the context of high-throughput calculations, one of the next major objectives will be to transition from Abipy [93] to dedicated infrastructures and codes such as Fireworks [116], AiiDA [117] and atomate [118]. While Abipy performs effectively for smaller material lists, its limitations become evident in larger-scale calculations involving numerous materials, demanding a higher degree of automation. Furthermore, there are still certain manual tasks that should be automated. For instance, these tasks encompass the automatic restart of the calculations when the convergence is not achieved, or the necessity to manually incorporate quadrupole contributions into the relevant calculation input file if they need to be considered. Moreover, several optimisations can be implemented to further reduce the computational cost of these transport calculations. One such optimisation is the automatic determination of the optimal energy window related to the Fermi-Dirac occupation function (see Eq. 1.14). As the derivative of the Fermi-Dirac

occupation function decreases rapidly close to the Fermi level, there is no need to sample all the electronic states and an energy windows can be chosen [48]. For the moment, this window is manually fixed to specific value ( $\sim 10 \times k_B T$ ) which is independent on the material and need a convergence study to be optimal. In order to bypass the time-consuming convergence study in our high-throughput computations, the window was set for all materials at 0.3 eV. This corresponds to an overestimated value (based on our own experience), to ensure that all the participating states were taken into account in the transport calculation. However, this also implies that many states not involved in transport have also been taken into account in some (all?) materials, considerably increasing calculation times. This kind of optimisation would make our implementation even more competitive.

#### 1.4 CONCLUSION

In conclusion, we have obtained well-converged phonon-limited mobilities for a medium set of semiconductors. We have developed and used an automatic workflow that allows for the comparison of different approximations to the BTE with the exact results. Our results show that SERTA and to a lesser degree MRTA are not reliable in general and that they are in many cases not good approximations to the IBTE. Since IBTE necessitates only implementation without an increased computational burden, it emerges as the preferable choice for computing transport properties.

When comparing our results with experimental measurements, we anticipate consistently higher values with IBTE, as our approach does not take into account scattering by impurities and defects. However, even in the context of a perfect crystal with no defects or impurities, we expect the IBTE to slightly diverge from experimental measurements. In fact, the IBTE serves as an exact solution to the BTE but is therefore grounded in DFT. Moving towards advanced approaches like hybrid functionals or GW in the near future holds the potential to significantly narrow the gap between theoretical predictions and experimental observations. In essence, it becomes imperative to take many-body effects into account and to consider additional scattering processes to enhance the agreement between theory and experiment.

Furthermore, it is important to bear in mind the limitations of the BTE approach. For instance, a notable limitation in most first-principles BTE calculations lies in their confinement to room temperature. Yet, it

is well-established that the band structure of materials requires renormalisation due to e-ph coupling which, in turn, is dependent of temperature. In addition, low temperature regimes introduce new challenges as phonon-induced scattering no longer dominates. Alternative methodologies, such as the Landauer-Buttiker approach, may prove more effective in these scenarios. Additionally, low temperatures pose computational challenges. For instance, very few different electronic states are accessible leading to a narrow peak close to the band edge due to the product of Fermi-Dirac occupations and the electronic density of states, demanding significantly higher computational grids. Conversely, tackling high temperatures is also challenging. Unlike low temperatures, high temperatures increase the number of states participating in transport, leading to a surge in the number of transitions that must be computed. This results in computationally intensive calculations. Another important limitation of the BTE is the potential breakdown of perturbation theory in the regime of strong e-ph coupling. Indeed, as the coupling intensity increases, it gives rise to a unique mode of transport, ensnaring carriers within specific lattice sites. The unique interplay between a self-localised carrier and the phonon that entraps it is referred to as a polaron [103]. To address the challenge posed by polarons, specific approaches should be employed [71, 119–122].

Nevertheless, our work demonstrates that phonon-limited mobilities can be computed automatically in a high-throughput manner, opening new avenues for materials screening. While it may be challenging to compete with faster models-based screening methods, such as AMSET, it could serve as a valuable complement to enhance the depth of analysis or potentially improve existing models. For instance, by understanding why they tend to fail for certain families of materials, if this is the case.



QUASI-1D ELECTRONIC TRANSPORT AND  
ISOTROPIC PHONON TRANSPORT IN THE ZINTL  
 $CA_5IN_2SB_6$

---

Thermoelectric materials, used to convert heat into electricity, have a wide variety of applications including industrial waste-heat recovery, remote sensing, and powering space exploration [123]. High efficiency thermal-to-electrical energy conversion requires materials with a high Seebeck coefficient and electrical conductivity while possessing low thermal conductivity. This combination is exceptionally difficult to achieve simultaneously – posing a fundamental dilemma for those developing materials with improved thermoelectric figure-of-merit (FoM),  $zT$ . Materials with anisotropic crystal structures offer a potential strategy to decouple these properties, since the degree of anisotropy exhibited by each transport coefficient can differ [124, 125]. This has been demonstrated in several important thermoelectric materials [125–127], including the recent study of single crystalline SnSe, in which exceptionally high  $zT$  values ( $> 2$ ) were reported [124]. In all of these cases, the highest  $zT$  is found to be in the direction with the highest electrical conductivity.

Zintl phases, with their vast range of structural patterns in non-cubic space groups [128] and their excellent high-temperature thermoelectric performance [35], stand out as an intriguing area for transport anisotropy studies. The covalently-bonded polyanions exemplified by Zintl phases crystallize in a diverse range of highly anisotropic substructures, including isolated moieties (e.g.,  $Yb_{14}MnSb_{11}$  [34]), 1D chains ( $A_5M_2Sb_6$  and  $A_3MSb_3$ ), 2D sheets ( $AM_2X_2$  [129]) and 3D networks ( $KGaSb_4$  [130],  $BaGa_2Sb_2$  [131]). However, despite ample theoretical evidence [132–135] of light effective mass and enhanced thermoelectric efficiency in the covalently-bonded direction, experimental confirmation is still lacking in the vast majority of Zintl compounds. This knowledge gap has been exacerbated by the difficulty of growing single crystals of sufficient size and quality for complete transport property characterisation. Zintl compounds often melt incongruently, have high melting temperatures, and contain reactive and/or high vapor-pressure elements, all of which make directional solidification methods (e.g.,

Bridgman or Czochralski techniques) impractical. Zintl crystals are usually precipitated from a molten metal flux [136], which has the advantage of reducing the melting temperature, diluting the most reactive elements (usually the cation), and allowing for growth of incongruent phases. The drawback is often small, anisotropic crystals with at least one difficult-to-characterise dimension.

In this study, we combine theory and experiment to investigate the anisotropic behaviour of the quasi-1D compound,  $\text{Ca}_5\text{In}_2\text{Sb}_6$ . Prior computational studies have predicted highly anisotropic effective mass, with light effective mass in the  $c$ -direction, but this has not been confirmed experimentally [132]. Instead, prior experimental studies of the  $\text{A}_5\text{M}_2\text{Sb}_6$  family of compounds (including  $\text{A}=\text{Ca}$ ,  $\text{Sr}$  and  $\text{M}=\text{Al}$ ,  $\text{Ga}$  or  $\text{In}$ ) have focused on optimising composition through doping and alloying, leading to promising  $zT$  values at intermediate temperatures (e.g.,  $zT = 0.7$  in Zn-doped  $\text{Ca}_5\text{In}_2\text{Sb}_6$  at 900K) in polycrystalline samples [137]. Here, we revisit *ab initio* predictions of anisotropic electronic properties using an improved scattering model and we investigate thermal anisotropy using phonon calculations and experimental thermal expansion coefficients. Thanks to a collaboration with experimentalists, we manage to compare our theoretical results with experimental measurements based on single crystals grown from molten metal flux. In fact, they used a photolithography approach to measure electronic transport along the smallest dimension of  $\text{Ca}_5\text{In}_2\text{Sb}_6$  crystals, allowing them to obtain electrical resistivity both parallel and perpendicular to the growth direction for the first time. This chapter is based on Ref. [60].

## 2.1 CRYSTAL AND ELECTRONIC STRUCTURE

The structure of  $\text{Ca}_5\text{In}_2\text{Sb}_6$ , shown in Fig. 2.1(a), is characterised by anionic substructures (Fig. 2.1(b)) resembling chains of corner-linked  $\text{InSb}_4$  tetrahedra aligned in the  $c$ -direction. Each neighboring chain is joined via  $\text{Sb-Sb}$  covalent bonds to form infinite polyanionic ladders. The electronic band structure of  $\text{Ca}_5\text{In}_2\text{Sb}_6$ , shown in Fig. 2.2 along high symmetry directions, has a direct band gap of 0.15 eV between  $\text{Y}$  and  $\Gamma$ . Since density-functional theory (DFT) with GGA is known to underestimate band gaps, for the purposes of calculating transport coefficients, a scissor operator was used to match the experimental band gap of 0.64 eV obtained from optical measurements [132]. Below, we focus our analysis on the valence band (VB) in the energy range

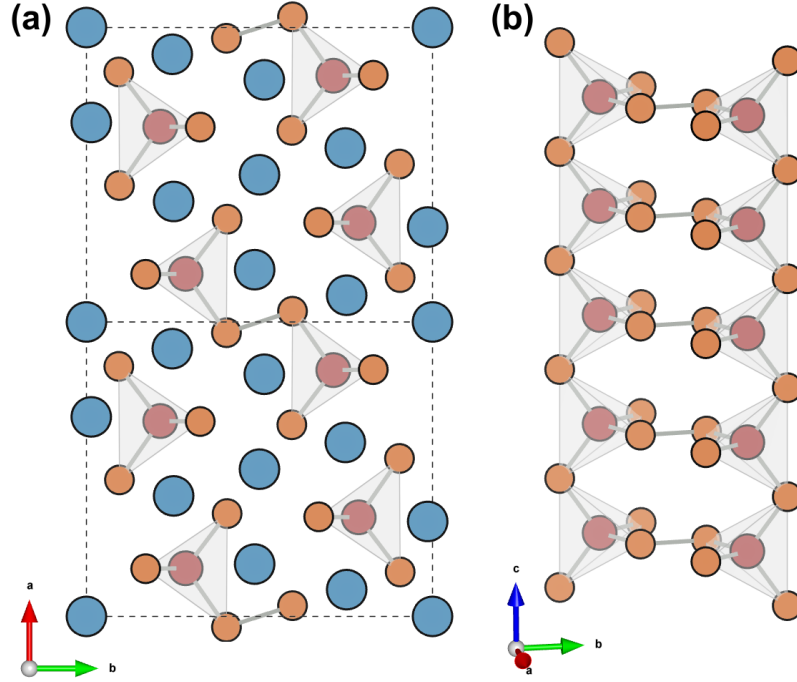


**Figure 2.1:** (a) The orthorhombic unit cell of  $\text{Ca}_5\text{In}_2\text{Sb}_6$ . Ca, In and Sb atoms in blue, red and orange, respectively. (b) 1D tetrahedral ladders aligned parallel to the  $c$ -axis.

from  $\varepsilon_f = -0.2$  to  $0$  eV, since, to date, all  $\text{A}_5\text{M}_2\text{Sb}_6$  compounds (including  $\text{A}=\text{Ca}$ ,  $\text{Sr}$  and  $\text{M}=\text{Al}$ ,  $\text{In}$ ,  $\text{Ga}$ ) synthesised with this structure type have been  $p$ -type [138]. For  $\text{Ca}_5\text{In}_2\text{Sb}_6$ , the nominally undoped polycrystalline samples reported in Zevalkink *et al.* [132], as well as the  $\text{Ca}_5\text{In}_2\text{Sb}_6$  single crystals synthesised for the current study have  $n \sim 10^{18} \text{h}^+/\text{cm}^3$  (corresponding to  $\varepsilon_f = -0.25$  eV), while Zn-doped polycrystalline samples have been reported with up to  $10^{20} \text{h}^+/\text{cm}^3$  ( $\varepsilon_f = -1.7$  eV).

The valence band maximum (VBM) of  $\text{Ca}_5\text{In}_2\text{Sb}_6$  consists of two bands, each of which has a degeneracy of two due to symmetry, leading to an overall band degeneracy of  $N_V = 4$ . The VB is highly anisotropic; the Fermi surface at  $10^{19} \text{h}^+/\text{cm}^3$  resembles a plate oriented perpendicular to the  $c$ -axis as seen in Fig. 2.3. Table 2.1 shown compares the conductivity effective masses  $m_a^*$ ,  $m_b^*$ , and  $m_c^*$  along the three principle directions. Note that the conductivity effective mass controls electronic mobility and is determined by the average curvature of the bands near  $\varepsilon_f$  in a particular  $k$ -space direction [4, 62, 139]. It takes into account

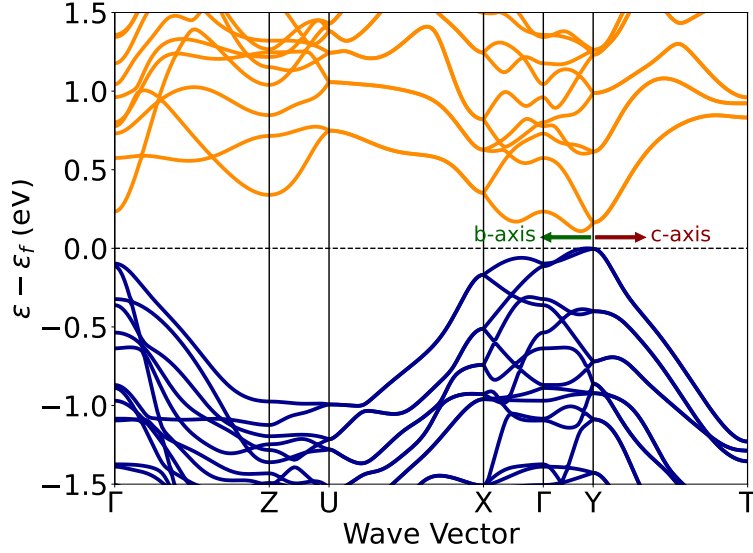


**Figure 2.2:** The electronic band structure has a direct band gap with valence band maximum between  $\Gamma$  and Y consisting of two degenerate bands.

all the bands and regions in the Brillouin zone involved in transport at the specified Fermi energy and temperature. The density of states effective mass ( $m_{DOS}^*$ ), in contrast, is a scalar quantity and determines the Seebeck coefficient. The distinction between  $m_{DOS}^*$  and  $m^*$  is what enables enhanced  $zT$  along the light inertial mass and high mobility direction of anisotropic materials [140].

$m_a^*$ (Y-S)	$3.33 m_e$
$m_b^*$ (Y- $\Gamma$ )	$1.17 m_e$
$m_c^*$ (Y-T)	$0.15 m_e$
$m_{avg}^*$	$1.55 m_e$

**Table 2.1:** Conductivity effective mass for the different directions.

In  $\text{Ca}_5\text{In}_2\text{Sb}_6$ , the carrier transport in the  $c$ -direction, parallel to the polyanionic chains, has the lightest mass with  $m_c^*$  (Y-T) =  $0.15 m_e$ , while the effective masses in the  $b$ - and  $a$ -directions are 8 and 20 times heavier, at  $m_b^*$  (Y- $\Gamma$ ) =  $1.17 m_e$  and  $m_a^*$  (Y-S) =  $3.33 m_e$ , respectively. The light mass in the  $c$ -direction likely stems from the polar-covalent In-Sb bonds that form a continuous chain along the  $c$ -direction. The covalent

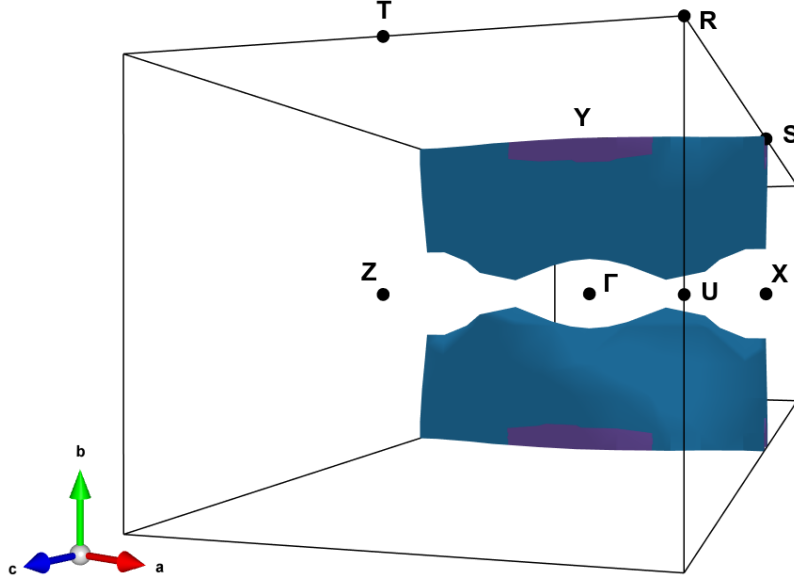


**Figure 2.3:** The Fermi surface of  $\text{Ca}_5\text{In}_2\text{Sb}_6$  at a hole concentration of  $10^{19}\text{h}^+/\text{cm}^3$  reveals quasi-1D conduction in the  $c$ -direction.

Sb–Sb dumbbells are oriented along the  $b$ -direction but do not form a continuous network. In contrast, bonding along the  $a$ -direction is characterised only by ionic Ca–Sb bonding, likely leading to the high effective mass.

## 2.2 CARRIER CHARGE TRANSPORT

The conductivity effective masses and transport properties were obtained with the BoltzTraP software [58, 59]. Typically, BoltzTraP employs the CRTA for carrier scattering. In order to overcome this rather rough approximation, the BoltzTraP software was modified to include an energy and temperature dependent relaxation time  $\tau(\varepsilon, T)$  following [141]:

$$\tau(\varepsilon, T) = \tau_0(\varepsilon_0, T_0) \left( \frac{T}{T_0} \right)^s \left( \frac{\varepsilon}{\varepsilon_0} \right)^{r-1/2} \quad (2.1)$$

where the reference relaxation time,  $\tau_0$ , is kept variable in order to fit experimental results. The energy,  $\varepsilon_0$ , and the temperature,  $T_0$ , are fixed to 0.01 eV and 600K, respectively. Parameters  $s$  and  $r$  depend on the scattering type considered. Ionised impurity (II) scattering sets the parameters to  $s = 0$  and  $r = 2$  whereas the acoustic phonon (AP)

scattering use  $s = -1$  and  $r = 0$ . The contributions from the two scattering mechanisms were summed via the Matthiessen's rule. Note that polar optical phonon scattering (POP) was also considered ( $s = -1$  and  $r = 1$ ) but we found that the ratio of AP-to-POP did not significantly change the temperature dependence of transport coefficients. For this reason, POP was omitted for the purpose of this study.

While this approach has proven effective in fitting polycrystal results within our specific context, it is imperative to be cautious regarding its predictive capabilities. Recent findings highlight that temperature dependence alone may not serve as a dependable indicator of the predominant scattering mechanisms [111]. In simpler terms, the utilization of the parameters  $s$  and  $r$  to characterise the different scattering mechanisms may not accurately represent these mechanisms. This suggests the possibility that, for instance, polar optical phonons could influence the behaviour of the transport in this material, as the parameters assigned to describe them may be inaccurate.

Fig. 2.4 and Fig. 2.5 shows the calculated resistivity and Seebeck coefficients, respectively, of  $\text{Ca}_5\text{In}_2\text{Sb}_6$  (solid and dotted curves) compared with experimental polycrystalline data from an undoped sample ( $n = 4 \times 10^{18} \text{h}^+/\text{cm}^3$ ) and a Zn-doped sample ( $n = 2 \times 10^{20} \text{h}^+/\text{cm}^3$ ) taken from Zevalkink *et al.* [137]. The transport along the three principle axes, as well as the directionally-average coefficients, were computed from the electronic band structure by solving the Boltzmann equation with energy-dependent relaxation times. The individual relaxation times for ionised impurity ( $\tau_{0,\text{II}}$ ) and acoustic phonon ( $\tau_{0,\text{AP}}$ ) scattering were used as fitting parameters to ensure that the computed average resistivity matched the experimental resistivity of polycrystalline samples. Table 2.2 shows the value of  $\tau_0$  used to fit experimental results for the two scattering mechanisms. The polycrystalline average was taken as the average of the resistivities along the perpendicular axes. This average can be considered as an upper bound on the resistivity of the polycrystalline bulk, and thus may lead to slight overestimation of the single crystal resistivities [142].

$n$ ( $\text{cm}^3$ )	$\tau_{0,\text{II}}$ (fs)	$\tau_{0,\text{AP}}$ (fs)
$4 \times 10^{18}$	0.160	1600
$2 \times 10^{20}$	0.016	55

**Table 2.2:** Values of  $\tau_0$  used to fit experimental results for ionised impurity scattering (II) and acoustic phonon scattering (AP).

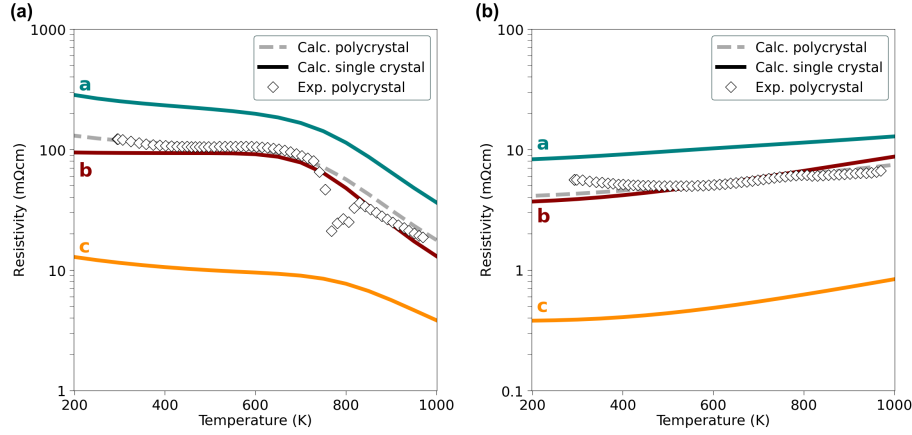


**Figure 2.4:** The calculated directional (solid curves) and average (dotted curves) resistivity of  $\text{Ca}_5\text{In}_2\text{Sb}_6$  compared with experimental polycrystalline data (diamond symbols) from Ref. [137] for a carrier concentration of (a)  $4 \times 10^{18} \text{h}^+/\text{cm}^3$  and (b)  $2 \times 10^{20} \text{h}^+/\text{cm}^3$ .

In orthorhombic crystals, three coefficients ( $\rho_{xx}$ ,  $\rho_{yy}$ ,  $\rho_{zz}$ ) corresponding to transport along each of the principle axes (a, b, and c, respectively), are sufficient to fully describe the resistivity tensor,  $\rho_{ij}$ . Likewise for the Seebeck tensor,  $\alpha_{ij}$  [143] and the electronic thermal conductivities,  $\kappa_{e,ij}$  (see Fig. 2.6 for the latter). In  $\text{Ca}_5\text{In}_2\text{Sb}_6$ , the predicted resistivity along the c-axis (parallel to the polyanionic chains) is found to be roughly an order of magnitude lower than the a- or b-axes, following the trend in conductivity effective mass described above. The ratio between the resistivity along the three directions remains largely constant as a function of temperature and Fermi level. In contrast to the highly anisotropic electrical resistivity, the Seebeck coefficient varies by only 10-20% between the three principle axes at 200K. Similar behaviour has been noted in many anisotropic materials (e.g., SnSe [124],  $\text{Bi}_2\text{Te}_3$  [125] and GeAs [144]); the conductivity is often orders of magnitude more anisotropic than the Seebeck coefficient, thus leading to improved power factor along the high conductivity direction of the crystal. As shown by Parker *et al.* in Ref. [140], the Seebeck coefficient will be isotropic as long as the band(s) can be modeled as a single parabolic band, and the scattering rate,  $\tau$ , is isotropic. This remains true regardless of the degree of band mass anisotropy. Our calculations assume by default that  $\tau$  is isotropic. Therefore, the predicted anisotropy in the Seebeck coefficient of  $\text{Ca}_5\text{In}_2\text{Sb}_6$  arises due to deviations from parabolic band curvature and from the contributions of additional

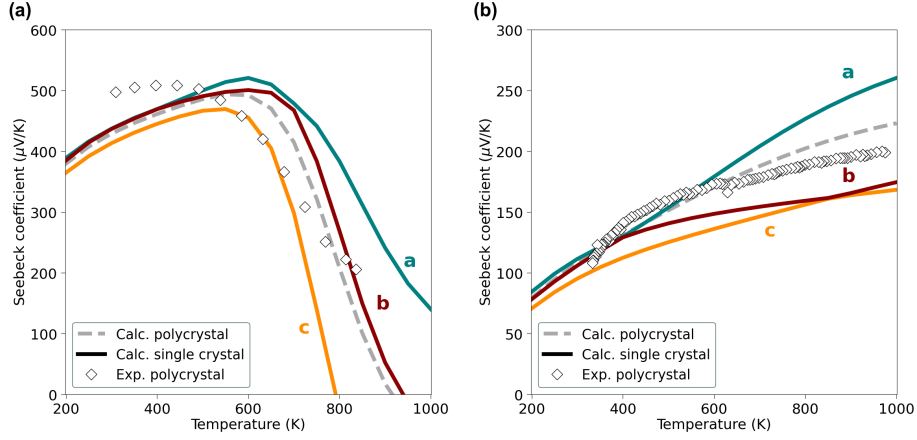


**Figure 2.5:** The calculated directional (solid curves) and average (dotted curves) Seebeck coefficient of  $\text{Ca}_5\text{In}_2\text{Sb}_6$  compared with experimental polycrystalline data (diamond symbols) from Ref. [137] for a carrier concentration of **(a)**  $4 \times 10^{18}\text{h}^+/\text{cm}^3$  and **(b)**  $2 \times 10^{20}\text{h}^+/\text{cm}^3$ .

bands, especially from carrier excited to the conduction band. These contributions cause the Seebeck to become increasingly isotropic at high temperatures.

The predicted  $zT$  values shown in Fig. 2.7 were calculated using the experimental values of  $\kappa_l$  ( $\sim 1.1 \text{ W/mK}$  at 300K –  $0.7 \text{ W/mK}$  at 1000K) reported for the undoped polycrystalline sample in Ref. [132]. The predicted  $zT$  is highest in the  $c$ -direction for both  $p$ -type carrier concentration regimes, peaking at lower temperatures for  $n = 10^{18}\text{h}^+/\text{cm}^3$ , due to activation of intrinsic carriers. While the directionally-averaged  $zT$  is predicted to be higher in doped samples ( $n = 2 \times 10^{20}\text{h}^+/\text{cm}^3$ ) than in undoped samples, the predicted  $zT$  along the  $c$ -direction is optimized at much lower carrier concentrations due to the lighter effective mass, peaking at 1.8 at 600K. The  $zT$  predictions in Fig. 2.7 make two major assumptions that should not be taken for granted: (i) isotropic lattice thermal conductivity and (ii) isotropic scattering of electronic carriers.

### 2.3 EVIDENCE FOR ISOTROPIC LATTICE THERMAL CONDUCTIVITY

The anisotropy of the lattice thermal conductivity ( $\kappa_l$ ) of a crystal is primarily a function of the speed of sound tensor, which, in turn, is determined by the elastic tensor. McKinney *et al.* [145] showed recently

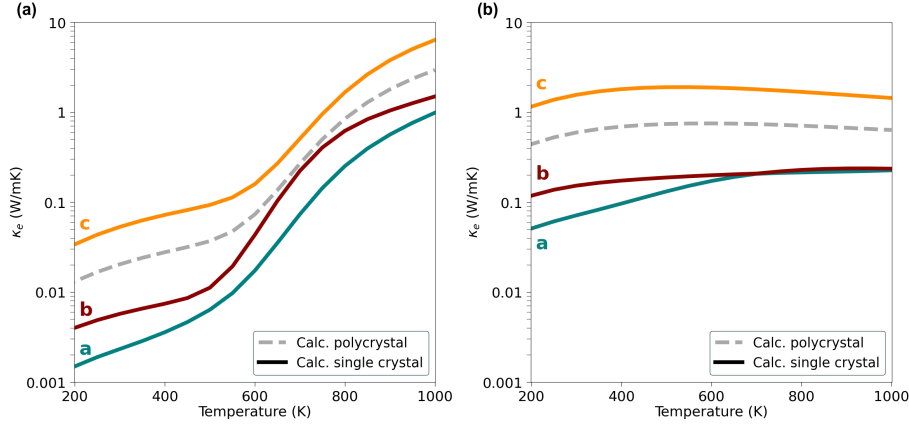


**Figure 2.6:** The calculated directional (solid curves) and average (dotted curves) electronic thermal conductivity of  $\text{Ca}_5\text{In}_2\text{Sb}_6$  for a carrier concentration of (a)  $4 \times 10^{18} \text{h}^+ / \text{cm}^3$  and (b)  $2 \times 10^{20} \text{h}^+ / \text{cm}^3$ .

that anisotropic lattice thermal conductivity of a wide variety of materials can be reproduced reasonably well using only the computed elastic tensor. In general, isotropic elastic constants lead to isotropic lattice thermal conductivity. The computed elastic tensor of  $\text{Ca}_5\text{In}_2\text{Sb}_6$  [146] was found to be only slightly anisotropic; the Young's modulus varies from 51 GPa in the  $x$ -direction to 64 GPa in the  $y$ -direction, suggesting that the ionic Ca–Sb bonds are as stiff as the polar-covalent In–Sb bonds forming the polyanionic backbone of the structure. From the elastic tensor of  $\text{Ca}_5\text{In}_2\text{Sb}_6$ , we computed the speed of sound tensor which is nearly completely isotropic (see Table 2.3). This suggests that  $\kappa_l$  in  $\text{Ca}_5\text{In}_2\text{Sb}_6$  is likewise isotropic.

	$\nu_{T,1}$	$\nu_{T,2}$	$\nu_L$	$\nu_{\text{AVG}}$	$\gamma$
$\Gamma$ -X	1737	2392	3670	2600	1.37
$\Gamma$ -Y	2029	2395	3654	2693	1.36
$\Gamma$ -Z	1850	2091	4124	2688	1.27

**Table 2.3:** Computed transverse ( $\nu_T$ ), longitudinal ( $\nu_L$ ) and average ( $\nu_{\text{AVG}} = (\nu_{T,1} + \nu_{T,2} + \nu_L)/3$ ) sound velocities (in m/s) and mode Grüneisen parameters ( $\gamma$ ) along the principal axes.

The large unit cell of  $\text{Ca}_5\text{In}_2\text{Sb}_6$  (26 atoms per primitive cell) means that the optical modes may also play an important role in heat transport. As can be seen from the computed phonon dispersion shown in Fig. 2.8,

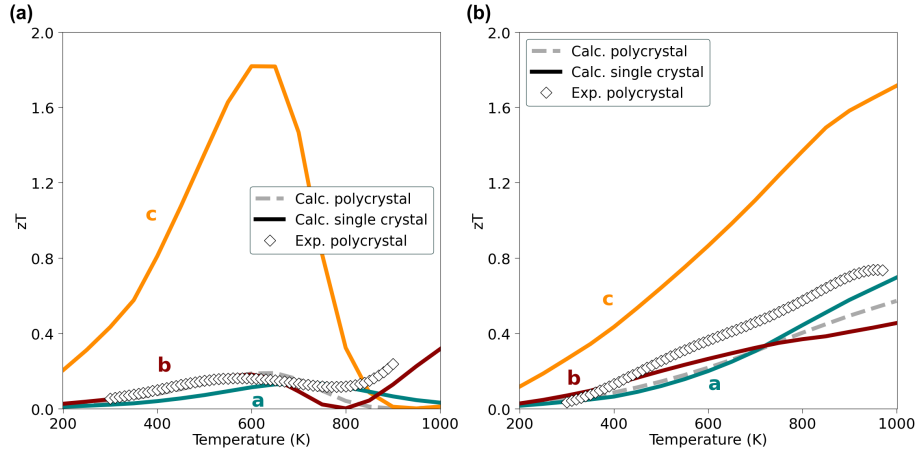


**Figure 2.7:** The calculated directional (solid curves) and average (dotted curves) FoM  $zT$  of  $\text{Ca}_5\text{In}_2\text{Sb}_6$  (assuming isotropic lattice thermal conductivity) compared with experimental polycrystalline data (diamond symbols) from Ref. [137] for a carrier concentration of (a)  $4 \times 10^{18} \text{h}^+/\text{cm}^3$  and (b)  $2 \times 10^{20} \text{h}^+/\text{cm}^3$ .

the velocity of the optical phonons in  $\text{Ca}_5\text{In}_2\text{Sb}_6$  are likewise nearly isotropic. Disparities between the  $a$ ,  $b$ , and  $c$  directions ( $\Gamma$ - $X$ ,  $\Gamma$ - $Y$ , and  $\Gamma$ - $Z$ , respectively), are comparable to what we observe for acoustic velocities.

Lastly, we consider the possibility of anisotropic phonon scattering rates. The computed mode Grüneisen parameters of  $\text{Ca}_5\text{In}_2\text{Sb}_6$  are shown in Fig. 2.8 and Fig. 2.9. Averaging the Grüneisen parameters along each principle axes yields slightly higher values for phonons propagating along the  $a$ - and  $b$ -directions (1.37 and 1.36, respectively) compared to the  $c$ -direction (1.27). These computed Grüneisen parameters are in excellent agreement with the experimental thermal expansion data. In fact, the linear coefficients of thermal expansion of the  $a$ -axis are the highest ( $1.52 \times 10^{-5} \text{K}^{-1}$ ), consistent with the higher Grüneisen parameter in that direction. The  $b$ - and  $c$ -axes are slightly lower ( $1.32 \times 10^{-5} \text{K}^{-1}$  and  $1.26 \times 10^{-5} \text{K}^{-1}$ , respectively). However, the overall variation is less than 20%, suggesting that the anharmonic bonding character is comparable along the three primary directions, i.e., the ionic bonds and the covalent bonds are equally harmonic. This, combined with the isotropic speed of sound indicates that our earlier assumption of isotropic lattice thermal conductivity in  $\text{Ca}_5\text{In}_2\text{Sb}_6$  was likely a reasonable one.

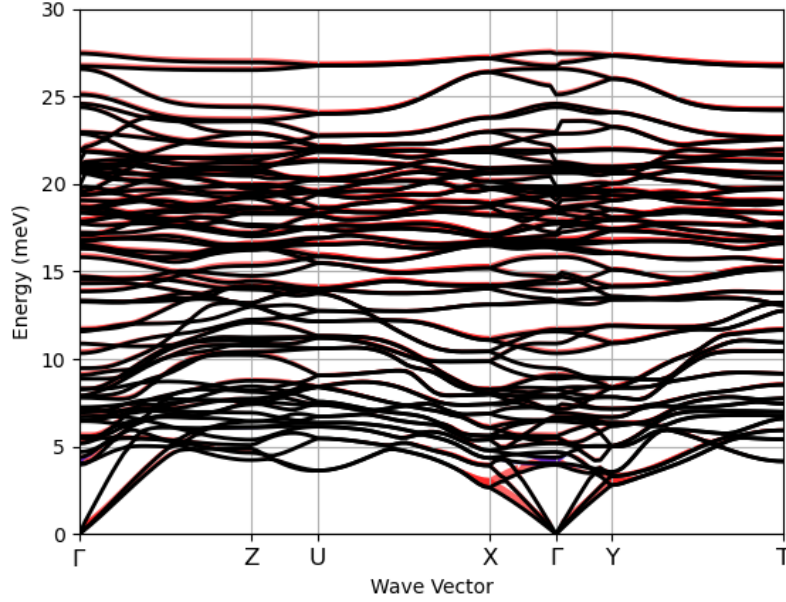


**Figure 2.8:** Calculated phonon dispersion of  $\text{Ca}_5\text{In}_2\text{Sb}_6$  with mode Grüneisen parameters represented by the thickness of the curves (red = positive, blue = negative).

#### 2.4 SINGLE CRYSTALS MEASUREMENTS

Single crystals of  $\text{Ca}_5\text{In}_2\text{Sb}_6$  were grown by Smiadak *et al.* [60] to verify the predicted electronic transport properties. The methodology used can be seen in Ref. [60]. The consequence of the highly anisotropic growth is that individual crystals can grow several millimeters along their preferred growth direction ( $c$ -direction) but only measured in the tens of microns in the perpendicular directions ( $a$ - and  $b$ -). A traditional four-probe method using manually-placed contacts could only be used to measure the resistivity parallel to the  $c$ -axis (blue symbols in Fig. 2.10), but this method was impractical for measurements in the  $a$ - and  $b$ -directions. For this reason, we pursued micro-fabrication techniques whereby regularly-shaped micro-ribbons oriented either parallel or perpendicular to the  $c$ -axis were extracted from single crystals using a FIB milling technique. The resistivity obtained from a micro-ribbon oriented perpendicular to the  $c$ -axis, shown as the green symbols in Fig. 2.10, was found to be 13–18 $\times$  higher than the parallel direction.

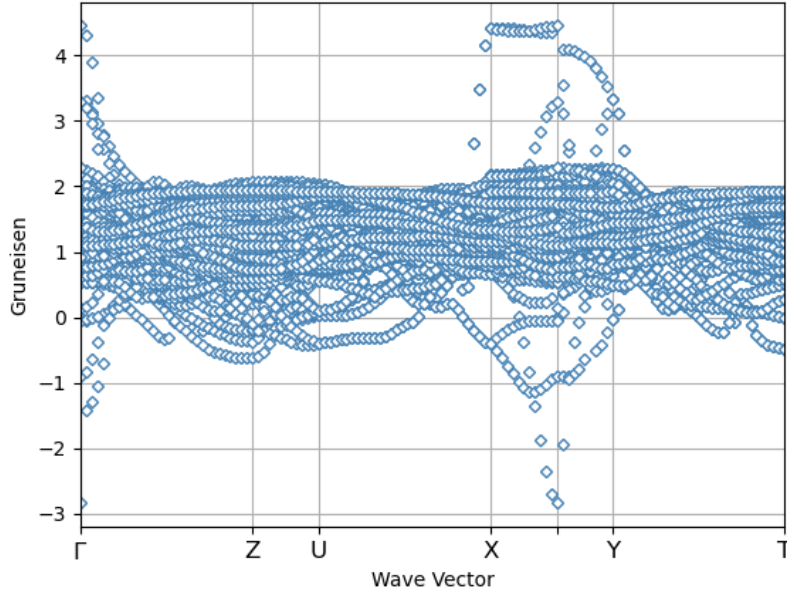


**Figure 2.9:** The computed mode Grüneisen parameters as a function of the wavevector.

The solid curves in Fig. 2.10 are the computed resistivity values along the principle axes at a carrier concentration of  $1 \times 10^{18} \text{h}^+ / \text{cm}^3$ . Both the magnitude and anisotropy of the predicted resistivities agree well with the single crystal data.

The ratio of the resistivity of  $\text{Ca}_5\text{In}_2\text{Sb}_6$  measured parallel and perpendicular to the crystal growth direction is compared in Table 2.4 against other highly anisotropic single crystals. Both  $\text{Ca}_5\text{In}_2\text{Sb}_6$  and  $\text{CsBi}_4\text{Te}_6$  contain 1D covalent chains, with parallel and perpendicular defined relative to the chain direction. For the layered compounds listed, parallel refers to in-plane and perpendicular is out-of-plane. This shows that  $\text{Ca}_5\text{In}_2\text{Sb}_6$  possesses more anisotropic resistivity than the tetradyte compounds  $\text{Bi}_2\text{Te}_3$  and  $\text{Sb}_2\text{Te}_3$ , but less than the incredibly anisotropic  $\text{CsBi}_4\text{Te}_6$ .  $\text{Mg}_3\text{Sb}_2$  - sometimes classified as a Zintl phase - exhibits relatively isotropic electronic transport (both experimentally and in DFT modeling [127]). Even though there are hundreds of thermoelectric materials with anisotropic structures, experimental data remains rare. In almost all cases, the “perpendicular” data is exceedingly difficult to obtain and it is often less reliable than the parallel measurements.

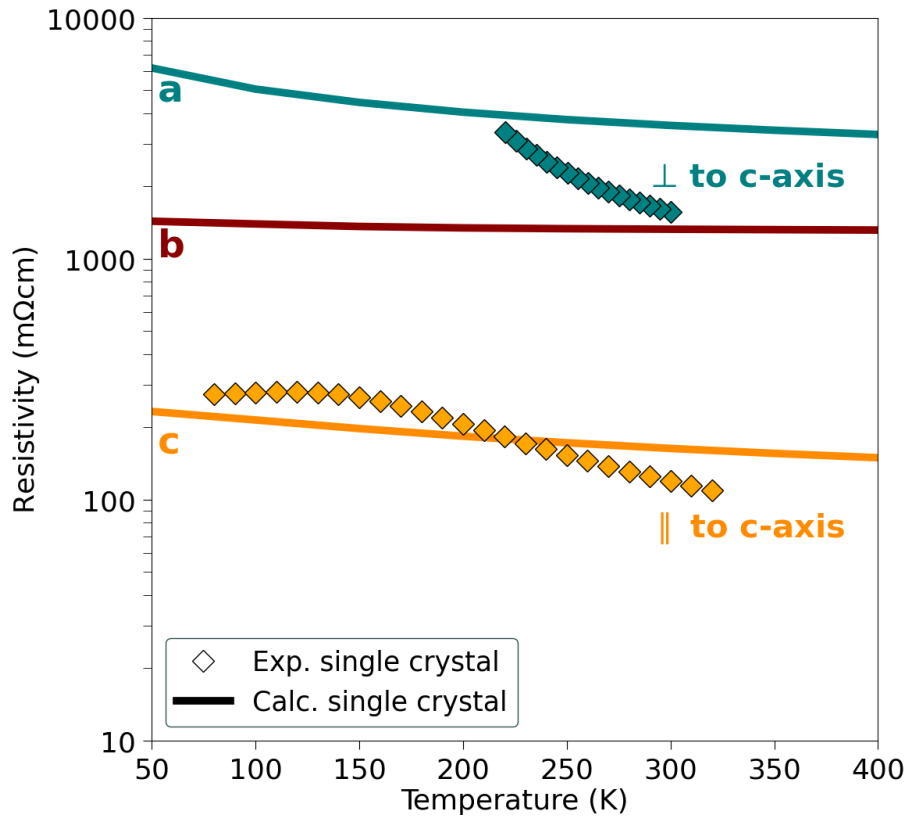


**Figure 2.10:** Experimental resistivity of  $\text{Ca}_5\text{In}_2\text{Sb}_6$  crystals measured perpendicular and parallel to the  $c$ -direction. The solid curves are the computed resistivity at a carrier concentration of  $1 \times 10^{18}\text{h}^+/\text{cm}^3$ .

This limitation is sometimes due to geometric constraints, as in the current study, or due to imperfections such as stacking faults in the crystals [147, 148], or the use of a textured polycrystal instead of a single crystal, which introduces grain boundaries. This highlights the continued need for significant advances in both characterisation techniques and crystal growth to help fill the gaps in our knowledge of anisotropic electronic transport in complex thermoelectric materials.

## 2.5 CONCLUSION

First principles modeling was used to show that the Zintl compound  $\text{Ca}_5\text{In}_2\text{Sb}_6$  has extremely anisotropic electrical resistivity due to light effective mass in the  $c$ -direction, parallel to its chain-like anionic sub-

Compound	$\rho_{\perp}/\rho_{\parallel}$ (200K)	$\rho_{\perp}/\rho_{\parallel}$ (300K)	Ref.
$\text{Ca}_5\text{In}_2\text{Sb}_6$ (1D)	18.6	13.1	[This work]
$\text{CsBi}_4\text{Te}_6$ (1D)	127	86.7	[126]
$\text{Bi}_2\text{Te}_3$ (2D)	–	6.1	[125]
$\text{Sb}_2\text{Te}_3$ (2D)	–	1.8	[149]
$\text{PbBi}_4\text{Te}_7$ (2D)	5.7	4.3	[150]
$\text{PbSb}_2\text{Te}_4$ (2D)	12.0	10.1	[150]
$\text{Mg}_3\text{Sb}_2$ (2D)	0.50	0.49	[127]
$\text{SnSe}$ (2D)	–	5.0	[124]

**Table 2.4:** Ratio of electrical resistivity perpendicular ( $\rho_{\perp}$ ) and parallel ( $\rho_{\parallel}$ ) to the crystal growth direction at 200 and 300K for selected bulk materials with quasi 1D or 2D crystal structures.

structure. The electrical resistivity and carrier concentration were measured on a single crystal micro-ribbon that was cut perpendicular to the  $c$ -direction. This data was compared against resistivity values collected on a single crystal parallel to the  $c$ -direction, yielding experimental confirmation of the predicted anisotropic electronic resistivity. A 13–18 $\times$  increase in conductivity was observed parallel to the  $c$ -direction. DFT predicts a significantly enhanced thermoelectric FoM parallel to the  $c$ -direction, assuming that the lattice thermal conductivity is isotropic. The latter assumption was supported by the calculated speed of sound tensor and the measured thermal expansion coefficients, both of which were found to be relatively isotropic. This study is also the first experimental confirmation of quasi-1D electronic transport in a Zintl compound thermoelectric material. Further, it serves as proof-of-concept for using micro-ribbons extracted from larger single crystals to evaluate thermoelectric properties in specific crystallographic directions. This process can potentially be applied to other compounds in the same manner to bridge the gap between experimental and computational evidence for anisotropic transport in Zintl compounds.

Nevertheless, it is crucial to approach the theoretical method employed in this study with caution, especially in view of its predictive nature. In this work, polycrystalline experimental results were fitted using a modified version of CRTA. In a second stage, theoretical results for single crystals (using the same methodologies and parameters as for polycrystals) were compared with experimental results in specific

directions. However, the reliability of the models used for the initial fitting, as elaborated in Sec. 2.2, has recently come under scrutiny [111]. Specifically, it has been demonstrated that the reliability of the temperature dependence associated with these diverse mechanisms and used in the model is questionable. Although our results are supported by the fitting with experimental data, applying these models to predict transport properties in novel materials demands extreme caution. After this study, alternative methodologies, such as AMSET [53], have emerged, demonstrating enhanced robustness in computing large-scale systems of this nature. We recommend the interested reader to explore these advancements for more effective calculations in similar contexts.



High mobility *p*-type transparent conducting materials (TCMs) have eluded researchers for decades. The unlikely bedfellows of good optical transparency (a wide band gap  $> 3\text{eV}$  and above 90% visible transmission), high valence band dispersion (typically requiring carrier effective mass  $< 0.5m_e$ ) and correct point defect chemistry (facile and controllable generation of electron-holes up to  $10^{21}\text{ cm}^{-3}$ , depending on applications) prove difficult to unite. In fact, these strict requirements preclude the vast majority of materials from ever displaying *p*-type transparent conducting properties. Early efforts focused on the development of *p*-type *oxides*, such as  $\text{CuAlO}_2$  [12], attempting to mimic the wide optical band gap of the *n*-type transparent conducting oxides. However,  $\text{CuAlO}_2$  and other delafossite materials are plagued by low mobility and conductivity due to the polaronic nature of the holes generated in these systems, which are bound to Cu states at the valence band maximum (VBM) [151–162].

Several other oxides have been considered as *p*-type transparent conductors with varying degrees of success: Li-doped NiO can reach hole concentrations on the order of  $1 \times 10^{21}\text{ cm}^{-3}$  and conductivity up to  $11\text{ S cm}^{-1}$ , but mobility is less than  $0.05\text{ cm}^2\text{ V}^{-1}\text{ s}^{-1}$  and transmission drops to 50% upon doping [163]; SnO is a reasonably good *p*-type TCM, with mobility around  $7\text{ cm}^2\text{ V}^{-1}\text{ s}^{-1}$  at  $1 \times 10^{17}\text{ cm}^{-3}$  carriers, and can also be doped *n*-type, but incurs stability issues due to the presence of Sn(II) (a problem which pervades ternary Sn(II) materials also) [11, 164]; quasi-closed shell  $d^3$  and  $d^6$  materials such as Sr-doped  $\text{LaCrO}_3$  and the  $\text{ZnM}_2\text{O}_4$  spinels ( $M = \text{Co, Rh, Ir}$ ) have been investigated as TCMs, exploiting the large crystal field splitting between  $e_g$  and  $t_{2g}$  states to engineer transparency, but their mobilities and conductivities routinely fall short of requirements [165, 166]; and  $\text{Ba}_2\text{BiTaO}_6$ , which shows excellent mobility (up to  $30\text{ cm}^2\text{ V}^{-1}\text{ s}^{-1}$ ) due to strong Bi  $6s^2 - \text{O } 2p$  interaction at the valence band (VB), but the carrier density is limited to  $1 \times 10^{14}\text{ cm}^{-3}$  [13, 167]. Therefore, research into *non-oxides* has taken centre stage in recent years [168–173], in the hope that greater valence band delocalisation and bond covalency can improve hole mobility

while simultaneously generating enough carriers to enable degenerate conductivity.

One such material is copper iodide, CuI, first discovered in 1907 by the “father of transparent conductors” Karl Bädeker [174] and now enjoying somewhat of a renaissance. It crystallises in the cubic zincblende structure below 643 K (Fig. 3.1), possesses an optical band gap of around 3 eV, displays native *p*-type conductivity, and consistently shows one of the highest Figures of merit,  $\Phi$ ,<sup>1</sup> for any *p*-type transparent conductor (over 60 000  $\text{M}\Omega^{-1}$  for S-doped CuI) [175–177]. It has a disperse, isotropic VBM (Fig. 3.2), with an average light hole parabolic effective mass of around  $0.21m_e$ , indicative of reasonably high hole mobility. The VBM is formed by the interaction of Cu  $3d t_2$  and I  $5p$  orbitals, while the conduction band minimum is formed by the interaction of Cu  $4s$  with I  $5s$  orbitals [178, 179], as shown schematically in the molecular orbital (MO) diagram in Fig. 3.3.

In addition to its rather attractive electronic structure, the simplicity of CuI is another strong factor in its revival in popularity. Good quality thin films can be deposited via relatively straightforward techniques such as vaporising iodine onto thin films of copper (à la Bädeker) [180], solid- and solution-based iodisation reactions [181–183] and ink-jet printing,[184] while more advanced techniques such as pulsed laser deposition (PLD) [185], molecular beam epitaxy (MBE) [186], and magnetron sputtering are beginning to gain traction [176]. Stability of films in air and to thermal cycling can be improved by encapsulation with amorphous  $\text{Al}_2\text{O}_3$  [185, 187] to prevent the oxidation of Cu(I) to Cu(II). Single crystal growth of CuI is reported more sporadically and over a much narrower range of charge carrier concentrations [188, 189]. In terms of devices and applications, CuI has been successfully used in thin film transistors (TFTs) with high operational stability and efficiency [190] while CuI nano-particle inks have contributed to improvements in high resolution X-ray imaging technology [191]. This

<sup>1</sup> Generally, the figure-of-merit (FoM) is calculated as the ratio between electrical conductivity  $\sigma$  and the visible absorption coefficient  $\alpha$ :

$$\Phi = \frac{\sigma}{\alpha} = \frac{-1}{R_s \ln(T_{vis} + R)}, \quad (3.1)$$

where  $T_{vis}$  is transmission and  $R_s$  is the sheet resistance, related to conductivity and thickness  $d$  by:

$$R_s = \frac{1}{\sigma d}. \quad (3.2)$$

manufacturing simplicity is further enhanced by its strong compatibility with various  $n$ -type oxides (such as ZnO, AgI, BaSnO<sub>3</sub>, and NiI<sub>2</sub>), positioning CuI as an optimal contender for combined  $n$ - and  $p$ -type applications [192–198].

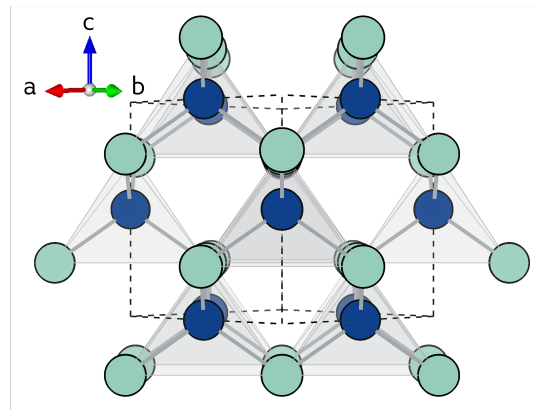


**Figure 3.1:** Zincblende crystal structure of CuI, viewed along the face diagonal. Cu and I atoms in blue and green, respectively. Cu have tetrahedral coordination, shown in grey.

Despite this fashionable return to the forefront of  $p$ -type TCM research, the charge transport behaviour of CuI is poorly understood. Experimental reports show no clear trend between hole mobility and carrier concentration, while little computational work has been undertaken on this subject. In this work, the intrinsic limits of CuI as a high-mobility transparent conductor are investigated from first-principles calculations and state-of-the-art charge carrier transport modelling. The different contributions to the overall scattering rate are analysed using two separate approaches, where it is found that scattering from phonons and ionised impurities dominate at either end of the charge carrier concentration range, respectively. This chapter is based on Ref. [99].

### 3.1 CRYSTAL AND ELECTRONIC STRUCTURE

The structural properties (lattice parameter, lattice angle and Cu–I bond length) of CuI are summarised in Table 3.1, where good agreement is found between the calculated values and both the experimental and computational literature. The PBEsol lattice parameters are slightly underestimated compared to room temperature neutron powder diffraction measurements by Keen *et al.* [199], while the PBE0 results show

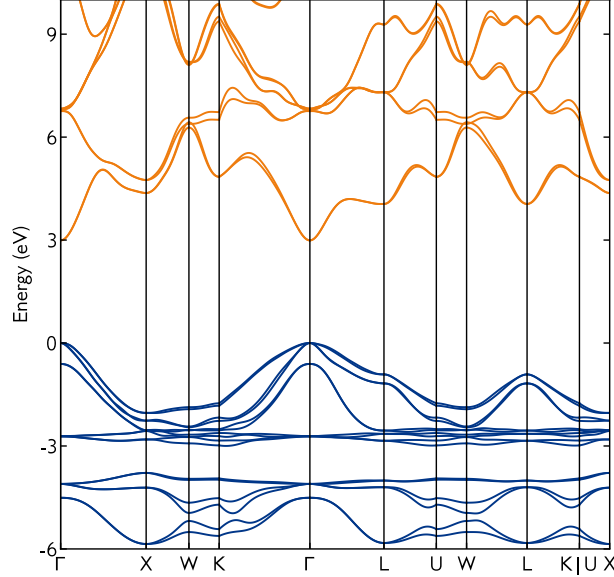


**Figure 3.2:** Electronic band structure of CuI. Calculated using the PBE0 hybrid functional with the inclusion of spin-orbit coupling (SOC).

closer agreement. Low temperature diffraction data is scarcely reported, but is expected to yield lattice parameters closer to the PBEsol results. Thin film CuI often displays slightly larger lattice parameters (6.06 Å from Moditswe *et al.* [200]) owing to tensile strain between film and substrate.

Parameter	Exp [199]	PBE0	PBE0 lit. [179]	PBEsol
$a$ (Å)	6.05	6.08	6.07	5.95
$\alpha$ (°)	90.0	90.0	90.0	90.0
Cu-I (Å)	2.57	2.63	2.62	2.58
Band gap (eV)	2.95 [201]	2.99	2.97	0.95
SOC splitting energy (eV)	0.64 [202]	0.63	–	0.47
Hole conductivity effective mass ( $m_0$ )	–	0.61	–	0.72

**Table 3.1:** Structural and band structure properties of CuI.

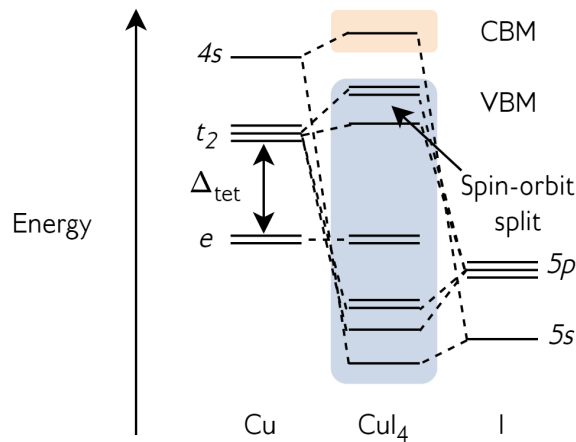


**Figure 3.3:** Schematic molecular orbital (MO) diagram of CuI. Upon the inclusion of SOC, further splitting occurs on the  $t_2 - 5p$  MOs into light and heavy hole channels and a spin-orbit split-off band, as seen in the band structure.

As shown in Table 3.1, a direct band gap of 2.99 eV at  $\Gamma$  is calculated with the PBE0 functional including spin-orbit coupling effects (PBE0+SOC, Fig. 3.2), which is in good agreement with experimental values obtained from a variety of measurements: pressure-dependent optical absorption from Ves *et al.*, 2.95 eV [201]; transmission spectra from Storm *et al.*, 3.11 eV [185]. This also matches well previous hybrid DFT calculations, with Yu *et al.* most recently reporting a value of 2.97 eV [179]. On the other hand, the direct band gap computed with PBEsol is severely underestimated as is often the case in semi-local DFT. The hole conductivity effective mass (or the transport mass) determined from PBE0 calculations is slightly lower than that from PBEsol. Semi-local DFT functionals often struggle to accurately describe localised  $d$  states (regardless of electronic occupation) without the inclusion of the Hubbard  $U$  parameter, so a mismatch in the transport effective mass is not unexpected.

In CuI, the inclusion of SOC has a direct effect on the band edges. Fig. 3.4(a) illustrates that without SOC, the VBM of CuI has three degenerate bands. The addition of SOC results in the lifting of the degeneracy, with one of the bands (the split-off band) dropping in energy, a common feature of zincblende semiconductors. As for the band gap, PBEsol tends to undervalue the spin-orbit splitting at the  $\Gamma$ -point of the VBM which is around 470 meV whereas the value computed

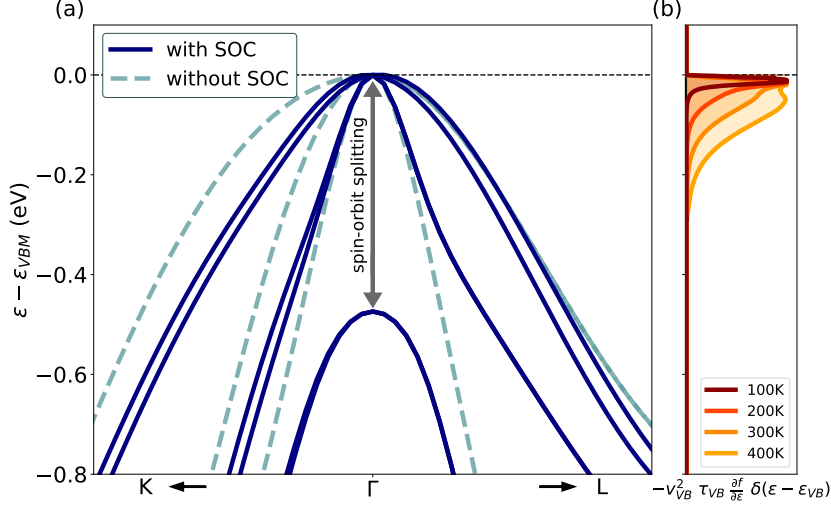


**Figure 3.4:** (a) Top of the valence bands of CuI around  $\Gamma$  with and without SOC as computed with the PBEsol functional. (b) The normalised function  $-v_{\text{VB}}^2 \tau_{\text{VB}} \frac{\partial f}{\partial \epsilon}$ , convoluted with  $\delta(\epsilon - \epsilon_{\text{VB}})$  in the valence band at different  $T$ . In this expression,  $v_{\text{VB}}$  and  $\tau_{\text{VB}}$  stand for the carrier velocity and lifetime in the VB,  $\frac{\partial f}{\partial \epsilon}$  is the derivative of the Fermi-Dirac distribution function with respect to the energy and  $\delta$  the Dirac delta function. By integrating this function, the relaxation time approximation (RTA) hole mobility is obtained.

with PBE0 is around 630 meV, in excellent agreement with the value of 640 meV determined experimentally by Blacha *et al.* using hydrostatic pressure-dependent thin film absorption [202].

### 3.2 CHARGE TRANSPORT

Two methods are used to simulate charge transport in CuI: an iterative Boltzmann transport equation (**IBTE**) solution to calculate phonon-limited mobilities using the **Abinit** code [48, 52, 80, 81] and a phenomenological model (**AMSET**) that calculates scattering rates for acoustic deformation potential (ADP), piezoelectric (PIE), ionised impurity (IMP) and polar optical phonon (POP) scattering, utilising low-cost inputs from first-principles calculations using the **VASP** code [53, 203–208]. While IBTE provides a high-quality representation of transport properties, AMSET complements the analysis by evaluating the effects of impurities but also by providing an additional analysis of

the phonon scattering mechanisms by decoupling the different contributions. AMSET also offers the advantage of using hybrid functionals, which are difficult to employ in fully first-principles IBTE calculations due to the computational cost and absence of implementations able to compute electron-phonon (e-ph) quantities within density functional perturbation theory (DFPT).

### 3.2.1 IBTE

The lifting of degeneracy resulting from the addition of SOC has a clear impact on hole transport. Indeed, for transport in semiconductors, only energies near the top of the VBM are relevant [209]. As depicted in Fig. 3.4(b), the function  $-v_{\text{VB}}^2 \tau_{\text{VB}} \frac{\partial f}{\partial \epsilon} \delta(\epsilon - \epsilon_{\text{VB}})$ , which once integrated provides direct access to the RTA hole mobility, quickly approaches zero for energies further from the Fermi level. This means that only the electronic states covered by this function participate in the hole transport. As a result, the inclusion of SOC in CuI leads to the complete removal of a scattering channel, as the split-off band is no longer included in the energy windows responsible for transport, even at higher temperatures. Using Abinit, we obtain a converged IBTE mobility of  $162 \text{ cm}^2 \text{ V}^{-1} \text{ s}^{-1}$  at 300 K with SOC and dynamical quadrupoles ( $Q^*$ ) using  $162 \times 162 \times 162$   $\mathbf{k}$ - and  $\mathbf{q}$ -point grids (refer to Fig. 3.5(b)). The inclusion of SOC leads to an enhancement in mobility by removing a scattering channel. Note that, despite the increase in mobility due to the effect of SOC on the electronic bands, its effect on phonons remains negligible on both phonon band structure and mobility, as shown in Figs. 3.5(a) and (b). The integration of  $Q^*$ , the next order of correction to dynamical dipoles, in the computation is also necessary to obtain accurate results [48, 52], preventing an error of about 15% in the case of CuI.

The DFPT phonon dispersion of CuI is shown in Fig. 3.6(a) and shows good agreement with the experimental frequencies reported in the literature [210, 211]. The minor disparity, such as for the LO-TO splitting, may be attributed to the challenge of precisely capturing the dielectric constants in CuI, as discussed in the next section. This plot is accompanied by the corresponding spectral decomposition of the hole scattering rates at different  $T$  (Fig. 3.6(b)), and shows that the high-frequency longitudinal optical mode  $T_2$  (LO) is the main contributor to the e-ph scattering in CuI. Although the spectral decomposition

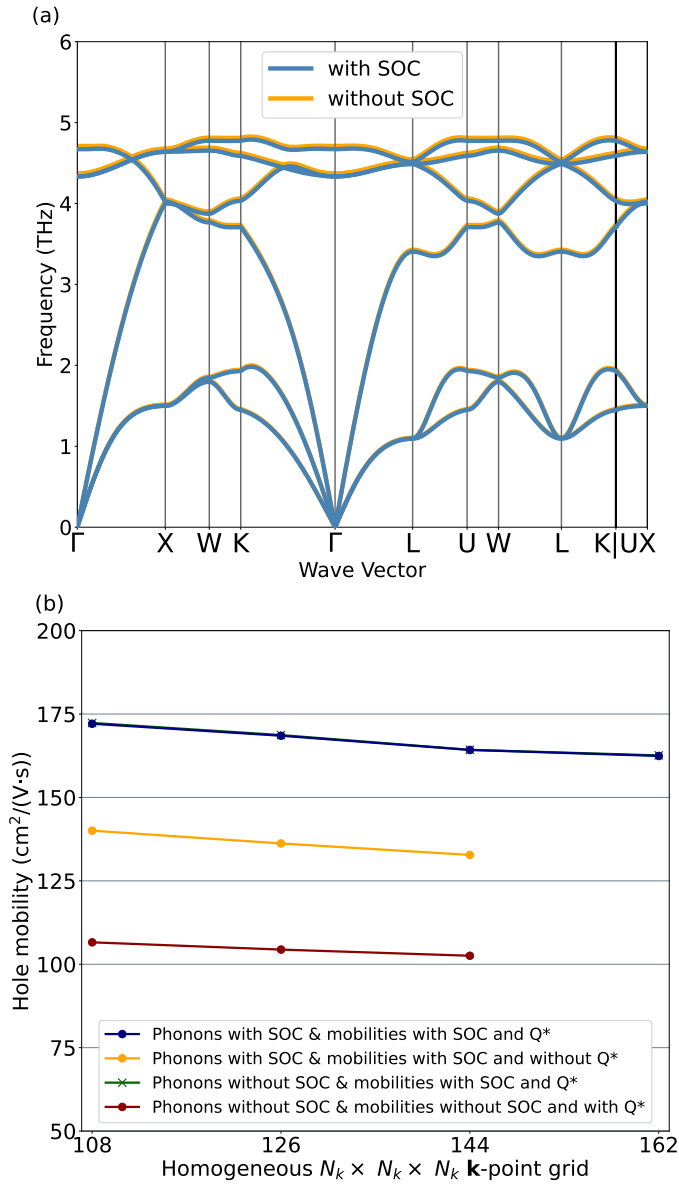


**Figure 3.5:** (a) Phonon dispersion curves for CuI with and without SOC. (b) IBTE hole mobility in CuI as a function of the  $k$ - and  $q$ -point grids at 300K using different treatments (the density of  $q$ -points is the same as the density of  $k$ -points). Due to their long-range nature, quadrupolar interactions must be taken into account for an accurate description of the scattering potential and mobilities [48, 52]. SOC also plays an important role in the transport properties of CuI and must also be taken in account. In this plot, SOC+ $Q^*$  mobilities obtained with SOC phonons, SOC+no $Q^*$  mobilities with SOC phonons, SOC+ $Q^*$  mobilities obtained with noSOC phonons and noSOC+ $Q^*$  mobilities obtained with noSOC phonons are represented in blue, orange, green and red, respectively. The absence of SOC in the phonon calculations does not affect the mobility results, as the blue and green curves overlap.

encompasses both short- and long-range phonons, transport in CuI is mainly influenced by the latter ones (near  $\Gamma$ ). This is due to the unique and curvy pocket present at the VBM of the electronic band structure of the material, allowing only transitions with small momentum transfer  $q$ . Fig. 3.7 represents the  $T_2$  (LO) phonon mode of CuI at  $\Gamma$  (towards the X direction) with the Cu and I atoms moving in phase opposition with twice the displacement amplitude for Cu. The relative contribution to scattering increases with T due to the growing number of phonons that are thermally excited, as evidenced by the area under the curve of Fig. 3.6(b) expanding from 100 K to 400 K. This results in a decrease of the e-ph IBTE mobility with temperature, as shown in Fig. 3.8.

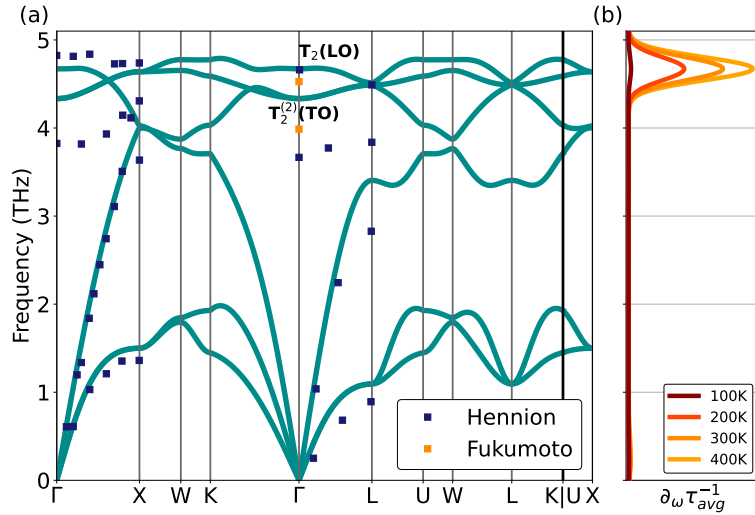


**Figure 3.6:** (a) CuI phonon dispersion computed with SOC and the PBEsol functional with experimentally reported frequencies overlaid [210, 211]. (b) Spectral decomposition of the hole scattering rates as a function of frequency at different temperatures.

### 3.2.2 AMSET

Fig. 3.9 shows the hole mobility calculated with AMSET at low and high carrier concentrations. The mobility is split by scattering mechanism, and the total mobility is plotted as the reciprocal sum of each component (via Matthiessen's rule). At a carrier concentration of  $1 \times 10^{16} \text{ cm}^{-3}$  (Fig. 3.9a), scattering from polar optical phonons (POP) is predicted

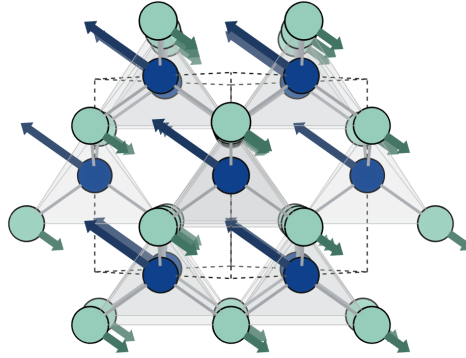


**Figure 3.7:** Structure of CuI showing the atomic displacements corresponding to the longitudinal optical phonon mode at the  $\Gamma$  point (towards the X direction), viewed along the face diagonal; Cu and I atoms in blue and green, respectively.

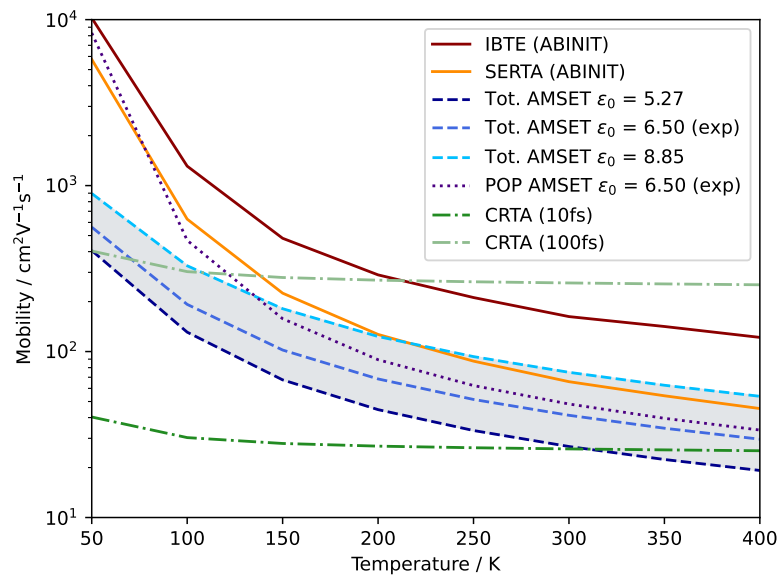


**Figure 3.8:** CuI hole mobility against T computed with different methods. This graph shows the influence of dielectric constants on the results obtained with AMSET but also demonstrates the effect of the use of the SERTA in the calculation of POP with AMSET whose results are close to the results obtained with this same approximation in Abinit.

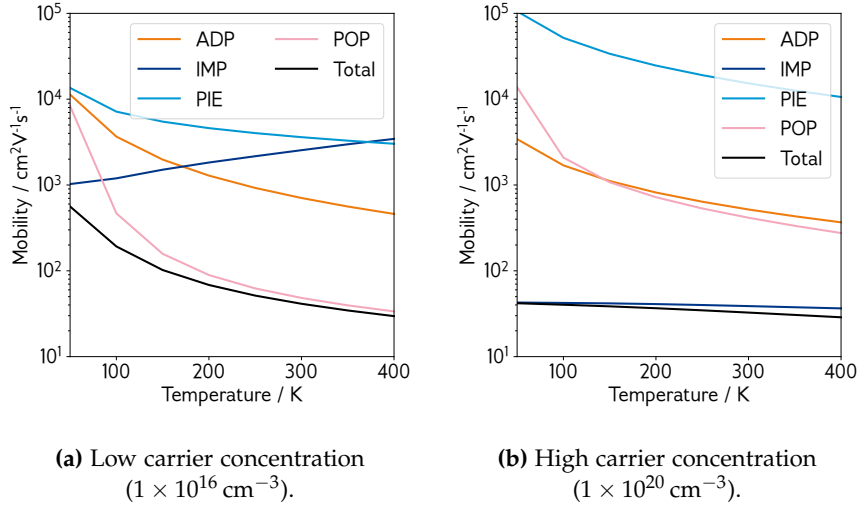


**Figure 3.9:** CuI hole mobility as a function of temperature at two carrier concentrations. Coloured lines represent mobility contributions from each type of scattering: ADP is acoustic deformation potential scattering (orange); IMP is ionised impurity scattering (dark blue); PIE is piezoelectric scattering (light blue); POP is polar optical phonon scattering (pink); Total is the reciprocal sum of these contributions (black).

to dominate the hole mobility, yielding a total room temperature hole mobility of  $41.3 \text{ cm}^2 \text{ V}^{-1} \text{ s}^{-1}$ . Scattering from acoustic deformation potentials (ADP), piezoelectric effects (PIE) and ionised impurities (IMP) is essentially negligible at low concentrations compared to POP scattering. The piezoelectric constant calculated from DFPT is in excellent agreement with experiment ( $0.10 \text{ C m}^{-2}$  against  $0.13 \text{ C m}^{-2}$ ) [212] and confirms that PIE scattering does not compromise the mobility, despite the non-centrosymmetric inversion native to the zincblende crystal structure.

Moving to a higher carrier concentration of  $1 \times 10^{20} \text{ cm}^{-3}$  (Fig. 3.9b), the effects of both POP and PIE scattering are diminished further, while ionised impurities begin to control the charge transport behaviour in CuI – a room temperature hole mobility of  $32.6 \text{ cm}^2 \text{ V}^{-1} \text{ s}^{-1}$  is predicted. IMP (and indeed POP scattering in the AMSET implementation) scattering is largely determined by the value of the static dielectric response of a material, i.e. its ability to screen electric charge. For CuI, calculated dielectric constants range from 5.27 to 8.85, dependent on the flavour of DFT functional and the method used to calculate the high- and low-frequency responses, and are shown in Table 3.2. Meanwhile,

an experimental dielectric response of 6.5 is reported by Hanson *et al.* [212]. Accurate calculation of the dielectric response in tetrahedral semiconductors is benchmarked by Skelton *et al.* [213] who note that semi-local DFT nearly always overestimates the high-frequency dielectric response, while hybrid functionals nearly always underestimate the high-frequency dielectric response, with PBE0 performing worse than HSE06. Considering the tetrahedral zincblende structure of CuI, it is reasonable to assume that similar trends are followed here. Due to the fact that the dielectric constant is quite small for CuI, these quite large percentage errors in  $\epsilon_0$  have significant effects on the POP and IMP scattering rates and therefore on the mobility computed with AMSET as shown in Fig. 3.8. To this end, the dielectric constant used in the AMSET calculations in Figs. 3.9 and 3.10 is that determined from experiment (6.5, where  $\epsilon_{\text{ionic}}$  is set as the calculated value of 1.1 from DFPT, and the remainder is assigned to  $\epsilon_{\infty}$ ). More sophisticated methods for calculating the dielectric response that can accurately model excited state features, such as GW (Green’s function  $G$  with screened Coulomb interaction  $W$ ) and BSE (Bethe-Salpeter equation) implementations, would provide a clearer picture [214] but exceed the scope of the current work.

Details	$\epsilon_{\text{ionic}}$	$\epsilon_{\infty}$	$\epsilon_0$
PBEsol DFPT; PBEsol IP-RPA*	1.10	7.75	8.85
PBEsol DFPT; PBE0 IP-RPA*	1.10	4.17	5.27
PBE0 FD; PBE0 IP-RPA*	1.65	4.17	5.82
Materials Project: PBE	0.87	6.82	7.69
Li <i>et al.</i> [215]: PBE	1.53	4.77	6.30
Hanson <i>et al.</i> (exp.) [212]	–	–	6.5

**Table 3.2:** Dielectric constants calculated using a variety of methods; \* denotes calculations from this work; DFPT (density functional perturbation theory) or FD (finite differences method) calculations were used to determine the low-frequency,  $\epsilon_{\text{ionic}}$ , response, while IP-RPA (independent particle random phase approximation) optical calculations were used to determine the high-frequency,  $\epsilon_{\infty}$ , response. Further details can be found in the computational details (App. A.4).

### 3.2.3 Combined approach

While AMSET correctly predicts the relative importance of the different scattering mechanisms, the low concentration regime phonon-limited mobility predicted by AMSET and the IBTE method varies by a factor of 4. As POP scattering is the primary mobility-limiting mechanism in this material at low carrier concentrations, this overestimation of the scattering rate results in mobility values that are lower than those reported in the experimental literature (notably the single crystal result from Chen *et al.*) [188]. One way to explain this is the inelastic treatment of POP in AMSET. Indeed, AMSET approximates POP scattering using the self-energy relaxation time approximation (SERTA), which as part of its formalism only considers scattering in the forward direction relative to charge carrier motion. The omission of backward scattering can lead to an underestimation of phonon-limited mobility, the extent of which varies between materials depending on the complexity of the band edge (single band or multi-degenerate), the effective mass, and spin-orbit effects [42, 45].

The comparison between phonon-limited mobility and experimental results can be challenging since most calculations do not consider impurities or defects. While SERTA serves as an approximation of IBTE, it is advisable to prioritise the latter due to its comprehensive nature, even if certain SERTA results appear closer to experimental data. For instance in Si, the computed electron mobility with the two methods fall within the range of experimentally reported mobilities [48] although the hole mobility is overestimated by both approaches – only when performing simulations using the experimental lattice parameter and fitting the band structure to the experimental hole effective mass is agreement with experimental mobility recovered using the IBTE approach [45]; for SiC the IBTE performs better than the SERTA for electron mobility (SERTA underestimates by around 30%), while they straddle the upper and lower side of experimental results for the hole mobility, respectively [216] and for GaAs both the implementations provide rather unreliable results, not helped by the large range of experimental mobilities reported [98]. Surveying over more than 50 materials, Claes *et al.* [42] show that differences in computed mobility using IBTE and SERTA can reach up to 60% and that the differences are often particularly large for binary halides with low  $\omega_{\text{POP}}$  such as NaI, CsI and TlBr. The general trend is that SERTA will, if at all, underestimate phonon-limited mobilities compared to the exact IBTE

results. Crucially, it is difficult to predict *a priori* the severity of the underestimation.

To this end, mobility values obtained using the SERTA under Abinit are compared with those acquired using AMSET, as illustrated in Fig. 3.8. It is found that the agreement between the two SERTA results is close, and this indicates that POP scattering is potentially overestimated in AMSET for CuI due to the SERTA. Therefore, we propose that the mobility limit in CuI is determined in the low concentration regime by IBTE e-ph scattering and in the high concentration regime by ionised impurity scattering.

Fig. 3.10 shows the hole mobility determined by summing the e-ph contribution from IBTE and the IMP contribution from AMSET assuming the validity of Matthiessen's rule on mobility ( $\frac{1}{\mu_{\text{IBTE+IMP}}} = \frac{1}{\mu_{\text{IBTE}}} + \frac{1}{\mu_{\text{IMP}}}$ ). While this does not represent an exact solution to the BTE, it provides a reasonable upper limit to the mobility that is achievable in CuI. The e-ph IBTE and total AMSET drift mobilities (computed using the experimentally determined dielectric constant of 6.5) are also shown, as are experimental Hall mobility values from the literature. As the Hall factor ( $r_{\text{H}}$ ) is close to 1 for CuI and CuBr [217, 218], it is reasonable to compare the simulated drift mobility with experimental Hall mobility ( $r_{\text{H}}\mu \sim \mu_{\text{H}}$ ).

The combined mobility from IBTE and IMP acts as an upper limit to hole mobility in CuI, within which the presently available data from experiment falls. First, single crystal data is considered (orange stars in Fig. 3.10), which should represent the highest achievable experimental mobility and truest comparison to simulation, as only the intrinsic, material-dependent scattering processes should be present. It is well-known however that single crystal size, cleanliness and surface defects can all impact mobility measurements. Record single crystal mobility is reported by Chen *et al.* [188] achieving a value of  $43.9 \text{ cm}^2 \text{ V}^{-1} \text{ s}^{-1}$  at a carrier concentration of  $4.3 \times 10^{16} \text{ cm}^{-3}$  in a sample of dimensions  $15 \times 10 \times 1 \text{ mm}$ . This is in the e-ph scattering limit, and suggests significant scope for improvement in mobility at low carrier concentrations. Other single crystals have been synthesised by Lv *et al.* [189], obtaining a sample of similar size and carrier concentration but with a reduced mobility of  $12.8 \text{ cm}^2 \text{ V}^{-1} \text{ s}^{-1}$  and Matsuzaki *et al.* [221], achieving mobility up to  $29 \text{ cm}^2 \text{ V}^{-1} \text{ s}^{-1}$  at low concentrations ( $2.0 \times 10^{14} \text{ cm}^{-3}$ ) and  $19 \text{ cm}^2 \text{ V}^{-1} \text{ s}^{-1}$  at carrier concentrations approaching the degenerate conductivity limit. By considering the POP scattering rate from AMSET as the dominant low concentration scattering mechanism, Chen's meas-

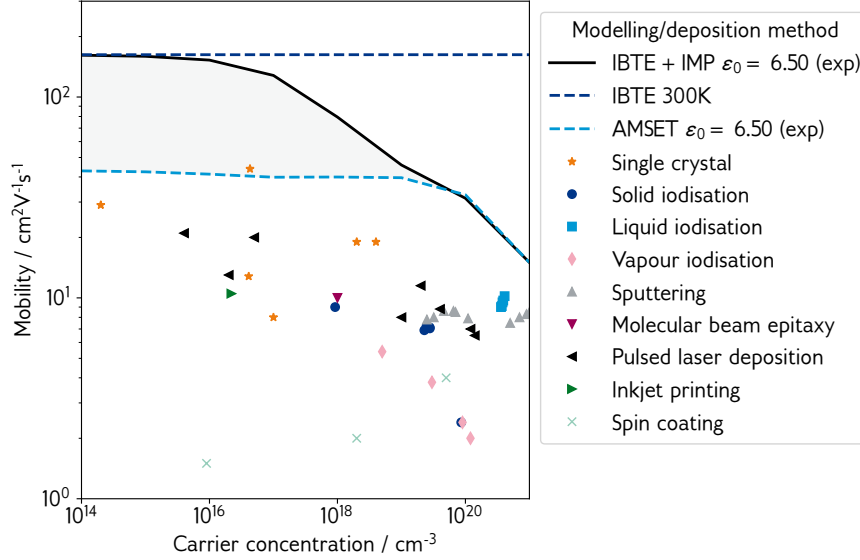


**Figure 3.10:** Experimental hole mobility as a function of carrier concentration, broken down by deposition method. Experimental data is reported in Refs. [176, 177, 180–182, 184–189, 219–222]. IBTE and AMSET drift mobilities overlaid as dashed lines; IBTE+IMP mobility ( $\frac{1}{\mu_{\text{IBTE+IMP}}} = \frac{1}{\mu_{\text{IBTE}}} + \frac{1}{\mu_{\text{IMP}}}$ ) overlaid as a filled black line; grey shaded region denotes space between AMSET-estimated upper limit and IBTE+IMP-estimated upper limit.

urement exceeds the predicted mobility. It is reasonable to assume that this single crystal measurement is within the “low” carrier concentration regime, as a rough calculation of the Mott criterion using the parabolic (transport) band edge effective masses and the experimental dielectric constant indicates a carrier density of  $8.5 \times 10^{17} \text{ cm}^{-3}$  ( $1.65 \times 10^{18} \text{ cm}^{-3}$ ). This failure of the SERTA to describe the low carrier density experimental datapoints was the first indication that a more sophisticated treatment of the e-ph scattering would be required for CuI.

Turning now to thin films, the record mobility measurement is more difficult to identify. Several papers report promising mobilities, even surpassing the  $43.9 \text{ cm}^2 \text{ V}^{-2} \text{ s}^{-1}$  from Chen *et al.*:  $35 \text{ cm}^2 \text{ V}^{-1} \text{ s}^{-1}$  at  $8.5 \times 10^{18} \text{ cm}^{-3}$  via liquid iodisation of metallic Cu from Wang *et al.* [223];  $35 \text{ cm}^2 \text{ V}^{-1} \text{ s}^{-1}$  to  $50 \text{ cm}^2 \text{ V}^{-1} \text{ s}^{-1}$  at concentrations in the region of  $1 \times 10^{18} \text{ cm}^{-3}$  via iodisation of metallic Cu on crystalline Si substrates from Madkhali *et al.* [224]; and  $110 \text{ cm}^2 \text{ V}^{-1} \text{ s}^{-1}$  at  $1.1 \times 10^{18} \text{ cm}^{-3}$  via MBE

on crystalline Si from Ahn *et al.* [225]. However, these measurements are from extremely thin films that have XRD peaks that can be attributed to the Cu and c-Si substrates, which themselves are extremely good charge carriers, making it difficult to decouple the transport properties of the substrate from those of the film. These results are therefore omitted from Fig. 3.10. Storm *et al.* [185, 187] report consistently high thin film mobility via pulsed laser deposition (PLD, purple triangles in Fig. 3.10) over a wide range of carrier concentrations, which comprises the most reliable thin film data available in the literature. At the higher end of the carrier concentrations reported, films deposited from sputtering and liquid iodisation appear to approach the mobility limit arising from ionised impurity scattering, peaking around  $10 \text{ cm}^2 \text{ V}^{-1} \text{ s}^{-1}$ . Across the entire carrier concentration range, the experimental results fall within the IBTE+IMP limit (and critically fall outside the SERTA+IMP, i.e., AMSET, limit), justifying our approach.

The final and perhaps most crucial point to consider is the electronic performance achievable via scalable synthesis methods. While PLD, MBE and sputtering offer reasonably high mobilities across the carrier concentration range, they are not commercially viable deposition techniques. Instead, inkjet printing, spin coating and, potentially, iodination reactions are likely to be the most industrially relevant. The hole mobilities reported from these methods seldom exceed  $10 \text{ cm}^2 \text{ V}^{-1} \text{ s}^{-1}$  regardless of carrier concentration, owing to the lower crystallinity of the films and subsequent grain boundary and interface scattering. Such CuI films are roughly on par with SnO mobility [11] but are beaten by  $\text{Ba}_2\text{BiTaO}_6$  ( $30 \text{ cm}^2 \text{ V}^{-1} \text{ s}^{-1}$ ) [13, 167] and the layered oxychalcogenide  $(\text{Cu}_2\text{S}_2)(\text{Sr}_3\text{Sc}_2\text{O}_5)$  ( $150 \text{ cm}^2 \text{ V}^{-1} \text{ s}^{-1}$ ) [14] and are still up to 2 orders of magnitude lower than the degenerately doped *n*-type transparent conductors ( $\text{In}_2\text{O}_3$   $130 \text{ cm}^2 \text{ V}^{-1} \text{ s}^{-1}$ ,  $\text{Ga}_2\text{O}_3$   $75 \text{ cm}^2 \text{ V}^{-1} \text{ s}^{-1}$ ,  $\text{SnO}_2$   $130 \text{ cm}^2 \text{ V}^{-1} \text{ s}^{-1}$ ,  $\text{BaSnO}_3$   $320 \text{ cm}^2 \text{ V}^{-1} \text{ s}^{-1}$  and  $\text{ZnSb}_2\text{O}_6$   $49 \text{ cm}^2 \text{ V}^{-1} \text{ s}^{-1}$ ) [6, 7, 226–228]. Despite this, CuI has been successfully used to make thin film transistors via solution-based and inkjet deposition with competitive switching ratios and current densities [184, 190, 229] and amorphous CuI thin-film transistors (TFTs) have been reported to outperform polycrystalline devices [230]. Such applications often require a lower carrier density than  $10^{20} \text{ cm}^{-3}$ , where the mobility of CuI can be significantly improved. The prediction of such a large scope for improvement in CuI mobility indicates that other scattering processes may also be in play, such as surface and grain boundary scattering, which could be mitigated as deposition and

device engineering process become more sophisticated. These results indicate that CuI will retain its position as the front-runner in the race for a marketable *p*-type TCM, and provide useful insights for quality control in CuI.

### 3.3 CONCLUSION

This study examined the suitability of CuI as a high performance *p*-type transparent conductor. Using sophisticated charge transport modelling, an upper limit to hole mobility as a function of carrier concentration was predicted, ranging from  $162 \text{ cm}^2 \text{ V}^{-1} \text{ s}^{-1}$  in the phonon-limited range to  $32.6 \text{ cm}^2 \text{ V}^{-1} \text{ s}^{-1}$  in the degenerately doped, ionised impurity-limited range. These results suggest significant scope for improvement in experimental mobility, particularly in the low to mid-concentration range, which could be achieved by mitigating surface and grain boundary scattering processes, and by further optimisation of synthesis conditions. The prospect of achieving samples with mobilities that closely align with our theoretical projections holds significant promise. Such progress has the capacity to yield a noteworthy two- to three-fold enhancement in the existing experimental FoM,  $\Phi$ , for CuI, thereby propelling it to a competitive stance alongside the finest *n*-type materials currently prevalent on the market. This work will act as a useful benchmark to experimental studies on CuI and related *p*-type transparent conductors, and indicates that there is still scope for enhanced opto-electronic performance.



POTENTIAL NEW STATE-OF-THE-ART P-TYPE  
MATERIALS IN TIN (II) OXIDES

Transparent conductive oxides (TCOs) have garnered significant attention due to their vast potential for application in various electronic devices, including solar cells, flat panel displays, and touch screens [3, 231, 232]. Recently, they have also been proposed for use in complementary metal-oxide-semiconductors (CMOS) or field-effect transistors (FETs) [233–235]. While *n*-type TCOs such as indium tin oxide (ITO), gallium oxide ( $\text{Ga}_2\text{O}_3$ ) or zinc oxide (ZnO) have been extensively researched and widely adopted [3, 5, 236, 237], developing *p*-type TCOs has proven to be a challenging task. This is primarily due to their low carrier mobilities, which are one order of magnitude lower than those of their *n*-type counterparts. The underlying reason lies in the typically flat valence bands of metal oxides, which are dominated by localised *p*-orbitals of oxygen atoms. However,  $\text{Sn}^{2+}$  oxides exhibit a departure from typical oxides in that they possess a metallic character in the valence band maximum (VBM) owing to the presence of lone pairs on tin atoms [238]. The formation of lone pairs and the resulting lighter hole effective masses are driven by the gain in energy resulting from the hybridisation between the anti-bonding state formed by the cation *s*-orbital and oxygen *p*-orbital with the *p*-state of tin, as depicted in Fig. 4.1.

However, it has been also demonstrated by Ha *et al.* [239] that the presence of  $\text{Sn}^{2+}$  alone does not guarantee a low effective mass; the crystalline structure also plays an important role. Indeed, the angle formed by the Sn–O–Sn bonds within the crystal structure has a strong influence on the effective mass of these oxides: when this angle approaches  $180^\circ$ , it promotes orbital overlap, leading to lower effective masses. But despite the intriguing range of properties associated with  $\text{Sn}^{2+}$ , tin typically favours the  $\text{Sn}^{4+}$  configuration. This is mainly due to the metallic *s*-orbitals being located above the oxygen *p*-states in the  $\text{Sn}^{2+}$  oxidation state. In addition,  $\text{Sn}^{2+}$ -based ternary oxides tend to compete with various other Sn–O–X phases with comparable formation energy [108].

Although the low band gap of SnO renders it less competitive for optical applications, the addition of a third element also helps to obtain more interesting optical properties. In this work, we choose to study the transport properties of 4 identified promising candidates that present a relatively good mix between phase stability, optical and transport properties:  $\text{K}_2\text{Sn}_2\text{O}_3$  (in the cubic (*c*) and rhombohedral (*r*) phases),  $\text{Rb}_2\text{Sn}_2\text{O}_3$  and  $\text{TiSnO}_3$  and compare them to SnO. In fact, previous works have already identified these materials as potential candidates based on effective mass calculations [62, 239] or, more recently, through the use of phenomenological mobility models [107, 108, 240]. In this study, we delve deeper into the understanding of the differences between these materials by employing a first-principles method that relies on the iterative solution of the Boltzmann transport equation, thereby assessing their significant potential. The relative importance of the electron-phonon (e-ph) coupling in these materials is also assessed using a new decomposition method of the scattering rates. Finally, a detailed analysis of the phonon modes with the most pronounced scattering effects on holes is performed.

#### 4.1 CRYSTAL STRUCTURES

Among the various  $\text{Sn}^{2+}$  oxides, the conventional SnO has been extensively studied both theoretically and experimentally. It possesses a tetragonal crystalline structure similar to  $\text{SnO}_2$ , but with a distinguishing layered arrangement as shown in Fig. 4.2(a). This distinction arises from the presence of a lone pair on the tin atom, resulting in different stacking patterns compared to  $\text{SnO}_2$ . In the case of SnO, the Sn-O-Sn layers are stacked along the *c*-axis, exhibiting relatively weak van der Waals interactions [241]. The structural properties of SnO obtained with GGA PBEsol are in good agreement with the experimental results [241–244], as shown in Table 4.2 but also with the numerous computational data obtained with various techniques [107, 245–248].

The other ternary tin oxides investigated in this study share a similar layered structure to SnO, except for *c*- $\text{K}_2\text{Sn}_2\text{O}_3$ , as seen in Fig. 4.2. Notably,  $\text{K}_2\text{Sn}_2\text{O}_3$  is slightly more stable in its cubic phase rather than the rhombohedral phase whereas  $\text{Rb}_2\text{Sn}_2\text{O}_3$  favours the rhombohedral configuration. Nevertheless, even in the cubic phase, the lone pairs of tin atoms tend to avoid each other within a three-dimensional Sn–O–Sn network. Finally, the rhombohedral structure of  $\text{TiSnO}_3$  is slightly different than those of *r*- $\text{K}_2\text{Sn}_2\text{O}_3$  and  $\text{Rb}_2\text{Sn}_2\text{O}_3$  as edge-sharing  $\text{TiO}_6$

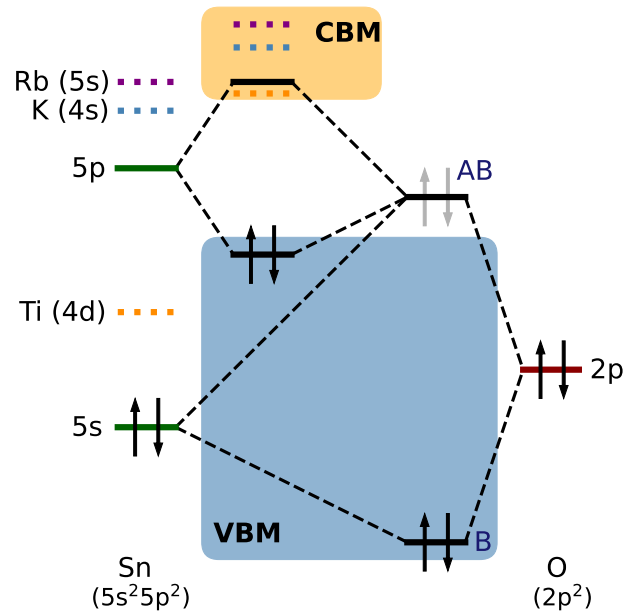


**Figure 4.1:** Schematic molecular orbital (MO) diagram of SnO. The contribution of the ternary atom in the four other systems is highlighted in blue, purple and orange for K, Rb and Ti, respectively

octahedra are present instead of hexagonal planar geometry between K/Rb and O. The structural properties of the ternary tin oxides are summarised in Tables 4.1 and 4.2, where good agreement is also found with experimental literature [250, 251] and other theoretical works [239, 240, 252].

#### 4.2 DECOMPOSITION OF THE SCATTERING RATES

One of the aims of this work is to gain a better understanding of the importance of e-ph coupling and the influence of the effective mass on the lifetime. To this end, a simple factorisation of the scattering rates into two parameters was carried out based on the self-energy relaxation time approximation (SERTA). In fact, the IBTE method, which provides

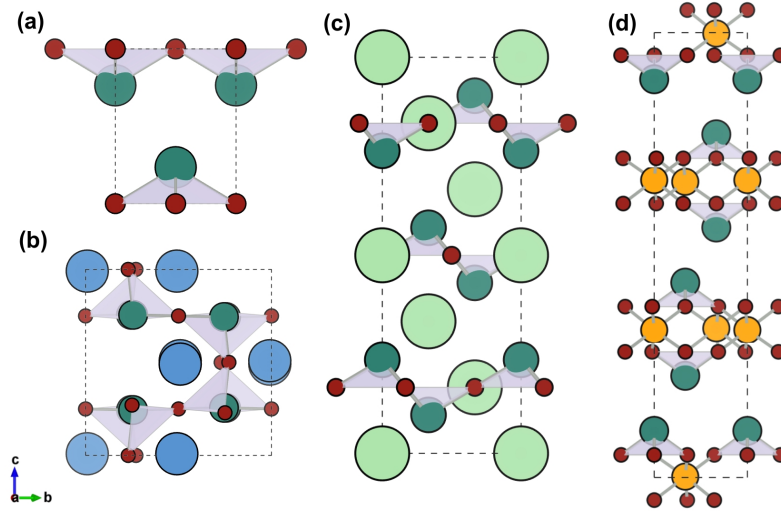


**Figure 4.2:** Crystal structures of (a) SnO, (b)  $c\text{-K}_2\text{Sn}_2\text{O}_3$ , (c)  $\text{Rb}_2\text{Sn}_2\text{O}_3$  and (d)  $\text{TiSnO}_3$ .  $r\text{-K}_2\text{Sn}_2\text{O}_3$  has the same rhombohedral structure as  $\text{Rb}_2\text{Sn}_2\text{O}_3$  and is therefore not shown here. Sn atoms are in darkgreen, O atoms in red, K atoms in blue, Rb atoms in lightgreen and Ti atoms in orange. The different crystal structure are plotted using VESTA [249].

Materials	Space group	Sn–O–Sn ( $^\circ$ )
SnO	$P4/nmm$	117.8
$c\text{-K}_2\text{Sn}_2\text{O}_3$	$I2_1\bar{3}$	167.6
$r\text{-K}_2\text{Sn}_2\text{O}_3$	$R\bar{3}m$	180
$\text{Rb}_2\text{Sn}_2\text{O}_3$	$R\bar{3}m$	180
$\text{TiSnO}_3$	$R\bar{3}$	-

**Table 4.1:** Space group and Sn–O–Sn angle for the different  $\text{Sn}^{2+}$  compounds studied in this work.

an exact solution of the BTE and is used to determine the phonon-limited hole mobility in our systems, does not directly give access to scattering rates. Therefore, it is not possible to perform this analysis with the IBTE approach. This means that we need to step back in terms of accuracy and analyze the scattering rates obtained from the SERTA. In the Boltzmann transport formalism under the SERTA, the hole mobility is given by a similar equation than the electron mobility (see Eq. 1.16). The important parameter in this equation for this analysis

Materials	$a$ (Å)		$c$ (Å)	
	PBEsol	Exp.	PBEsol	Exp.
SnO	3.88	3.80 [243, 244]	5.06	4.84 [244]
<i>c</i> -K <sub>2</sub> Sn <sub>2</sub> O <sub>3</sub>	8.32	8.41 [251]	8.32	8.41 [251]
<i>r</i> -K <sub>2</sub> Sn <sub>2</sub> O <sub>3</sub>	6.04	6.00 [251]	14.07	14.34 [251]
Rb <sub>2</sub> Sn <sub>2</sub> O <sub>3</sub>	6.13	6.09 [251]	14.86	15.10 [251]
TiSnO <sub>3</sub>	5.08	5.07 [250]	20.83	20.69 [250]

**Table 4.2:** Structural properties of the different Sn<sup>2+</sup> compounds studied in this work.

is the carrier lifetime given by Eq. 1.15. Being neither more nor less than a Fermi golden rule, it is conceivable to decompose this equation into two parts: one taking into account the number of available states and the conservation of energy, that we will refer to as the  $J$  parameter:

$$J_{nk} = \sum_{mv} \int \frac{d\mathbf{q}}{\Omega_{\text{BZ}}} \left[ (n_{\mathbf{q}v}^0 + f_{m\mathbf{k}+\mathbf{q}}^0) \delta(\varepsilon_{n\mathbf{k}} - \varepsilon_{m\mathbf{k}+\mathbf{q}} + \omega_{\mathbf{q}v}) \right. \\ \left. + (n_{\mathbf{q}v}^0 + 1 - f_{m\mathbf{k}+\mathbf{q}}^0) \delta(\varepsilon_{n\mathbf{k}} - \varepsilon_{m\mathbf{k}+\mathbf{q}} - \omega_{\mathbf{q}v}) \right]. \quad (4.1)$$

and one directly related to the e-ph coupling, the  $G^2$  parameter, so that

$$\frac{1}{\tau_{nk}^0} = G_{nk}^2 \times J_{nk}. \quad (4.2)$$

To enable this factorisation to be carried out computationally, it is only necessary to perform a conventional calculation of the scattering rates under the SERTA and another where all the matrix elements are set to 1. The latter gives us a direct access to the  $J$  parameter whereas the  $G^2$  parameter is obtained by dividing the scattering rates calculated conventionally by  $J_{nk}$ .

### 4.3 TRANSPORT

#### 4.3.1 SnO

Interestingly, the layered structure of SnO promotes interlayer transport (in the  $c$ -axis) over intralayer transport (in the  $a$ - and  $b$ -axes). This particularity of SnO is directly noticeable in its effective mass, as shown

in Table 4.3. The computed interlayer conductivity hole effective mass of 0.58 computed with PBE falls within the range of theoretical values reported in the literature (0.50-0.64  $m_0$ ) whereas the intralayer conductivity hole effective mass of 2.32 seems to be a little underestimated compared to other works (2.8-3.2  $m_0$ ) [108, 239, 246, 248]. The disparity in these values can be attributed to the differences in the methodologies employed to calculate the effective mass across the various studies. This large difference between intralayer and interlayer transport in SnO is also very marked in the hole mobility. Using Abinit and a fully-first principles method based on the iterative solution of the Boltzmann transport equation, we find a converged hole mobility of  $11 \text{ cm}^2 \text{ V}^{-1} \text{ s}^{-1}$  in the  $a$ - and  $b$ -axis (intralayer transport) and of  $41 \text{ cm}^2 \text{ V}^{-1} \text{ s}^{-1}$  for the  $c$ -axis (interlayer transport). These drift mobility results are in agreement with the field-effect drift measurement of Kim *et al.* [253] of  $25 \text{ cm}^2 \text{ V}^{-1} \text{ s}^{-1}$  obtained on thin films. Due to the lack of drift mobility reports, we will now compare these results with Hall mobility measurements. Fig. 4.3 shows our drift mobility and estimated Hall mobility results with temperature. The latter are calculated using a constant Hall factor ( $r_H$ ) of 1.77 as found in Ref. [107]. However, this remains an important approximation as the Hall factor can exhibit a complex temperature trend [85]. Our temperature-dependent results are in agreement with the those reported by Miller *et al.* [254] for undoped polycrystalline SnO as shown in Fig. 4.3. In their work, they achieved a record experimental Hall mobility of  $30 \text{ cm}^2 \text{ V}^{-1} \text{ s}^{-1}$  for a low carrier concentration (around  $1 \times 10^{16} \text{ cm}^{-3}$ ) at room temperature.

Materials	$m_h^*$ ( $m_0$ )		$\mu_h$ ( $\text{cm}^2 \text{ V}^{-1} \text{ s}^{-1}$ )	
	intralayer	interlayer	intralayer	interlayer
SnO	2.32	0.58	11.0	40.8
$c\text{-K}_2\text{Sn}_2\text{O}_3$	0.23	-	346.8	-
$r\text{-K}_2\text{Sn}_2\text{O}_3$	0.19	0.43	316.5	181.7
$\text{Rb}_2\text{Sn}_2\text{O}_3$	0.20	0.32	281.4	182.6
$\text{TiSnO}_3$	0.41	0.66	171.7	98.6

**Table 4.3:** Hole effective masses and IBTE mobilities (eigenvalues) of the different  $\text{Sn}^{2+}$  computed with GGA PBE (SnO) and GGA PBEsol (all the other  $\text{Sn}^{2+}$ ). The convergence studies can be found in App. B.2.

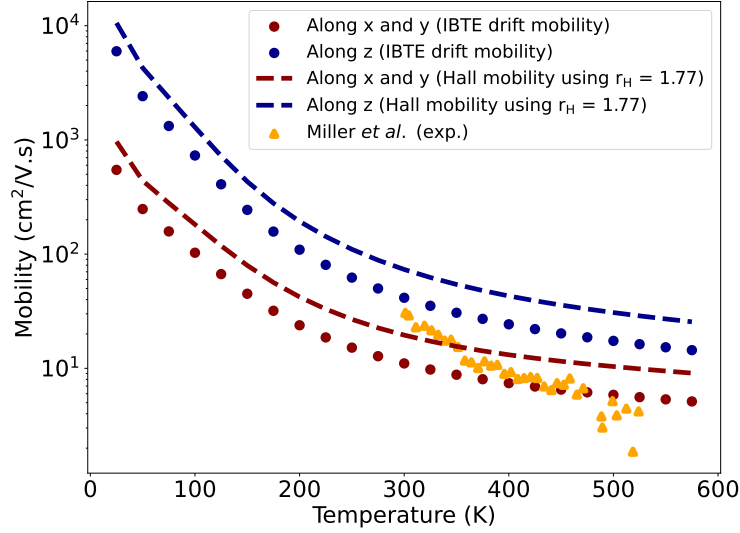


**Figure 4.3:** IBTE hole drift mobility of SnO against temperature. Using a constant Hall factor of 1.77 [107] for the range of temperature, the approximate Hall mobility is also shown and compared with experimental results from Ref. [254].

On the other hand, thin films results range from 1 to  $21 \text{ cm}^2 \text{ V}^{-1} \text{ s}^{-1}$  using different deposition methods [234, 255–261]. The high volatility of Sn during the growth of thin films leads to the formation of Sn vacancies, resulting in an increased carrier concentration and unintentional doping of the SnO thin films [257]. This can explain the slightly lower experimental results observed for thin films compared to polycrystalline samples. However, through precise modulation of the kinetic and thermodynamic conditions during the film growth process, it becomes possible to effectively minimise ionised-impurity and grain boundary scattering. This optimisation strategy contributes to the achievement of the highest thin film mobility value reported of  $21 \text{ cm}^2 \text{ V}^{-1} \text{ s}^{-1}$  obtained by Minohara *et al.* [257] with a low carrier concentration of  $7 \times 10^{16} \text{ cm}^{-3}$ . Our mobility results are also in agreement with a previous computational work done by Hu *et al.* [107] where a mobility of 7.4 and  $60.0 \text{ cm}^2 \text{ V}^{-1} \text{ s}^{-1}$  is found using two simple theoretical models for polar optical and acoustic deformation scattering.

Fig. 4.4 demonstrates that the scattering times of SnO closely follows the behaviour of the  $G^2$  parameter (see Eq. 4.2), which is directly linked

to the strength of the e-ph coupling. Specifically, we observe a first plateau in the scattering times up to 50 meV, followed by a substantial increase and a second plateau. Given the lack of any significant changes in the electronic structure at these energies, the sudden rise in scattering times can be attributed to the activation of new important phonon-mediated scattering channels with energies around 50 meV. The function  $-v_{\text{VB}}^2 \tau_{\text{VB}} \frac{\partial f}{\partial \epsilon} \delta(\epsilon - \epsilon_{\text{VB}})$  (in grey on Fig. 4.4), which gives access to the hole mobility once integrated, shows the energy states participating in the hole transport and their relative importance. Even if the peak of this curve (at 34 meV) is reached before the sudden increase, the tail largely encompasses it, demonstrating the importance of these high-frequency modes for the hole mobility in SnO. Another way to show the importance of high-frequency phonons is to look at the temperature dependence of the mobility. As shown in Fig. 4.5, an important temperature-dependence change is observed around 100K when higher energy vibrational modes are active. This may also explain the thermally activated mobility observed by Ogo *et al.* [234] and previously (maybe wrongly) attributed to possible polaron hopping.

A comprehensive view of the phonon properties of SnO is shown in Fig. 4.6: panel (a) displays the phonon band structure, while panel (b) shows the projected density of states (PDOS) for this structure. Finally, panel (c) presents the spectral decomposition of the scattering rates at two distinct energies (34 and 64 meV) corresponding to the first and second plateau of Fig. 4.4. Notably, this decomposition highlights and confirms the crucial role played by high-energy phonon modes in the scattering rate of SnO. However, these modes, mainly associated with oxygen motion (as indicated in the PDOS), can only participate to the transport when the transition  $f_{n\mathbf{k}}$  to  $f_{m\mathbf{k}+\mathbf{q}}$  requires a high-frequency phonon  $\omega_{\mathbf{q}v}$  of  $\sim 50$  meV as shown in Fig. 4.7(a). Within the first plateau (around 34 meV for instance), the only scattering processes involving these states and these high-frequency phonons can only be out-of-state transitions by phonon emission or in-state transitions by phonon absorption. Other type of transitions are not possible as the state  $f_{m\mathbf{k}+\mathbf{q}}$  does not exist (in the band gap). In the case of SnO, the out-of-state emissions are favoured as the states that can perform this type of transition are closer to the top of the valence band. This is also induced by the decreasing shape of the curve of the  $J$  parameter shown in Fig. 4.4. In fact, using a simple model based on a single parabolic band and a phonon following the Einstein model, we observe a decreasing behaviour of  $J$  with energy in the case of a transition

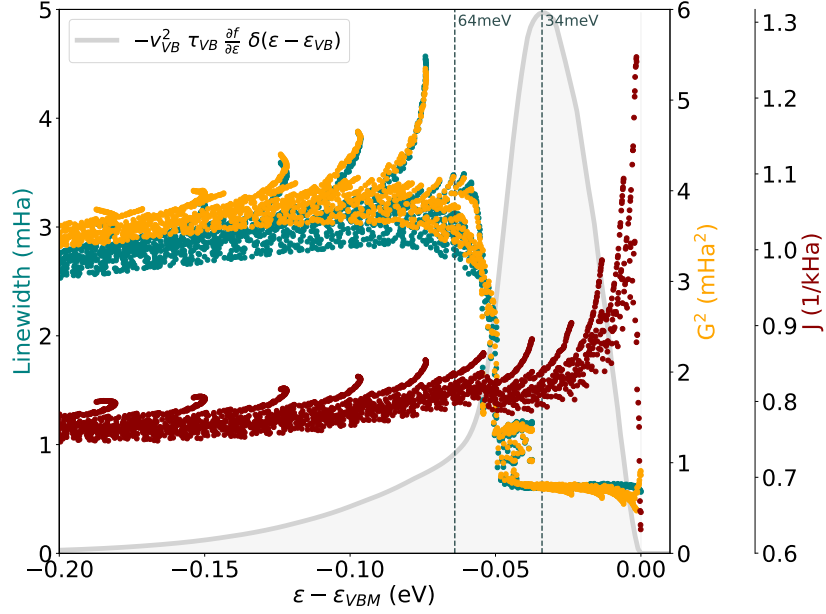


**Figure 4.4:** Hole linewidths (in teal) near the VBM of SnO. The two parameters,  $G^2$  and  $J$ , resulting from the decoupling of the scattering rates are also shown in orange and red, respectively ( $\frac{1}{\tau_{nk}} = G_{nk}^2 \times J_{nk}$ ). The grey area represents the function  $\tau_{VB} \frac{\partial f}{\partial \epsilon} \delta(\epsilon - \epsilon_{VB})$  where  $v_{VB}$  and  $\tau_{VB}$  stand for the carrier velocity and lifetime in the VB,  $\frac{\partial f}{\partial \epsilon}$  is the derivative of the Fermi-Dirac distribution function with respect to the energy and  $\delta$  the Dirac delta function. By integrating this function, the relaxation time approximation (RTA) hole mobility is obtained. In other words, only the electronic states present under this curve participate in the hole transport of SnO.

due to the emission of a phonon and an increasing behaviour when an absorption take place, as demonstrated in Fig. 4.7(b). On the other hand, an initial state close in energy to the second plateau (at 64 meV for example) allows all the different transitions with these phonons. This is also expressed by the much larger area under the curve in Fig. 4.6(c) for the latter. While the significance of these high-frequency phonon modes has been acknowledged in a previous study based on phenomenological models [107], their importance has never been described as precisely as in this first-principle work.

The other important parameter to look at during a transition between two states is the conservation of momentum. The light grey regions in the dispersion curve (Fig. 4.6(a)) correspond to the areas where intravalley scattering is relevant. This means that the only  $\mathbf{q}$  vectors

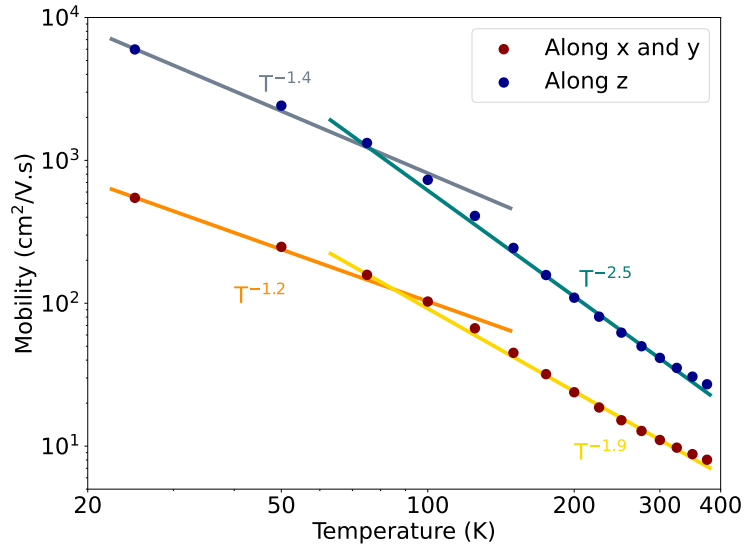


**Figure 4.5:** IBTE hole drift mobility in SnO as a function of the temperature showing the change in the temperature trend around 100K.

available for a transition that respect the conservation of the momentum are in the light grey area. For instance, this implies that acoustic modes with a large e-ph coupling at  $\mathbf{q}=\mathbf{M}$  as identified by Chen *et al.* [262] do not participate in the hole transport. Indeed, due to a rather curvy pocket at the  $\Gamma$ -point of SnO, a transition involving a momentum transfer of  $\mathbf{q}=\mathbf{M}$  is forbidden. In short, the phonon modes that scatter the most the hole in SnO are high-frequency modes with small  $\mathbf{q}$  (i.e., close to  $\Gamma$ ) that predominantly involve intralayer vibrations of oxygen. Figs. 4.8(a) and (d) illustrate these modes at two different locations at  $\Gamma$ , corresponding respectively to an optical longitudinal (LO)  $E_u$  mode ( $\Gamma_1$  in Fig. 4.6), where the oxygen atoms move in phase, and an optical degenerate  $E_g$  mode ( $\Gamma_2$  in Fig. 4.6), with oxygen atoms moving out-of-phase (the two degenerate  $E_g$  modes have the same atomic displacements pattern but in the two different intralayer directions).

A COHP analysis (Figs. 4.8(b) and (c)) with distorted structures due to these two phonons is carried out using an amplitude of 0.5 Å for the largest atomic displacement. The  $\Gamma_1$  mode does not seem to affect the structure considerably, whereas the  $\Gamma_2$  mode tends to strongly destabilise the VBM. While increased mixing between the Sn-5s-O-2p and Sn-5p orbitals could have increased the s-character of the VBM and

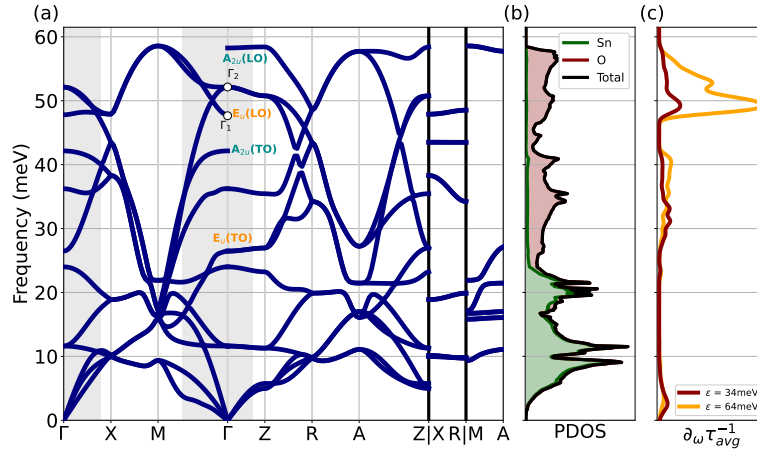


**Figure 4.6:** (a) SnO phonon dispersion computed using the PBEsol functional. The  $E_u$  (TO and LO) and  $A_{2u}$  (TO and LO) are highlighted in orange and teal, respectively. The grey areas around  $\Gamma$  show the regions relevant (due to energy conservation) for the scattering, as expressed in Eq. 1.15. (b) Phonon projected density of state (PDOS) with the contribution of Sn and O in green and red, respectively. (c) Spectral decomposition of the hole scattering rates at two different band energy level corresponding to the two plateaus of Fig. 4.4 (34 meV in red and 64 meV in orange).

caused destabilisation, in this case, the destabilisation mostly results from the interaction between the O-2p orbitals of two neighboring oxygen atoms. The two states being similar in energy, this hybridisation is favoured. However, this interaction is only possible when the oxygen atoms move out-of-phase, bringing them closer together and enabling this important hybridisation.

#### 4.3.2 Other $Sn^{2+}$

The incorporation of a third element into the binary SnO system has demonstrated notable advantages in terms of band gap enhancement and phase stability [108] but also provides substantial improvements in the hole effective mass of the material [239]. This improvement can mainly be attributed to the more favourable Sn-O-Sn configuration, which promotes better overlap between tin and oxygen atoms. Table 4.3 shows that the ternary oxides exhibit notably superior hole effective masses compared to SnO, particularly in the intralayer directions (for

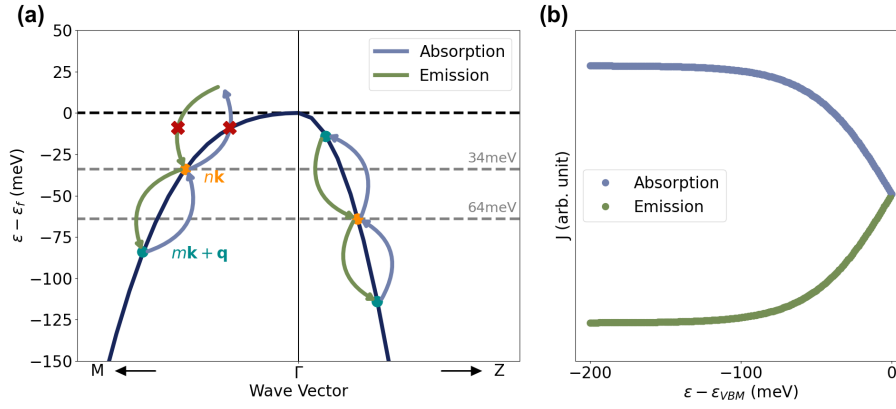


**Figure 4.7:** (a) Schematic view of the different transitions possible from an initial state  $nk$  (in orange) of 34 and 64 meV to a final state  $mk + q$  (in cyan) due to a phonon of 50 meV in SnO. The absorption and emission phenomena are in blue and green, respectively. The conservation of momentum is not taken into account in this schematic view. (b) Model of the behaviour of the parameter  $J$  as a function of the energy due to the absorption and emission of a phonon of a specific energy (following the Einstein model) in a single parabolic band  $p$ -type crystal.

layered compounds) where the effective masses decrease by an order of magnitude. In fact, looking at the effective masses in the interlayer direction, only a slight decrease is observed for  $r$ - $K_2Sn_2O_3$  and  $Rb_2Sn_2O_3$  compared to SnO whereas  $TiSnO_3$  possesses a rather similar hole band mass, albeit slightly higher. This similarity arises from their comparable crystal structures, where tin atoms in both materials are directly positioned facing each other.

Overall, the hole mobilities obtained using the IBTE methodology within Abinit mainly follow the trend of the effective masses except for  $TiSnO_3$ . Indeed, with a larger effective mass than SnO in the interlayer direction, one might expect a lower mobility in this direction compared with the value obtained for SnO. For instance, this is the result obtained using simple phenomenological models [108, 240]. However, these simple approaches, based on the Fröhlich [103] or Vogl models [106] do not fully take into account the anisotropy and particularly in this case the effective masses in the other directions. In the Boltzmann transport formalism and the relaxation-time approximation (RTA), the curvature of the bands plays a crucial role not only in determining velocities in Eq. 1.16 but also indirectly influences the number of states participating to transport. A higher effective mass corresponds to

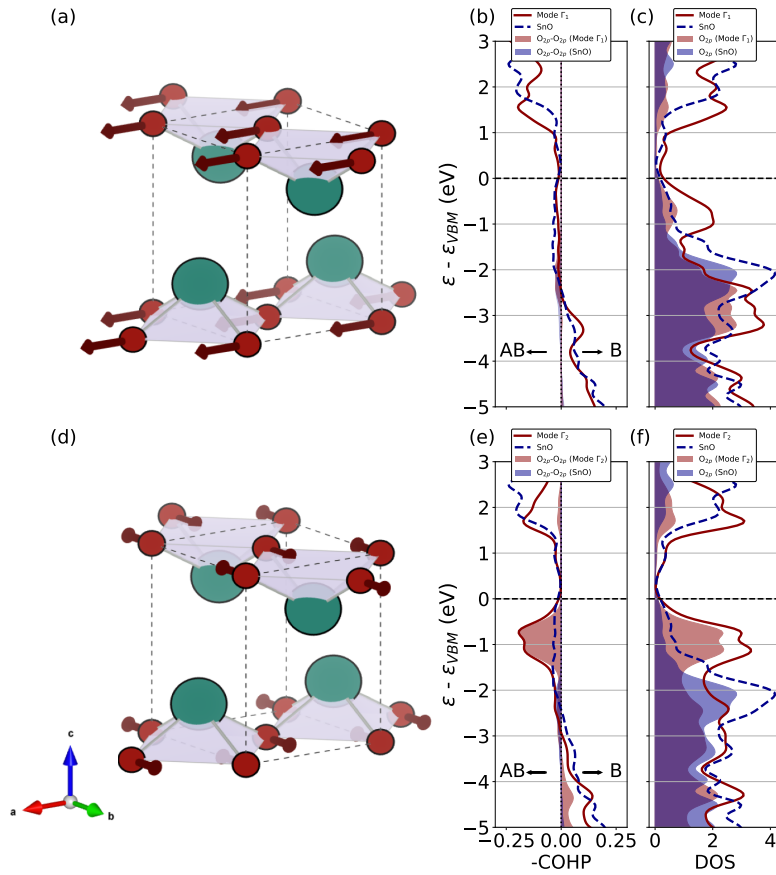


**Figure 4.8:** (a) and (d) Atomic displacements corresponding to the LO  $E_u$  mode ( $\Gamma_1$  in Fig. 4.6) and the degenerate  $E_g$  modes ( $\Gamma_2$  in Fig. 4.6), respectively. The two degenerate  $E_g$  modes showing the same atomic displacements but in the two different intralayer directions. (b) and (e) present the projected Crystal Orbital Hamiltonian Populations (COHP) for the two corresponding vibrational modes (in red) as well as the pristine SnO. The interaction between  $O_{2p}$  and  $O_{2p}$  is highlighted. Here, the -COHP is plotted in order to have the bonding levels to go to the right and the anti-bonding levels to the left. (c) and (f) show the DOS corresponding to the two modes and pristine SnO with a focus on the  $O_{2p}$  contribution.

a flatter band structure, which in turn provides a larger number of available states and scattering channels for the carriers. This can be seen as the parameter  $J$ , obtained when decoupling the Eq. 1.15 and shown in Fig. 4.9(c). The importance of this  $J$  parameter is largely underestimated in the models. Consequently, materials exhibiting excellent effective mass in one direction but poor effective masses in the other two directions, such as SnO, might exhibit lower mobility in that favourable direction compared to materials, such as  $\text{TiSnO}_3$  with higher effective mass in the same direction but excellent low effective masses in the other two directions.

Generally speaking, the parameter  $J$  is directly related to the DOS (or Seebeck) effective mass which takes into account both the effective mass and the valley degeneracy [66]. In fact,  $J$  is very low for  $r\text{-K}_2\text{Sn}_2\text{O}_3$  and  $\text{Rb}_2\text{Sn}_2\text{O}_3$  due to their low effective mass, whereas it is slightly higher for  $\text{TiSnO}_3$  owing to the same reason. Among the ternary oxides,  $c\text{-K}_2\text{Sn}_2\text{O}_3$  exhibits the highest value for  $J$ , primarily due to the presence of multiple pockets resulting from its VBM at the high symmetry point H as seen from the Fermi surface in Fig. 4.10. This larger number of valleys, in contrast to the classic single valley at  $\Gamma$  observed in the other studied materials, leads to an increased number of available states and facilitates new intervalley transitions. The shape of the curves of the various ternary oxides is also very different from SnO. This is probably linked to the larger number of transitions made by absorption of a phonon and not emission as shown in Fig. 4.7(b), which is the opposite of what happens in SnO.

However, this high number of possible transitions is counterbalanced by the low strength of e-ph coupling ( $G^2$ ) in  $c\text{-K}_2\text{Sn}_2\text{O}_3$  leading to very low scattering rates close to the VBM, as shown in Fig. 4.9(a) and (b). In comparison with SnO, the ternary oxides do not present such an abrupt increase of this  $G^2$  parameter close to the VBM. An important rise is observed for  $\text{TiSnO}_3$ , similarly to SnO, but it only occurs after 90 meV where the electronic states do no longer participate greatly to transport. By analyzing the linewidths, it can be seen that the lowest values are observed for  $\text{TiSnO}_3$  and  $c\text{-K}_2\text{Sn}_2\text{O}_3$ , while the highest values are found for  $r\text{-K}_2\text{Sn}_2\text{O}_3$  and  $\text{Rb}_2\text{Sn}_2\text{O}_3$  within the energy range relevant for transport. This pattern aligns with the trend observed in the  $G^2$  parameter related to the e-ph coupling. However, it is noteworthy that these linewidths remain considerably lower than those exhibited by SnO after the important increase. This implies that in SnO the high scattering rates are due to both an important e-ph coupling and an

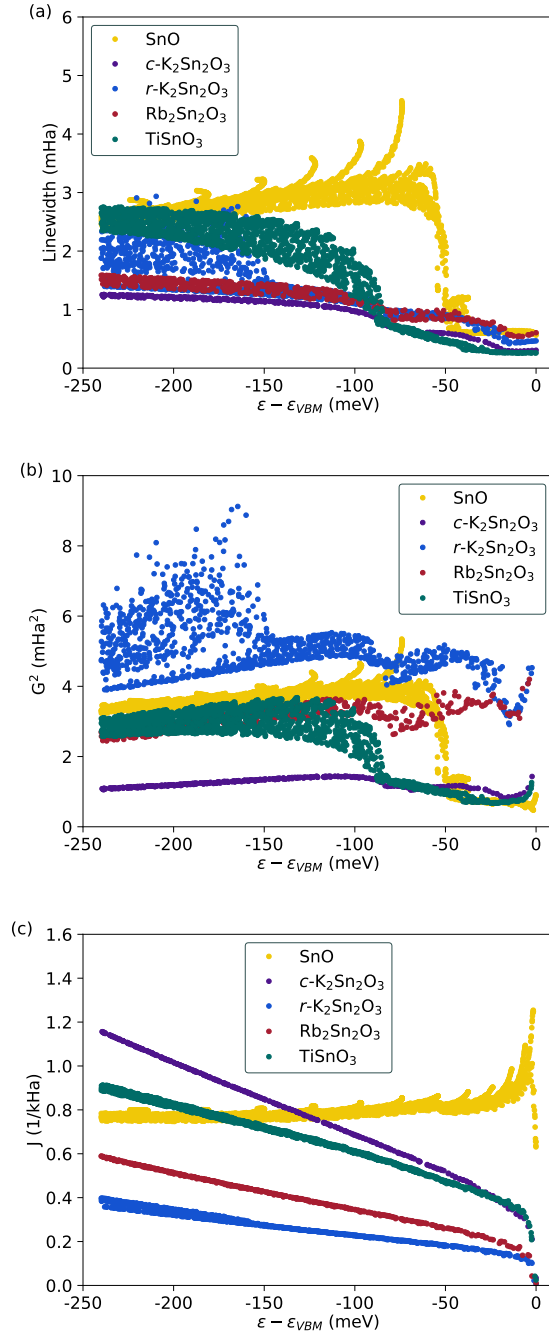


**Figure 4.9:** (a) Hole linewidths, (b)  $G^2$  parameters and (c)  $J$  parameters with SnO in yellow,  $c\text{-K}_2\text{Sn}_2\text{O}_3$  in purple,  $r\text{-K}_2\text{Sn}_2\text{O}_3$  in blue,  $\text{Rb}_2\text{Sn}_2\text{O}_3$  in red and  $\text{TiSnO}_3$  in green.

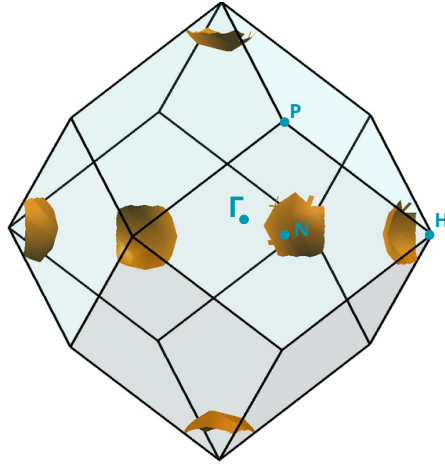


**Figure 4.10:** Fermi surface of  $c\text{-K}_2\text{Sn}_2\text{O}_3$  at an energy close to the VBM showing the different pockets that allow intervalley transitions.

important number of states allowing the different transitions to happen. In other words, the tendency for a large  $J$  parameter to be linked to a small  $G^2$  parameter as observed in the different ternary oxides, does not apply in the case of SnO.

To analyze the phonon modes that exhibit the strongest coupling with electrons and compare them with SnO, the spectral decomposition of the scattering rates is also performed for the four ternary oxides at 300K. The analysis is performed at an energy value specifically chosen to correspond to the energy for which the maximum number of states participate in transport, as shown in Fig. 4.11. The results are shown in Figs. 4.12, 4.13, 4.14 and 4.15 for  $c\text{-K}_2\text{Sn}_2\text{O}_3$ ,  $r\text{-K}_2\text{Sn}_2\text{O}_3$ ,  $\text{Rb}_2\text{Sn}_2\text{O}_3$  and  $\text{TiSnO}_3$ , respectively.

The most noticeable observation is that the modes with the strongest hole coupling are consistently associated with a significant displacement of the third atom, namely Rb, K, or Ti, in addition to oxygen, as depicted in panel (b) of these figures. Another interesting finding is that the tin displacement in these modes is consistently small, which is also in line with the results observed in SnO. In the rhombohedral materials, the large displacement of the third atom can be either in the direction perpendicular to the layers or in the layers and exhibits a similar pattern across all three compounds. These vibrational modes exhibit an LO-TO splitting and belong to either  $E_u$  or  $A_{2u}$  symmetry. However,  $\text{TiSnO}_3$  also possesses rather important high-frequency phonon modes,

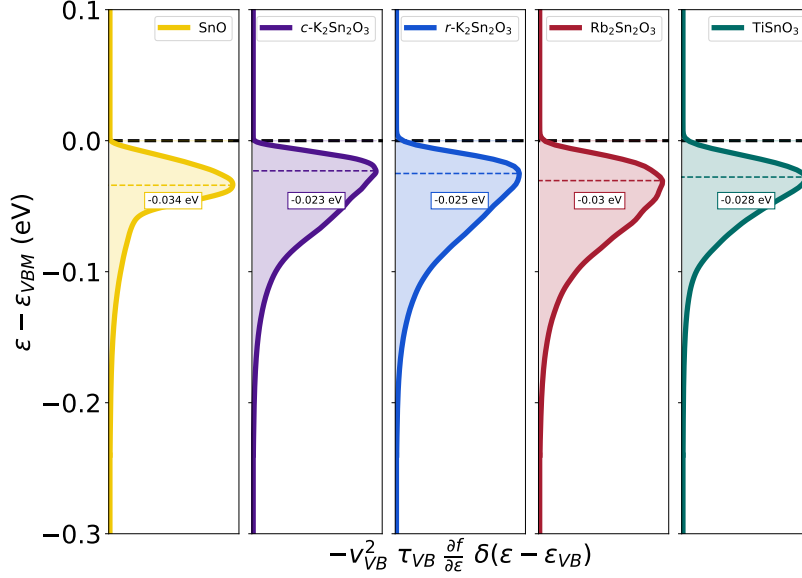


**Figure 4.11:** The function  $-v_{VB}^2 \tau_{VB} \frac{\partial f}{\partial \epsilon}$ , convoluted with  $\delta(\epsilon - \epsilon_{VB})$  in the valence band at 300K for the different materials studied in this work. In this expression,  $v_{VB}$  and  $\tau_{VB}$  stand for the carrier velocity and lifetime in the valence band (VB),  $\frac{\partial f}{\partial \epsilon}$  is the derivative of the Fermi-Dirac distribution function with respect to the energy and  $\delta$  the Dirac delta function. By integrating this function, the relaxation time approximation (RTA) hole mobility is obtained. The energy corresponding to the maximum of this curve is used for the phonon analysis. The corresponding band structures can be seen in the App. B.1.2.

in contrast with  $r\text{-K}_2\text{Sn}_2\text{O}_3$  and  $\text{Rb}_2\text{Sn}_2\text{O}_3$  but in a similar way to SnO. Being very high in frequency, they do not allow a large number of transitions, which limits their impact at room temperature. Nevertheless, we can expect them to play a crucial role as the temperatures rises. Finally, in the case of  $c\text{-K}_2\text{Sn}_2\text{O}_3$ , the  $T^{(3)}$  (LO) mode just below 18 meV, associated with perpendicular displacement of the two distinct K atoms, is responsible for just under half of the scattering of the holes. In comparison to SnO, the high-frequency modes associated with oxygen motions do not play the main role in the ternary oxides at room temperature. This can be attributed to their *too* high frequencies, which are already barely accessible in SnO at 300K, leading to a restricted number of electronic transitions.

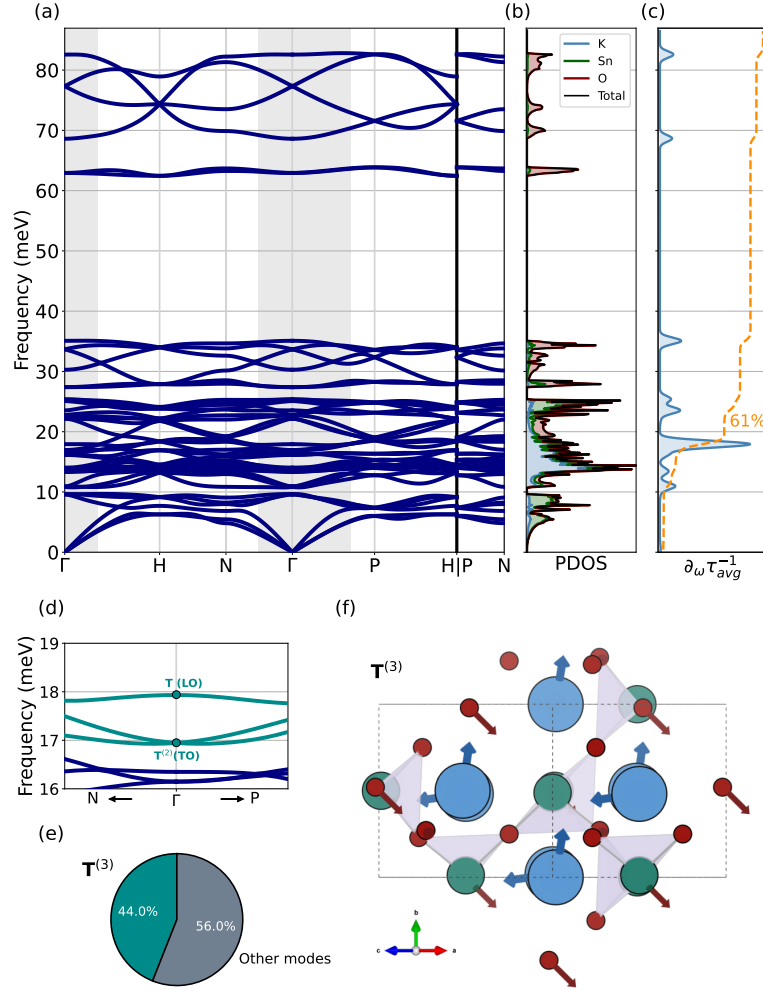


**Figure 4.12:** (a)  $c$ - $\text{K}_2\text{Sn}_2\text{O}_3$  phonon dispersion computed using the PBEsol functional. The grey areas around  $\Gamma$  show the regions relevant (due to energy conservation) for the scattering, as expressed in Eq. 1.15. (b) PDOS with the contribution of K, Sn and O atoms in blue, green and red, respectively. (c) Spectral decomposition of the hole scattering rates at 300K. The scattering rates are computed at an energy of 23 meV from the VBM, corresponding to the energy for which the maximum number of states participate in hole transport. (d) Phonon dispersion at  $\Gamma$  illustrating the most important modes for hole scattering with (e) their relative importance and (f) the corresponding atomic displacements. K, Sn and O atoms are in blue, darkgreen and red, respectively.

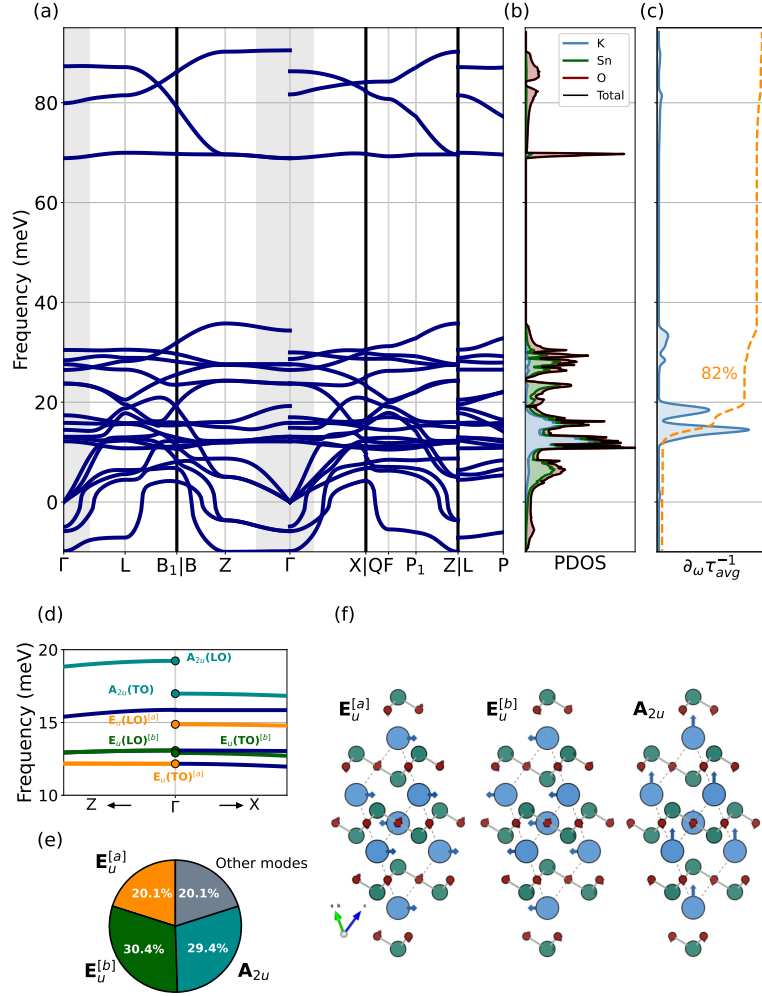


**Figure 4.13:** (a)  $r$ - $\text{K}_2\text{Sn}_2\text{O}_3$  phonon dispersion computed using the PBEsol functional. The grey areas around  $\Gamma$  show the regions relevant (due to energy conservation) for the scattering, as expressed in Eq. 1.15. (b) PDOS with the contribution of K, Sn and O atoms in blue, green and red, respectively. (c) Spectral decomposition of the hole scattering rates at 300K. The scattering rates are computed at an energy of 25 meV from the VBM, corresponding to the energy for which the maximum number of states participate in hole transport. (d) Phonon dispersion at  $\Gamma$  illustrating the most important modes for hole scattering with (e) their relative importance and (f) the corresponding atomic displacements. K, Sn and O atoms are in blue, darkgreen and red, respectively.

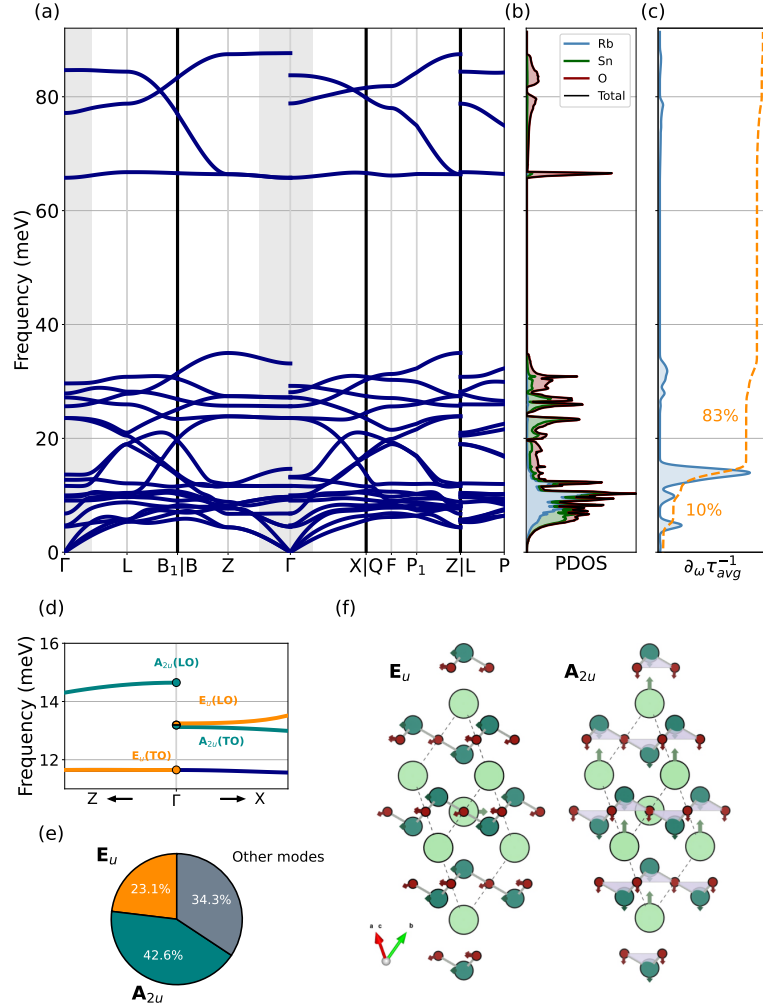


**Figure 4.14:** (a)  $\text{Rb}_2\text{Sn}_2\text{O}_3$  phonon dispersion computed using the PBEsol functional. The grey areas around  $\Gamma$  show the regions relevant (due to energy conservation) for the scattering, as expressed in Eq. 1.15. (b) PDOS with the contribution of Rb, Sn and O atoms in blue, green and red, respectively. (c) Spectral decomposition of the hole scattering rates at 300K. The scattering rates are computed at an energy of 30 meV from the VBM, corresponding to the energy for which the maximum number of states participate in hole transport. (d) Phonon dispersion at  $\Gamma$  illustrating the most important modes for hole scattering with (e) their relative importance and (f) the corresponding atomic displacements. Rb, Sn and O atoms are in lightgreen, darkgreen and red, respectively.

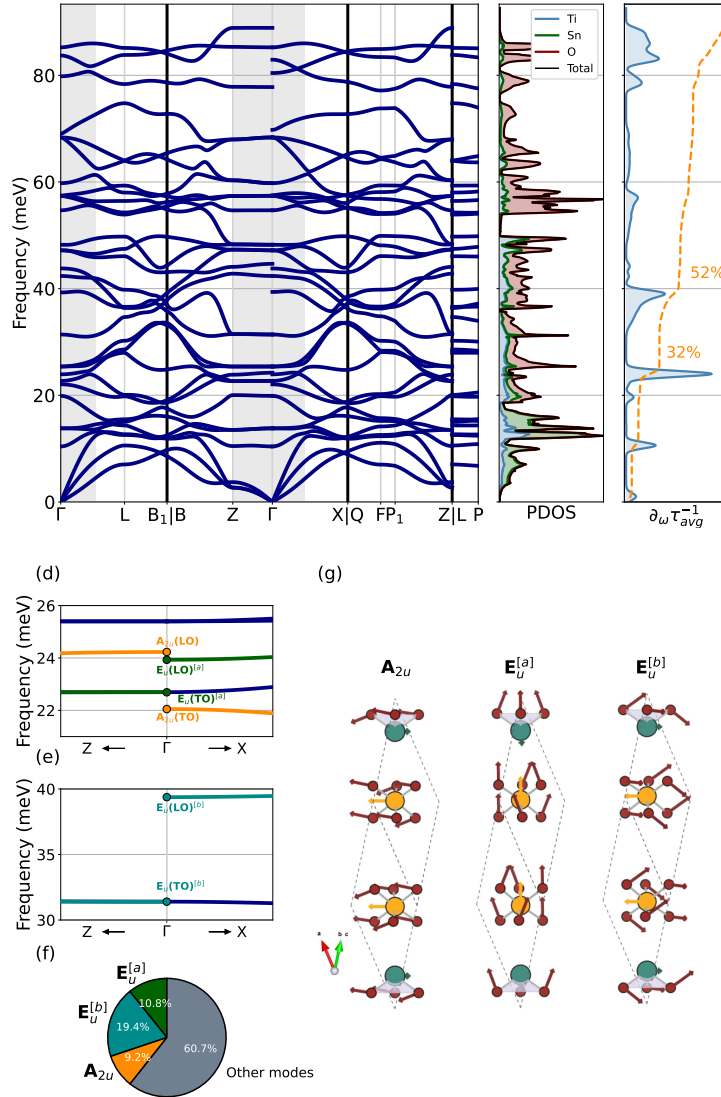


**Figure 4.15:** (a)  $\text{TiSnO}_3$  phonon dispersion computed using the PBEsol functional. The grey areas around  $\Gamma$  show the regions relevant (due to energy conservation) for the scattering, as expressed in Eq. 1.15. (b) PDOS with the contribution of Ti, Sn and O atoms in blue, green and red, respectively. (c) Spectral decomposition of the hole scattering rates at 300K. The scattering rates are computed at an energy of 28 meV from the VBM, corresponding to the energy for which the maximum number of states participate in hole transport. (d) and (d) Phonon dispersions at  $\Gamma$  illustrating the most important modes for hole scattering with (f) their relative importance and (g) the corresponding atomic displacements. Ti, Sn and O atoms are in orange, darkgreen and red, respectively.

#### 4.4 CONCLUSION

This first-principle study showcases the remarkable potential of ternary  $\text{Sn}^{2+}$  for achieving high hole mobility, positioning them as top contenders among the finest  $p$ -type materials in the market. While the stability of these oxides has been a subject of discussion, it is noteworthy that most of them have been successfully synthesized in previous research. The intriguing transport results obtained from these oxides present an opportunity to rekindle experimental studies on them. Although the primary focus of this work has centered on potential applications in TCOs, it has been demonstrated that materials with lone pairs can hold promise for diverse applications, including thermoelectrics [22, 254]. However, a comprehensive exploration of the thermoelectric capabilities of these materials remains a topic for future investigation.

Beyond calculating the hole mobility of these oxides, our study involves different analyses aimed at gaining a deeper insight into the transport mechanisms within these compounds. In fact, through a comprehensive examination of transport properties in both SnO and these ternary oxides, we highlighted the role of the effective mass on the lifetime of our compounds, employing an innovative approach for factorising the scattering rates. While this is not often taken into account in the simplest models, it can have a significant effect on mobility. One such example is SnO, which exhibits two very poor transport directions primarily attributed to a high effective mass in these directions. Consequently, the direction in which SnO demonstrates a more favourable effective mass is directly impacted, influenced by the large number of scattering channels provided by a flat band. We also show that only a small part of the phonons are involved in the scattering of the electrons, even when the material has numerous phonon bands. In other words, this means that carriers are only scattered by certain very specific types of vibrations. This could lead to new investigations that try to reduce these specific vibrations in order to boost the transport properties of these materials.

## CONCLUSION

---

Understanding electronic transport in materials is of paramount importance in both fundamental and applied physics, as it directly influences critical properties like the mobility of semiconductors and the efficiency of thermoelectric materials. Carrier transport hinges on a material's electronic structure and various scattering events. Among these, scattering by phonons and other carrier stand out the most fundamental mechanisms, even occurring in pristine single crystals. In the past decade, there has been a significant breakthrough in the development of accurate theoretical methods and computational codes. These advancements allow for the precise calculation of electronic transport parameters, such as conductivity, mobility, and the Seebeck coefficient, entirely from first principles, without relying on experimental parameters.

In the Chap. 1, we described one of these methodologies called the BTE with a focus on the phonon-limited mobility. For years, most computations have relied on some forms of simplification of the BTE. We demonstrated in this work that these approximations may deviate significantly from the exact values. In addition, thanks to the latest improvements in `Abinit` and the development of a new workflows, the different steps required to achieve converged carrier mobilities are now almost fully automated. This enables us to conduct one of the first high-throughput study in the field based on the iterative solution of the BTE, paving the way for other screening works. However, it is also important to emphasise that the methodology presented here has limitations not only in terms of the method itself but also stemming from the inherent complexity of the calculations involved. Regarding the BTE, one should be particularly cautious when working within specific temperature regimes, especially in cases of extremely low or high temperatures, or, for instance, when the e-ph coupling is extremely pronounced, leading to the formation of polarons. Such specific conditions necessitate the application of dedicated methods and approaches to ensure accurate and reliable results. On the other hand, performing very large-scale calculations involving hundreds of materials, or achieving converged results on larger systems, still appears to be beyond the scope of approaches with this level of accuracy. Therefore, it remains crucial to acknowledge the existence of other methods, model-based or more

approximate for instance, that facilitate these calculations that are still unattainable using our first-principles procedure.

In fact, in order to effectively address future developments in the field, it is also imperative to incorporate discussions on machine learning (ML). Currently, the application of ML in the realm of electronic transport can be categorised into two distinct areas. First, microscopic quantity computation where deep-learning framework that represent DFT Hamiltonian [263] are used to calculate intricate quantities, such as e-ph matrix elements, as demonstrated in Ref. [264]. Secondly, database-driven predictive models that involves harnessing ML's capabilities on extensive databases to train models. These models could be subsequently employed to predict mobility or other related e-ph coupling properties for a multitude of materials. This approach has already shown promise, notably in recent research where it was applied to forecast band-gap zero-point renormalisation, as highlighted in Ref. [265]. Alternatively, ML can also be used to calculate different material properties which are then implemented in e-ph models as explained in Sec. 1.2.5 [111]. As an automated framework like ours offers new insights and could complement model-based methods, it could also be used in ML studies based on active learning for instance.

In the subsequent sections of this work, the focus has been directed towards specific systems with the aim of investigating their properties for various applications. In Chap. 2, we computed the thermoelectric properties of the Zintl material  $\text{Ca}_5\text{In}_2\text{Sb}_6$ . Our theoretical findings, in conjunction with experimental measurements, reveal a distinctive quasi-1D electronic transport in this material, while thermal transport demonstrates an isotropic behaviour. Such a decoupling between electronic and thermal transport holds significant promise in the field of thermoelectrics, as it could allow the achievement of very high FoM  $zT$ . In Chap. 3, we explored the transport properties of the well-known TCM CuI using both our methodology based on the IBTE and the AMSET approach. This combined method has enabled us to establish an upper limit to the hole mobility as a function of the carrier concentration in CuI. This theoretical upper bound suggests that there is still room for improvement and optimisation of the synthesis conditions, while bearing in mind that surface and grain boundary scattering may play significant roles. Finally, we delve into another intriguing family of *p*-type materials for transparent conductive applications — the Sn(II) family. While SnO is already a well-known TCO, the study of ternary tin (II) oxides remains relatively limited. In Chap. 3, we undertake

a comprehensive study of the mobility of SnO and four other ternary oxides, namely  $K_2Sn_2O_3$  (in the cubic and rhombohedral phases),  $Rb_2Sn_2O_3$  and  $TiSnO_3$ . In addition to showcasing the potential for these oxides to achieve remarkably high hole mobilities, we establish that only a limited number of phonon modes are responsible for carrier scattering. This finding could pave the way for new investigations into the crystal structure of these oxides, with the goal of minimising the scattering due to these important vibrational modes. Additionally, our study enhances our comprehension of the pivotal role that effective mass plays in determining electronic lifetimes through an innovative approach that factorise the scattering rates.





## COMPUTATIONAL DETAILS

---

### A.1 DETAILS ABOUT THE TRANSPORT IMPLEMENTATION IN ABINIT

Different optimisations are used throughout the code to make it computationally competitive with Wannier-based implementations.

- The  $\mathbf{k}$ -points are automatically filtered so that only the states within a small energy window ( $\sim 10 \times 3/2k_B T$ , with  $k_B$  the Boltzmann constant and  $T$  the temperature) around the band edges are considered, since they are the only relevant ones.
- The  $\mathbf{q}$ -points are also filtered, based on the energy conservation in Eq. (1.15), to keep only those for which a phonon can indeed lead to a transition. This greatly reduces the total number of e-ph matrix elements to compute.
- A linear tetrahedron integration method is used to integrate Eq. (1.15), in order to avoid the popular use of a Gaussian broadening to approximate the Dirac  $\delta$  distributions, hence avoiding an additional convergence study.

The solution of the MRTA and IBTE have now also been implemented in Abinit. The MRTA is straightforward since the velocities are already known. In the case of the IBTE, the iterative solution requires to set a threshold for the convergence. This parameter can be automatically determined by Abinit based on a heuristic or manually set. Other parameters allow a fine tuning of the convergence, such as a mixing of the solutions at two consecutive iteration steps or a maximum number of iterations.

### A.2 ADDITIONAL DETAILS ABOUT THE WORKFLOW

The ingredients needed to obtain the mobilities are the KS wave functions on the dense mesh for the electronic part (in purple in Fig. A.1) and the DFPT scattering potentials and the interatomic force constants on a coarse mesh (typical of DFPT) for the phonon part (in blue in

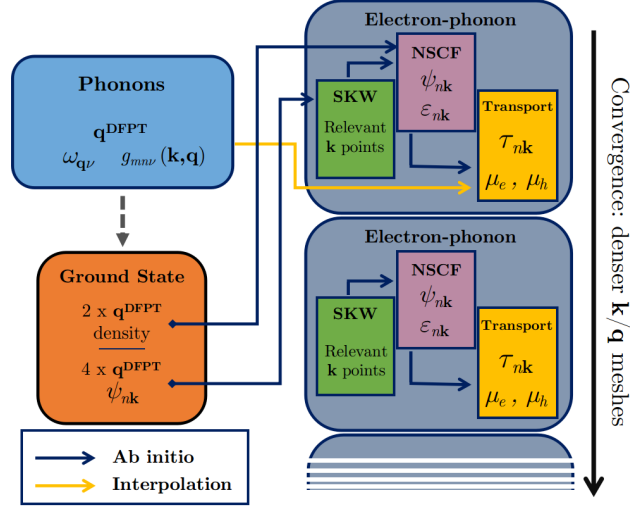


**Figure A.1:** Flowchart illustrating the workflow used to automatically compute phonon-limited mobilities.

Fig. A.1). The latter can be easily computed with another AbiPy workflow, although in this study we prefer to start from a database of previous DFPT computations [94, 95]. The ground-state is first determined on a  $\mathbf{k}$  mesh twice as dense as  $\mathbf{q}^{\text{DFPT}}$  in each direction (in orange in Fig. A.1). The ground-state density is then used to determine the wave function on the dense meshes with a non-self-consistent run. The computation of the dense wave function is a two-step procedure (in green and purple in Fig. A.1). First, a Shankland-Koelling-Wood (SKW) interpolation [58, 266–268] is performed starting from an initial electronic band structure, in order to determine which  $\mathbf{k}$  points have electronic states  $n\mathbf{k}$  within the energy window relevant for transport [48]. For the SKW interpolation to work properly, a denser  $\mathbf{k}$  mesh is needed for the initial wave function. For this reason, another ground-state run is initially performed on a  $\mathbf{k}$  mesh four times as dense as  $\mathbf{q}^{\text{DFPT}}$  in each direction (in orange in Fig. A.1). Once the interpolation is done, the list of relevant  $\mathbf{k}$  points is then used in the non-self-consistent run to greatly reduce the cost of the computation and the size of the created wave function file. All the ingredients required to compute mobilities are then readily available. A convergence study is needed on this dense mesh. For this reason, we perform the previous steps multiple times for meshes of increasing density. Convergence is assumed to be reached when three consecutive grids lead to mobilities maximum 5% away

from each others. In our initial tests, we found that the IBTE mobility requires denser meshes than the SERTA or MRTA. As a consequence all the convergence studies are done for the IBTE results: we start with an initial guess for the dense mesh that is 14 times  $\mathbf{q}^{\text{DFPT}}$  in each directions, (corresponding roughly to  $4 \times 10^6$  points per reciprocal atom) then we densify the sampling by steps of  $2 \times \mathbf{q}^{\text{DFPT}}$  until convergence is reached.

### A.3 QUASI-1D ELECTRONIC TRANSPORT AND ISOTROPIC PHONON TRANSPORT IN THE ZINTL $\text{Ca}_5\text{In}_2\text{Sb}_6$

The electronic structure of  $\text{Ca}_5\text{In}_2\text{Sb}_6$  was computed using density functional theory (DFT) and the Vienna *ab initio* Simulation Package (VASP) [204–206] using the Perdew-Burke-Ernzerhof (PBE) generalised gradient approximation (GGA) [269], the projector augmented-wave (PAW) approach and a  $\mathbf{k}$ -point grid of  $10 \times 4 \times 2$ . The conductivity effective masses and transport properties (obtained from PBE without SOC) were obtained with the BoltzTrap software [58, 59] by solving the Boltzmann transport equation, and the Pymatgen software was used for the post-processing analysis [270]. The calculated phonon dispersion of  $\text{Ca}_5\text{In}_2\text{Sb}_6$  was obtained using density functional perturbation theory (DFPT) within the Abinit software [81, 271]. A  $\mathbf{q}$ -grid of  $6 \times 2 \times 2$  was used to obtain the accurate phonon band structure. The mode Grüneisen parameters were obtained by performing calculations with a cell volume 1% larger than the initial phonon calculation and another with a volume 1% smaller.

### A.4 LIMITS TO HOLE MOBILITY IN COPPER IODIDE

Electronic band structure, AMSET inputs and defect calculations were performed within VASP, a periodic plane-wave code that uses the projector-augmented wave (PAW) method for describing the interaction between core and valence electrons [51, 203–208]. The explicit electron configurations of the pseudopotentials used were: Cu  $3d^{10}4s^1$ ; I  $5s^25p^5$ ; S  $3s^23p^4$ ; Se  $4s^24p^4$ . A plane-wave cut-off of 500 eV and a  $\Gamma$ -centered  $\mathbf{k}$ -point mesh of  $7 \times 7 \times 7$  were found to converge the total energy to within  $1 \text{ meV atom}^{-1}$ . Structural relaxations were carried out with a plane-wave cut-off of 650 eV to avoid Pulay stress and with a convergence criteria of  $0.1 \text{ meV atom}^{-1}$ . The GGA PBEsol functional was used for all convergence testing and density functional perturbation

theory (DFPT) related inputs [272] while the hybrid PBE0 functional was used for electronic structure, defect and finite differences (FD) calculations [269]. For all electronic structure calculations, a spin-orbit coupling (SOC) effects were explicitly considered, due to the presence of heavy I atoms. Considering the size of the spin-orbit split-off in the electronic band structure, the addition of SOC effects via a single-shot electronic structure calculation after structural optimisation is crucial to get the correct value of the band gap and relative band edge positions during defect calculations. SOC effects are negligible when computing structural properties, so were not included during relaxations.

Charge transport properties were calculated using both Abinit and the AMSET package. Abinit uses a fully first-principles approach to calculate phonon-limited mobilities based on an iterative solver to the Boltzmann transport equation (IBTE) [48, 52, 80, 81]. The approach used in Abinit, which is detailed in Refs. [48] and [42] and summarised in App. A.1. Here, a convergence is assumed to be reached when three consecutive grids lead to mobilities maximum 5% away from each others. In CuI, the converged IBTE mobilities were obtained with  $\mathbf{k}$ -meshes of  $162 \times 162 \times 162$  and interpolated DFPT scattering potentials and interatomic force constants obtained on a  $9 \times 9 \times 9$  coarse  $\mathbf{q}$ -mesh. All the calculations needed to obtain the mobility within Abinit were done with GGA PBEsol functional including SOC. The dynamical quadrupoles ( $Q^*$ ) were also included for the scattering potentials and mobilities. However, as the DFPT computation of  $Q^*$  is still limited to norm-conserving pseudopotentials without non-linear core corrections (NLCC) and without SOC, a slight deviation of the mobility can be expected but by several orders of magnitude less than doing the calculations without taking the  $Q^*$  into account.

On the other hand, AMSET solves the linearised Boltzmann transport equation using the relaxation time approximation (RTA). Individual scattering rates were explicitly calculated using materials properties, going beyond the constant relaxation time approximation to give a more accurate description of carrier lifetimes. In this study, scattering from polar optical phonons (POP), acoustic deformation potentials (ADP), ionised impurities (IMP) and piezoelectric effects (PIE) were considered, which require deformation potentials, the elastic constant, low- and high-frequency dielectric constants, the polar optical phonon frequency and the piezoelectric constant. A dense uniform  $\Gamma$ -centred  $\mathbf{k}$ -point mesh of  $14 \times 14 \times 14$  was used to obtain the wavefunction overlaps for determining scattering rates, and the corresponding band

structure was plotted using the SUMO package [273]. The deformation potentials were calculated from density of states calculations using the same convergence parameters as bulk calculations. The low-frequency dielectric constant, piezoelectric constant and polar optical phonon frequency were calculated using both density functional perturbation theory (DFPT) and finite differences (FD) implementations in VASP. The high-frequency dielectric constant was calculated with the PBE0 functional using the independent particle random phase approximation (IP-RPA) optics routine in VASP and converged against the number of empty bands and  $\mathbf{k}$ -point density.

Phonon calculations on CuI were performed with DFPT and Abinit using PBEsol+SOC and a  $9 \times 9 \times 9$   $\mathbf{q}$ -mesh following the methodology used by Petretto *et al.* [94]. The structures were relaxed until all the forces on the atoms and the stresses were below  $10^{-6}$ Ha/Bohr and  $10^{-4}$  Ha/Bohr<sup>3</sup>, respectively, using a plane-wave cut-off of 46 Ha.

#### A.5 POTENTIAL NEW STATE-OF-THE-ART P-TYPE MATERIALS IN TIN (II) OXIDES

All the calculations presented in this study were performed using Abinit [80, 81], employing the GGA PBEsol functional [272]. Abinit employs a fully first-principles approach to compute phonon-limited mobilities by iteratively solving the Boltzmann transport equation (IBTE) [42, 48, 52]. The methodology employed in Abinit, which is comprehensively outlined in Ref.[48] and [42] and summarized in App. A.1, allows us to achieve performance levels comparable to Wannier-based packages, eliminating the necessity of using Wannier functions altogether. In this work, convergence is assumed to be reached when the mobilities of three consecutive grids differ by no more than 5%. The converged IBTE mobilities were obtained with  $\mathbf{k}$ -meshes (for the electronic part) of  $128 \times 128 \times 96$  for SnO,  $130 \times 130 \times 130$  for  $c$ -K<sub>2</sub>Sn<sub>2</sub>O<sub>3</sub>,  $156 \times 156 \times 156$  for  $r$ -K<sub>2</sub>Sn<sub>2</sub>O<sub>3</sub>,  $144 \times 144 \times 144$  for Rb<sub>2</sub>Sn<sub>2</sub>O<sub>3</sub> and  $110 \times 110 \times 110$  for TiSnO<sub>3</sub>. On the other hand, DFPT scattering potentials and interatomic force constants also needed for the computation of the mobility were obtained by interpolation starting from a coarse  $\mathbf{q}$ -mesh of  $8 \times 8 \times 6$  for SnO,  $6 \times 6 \times 6$  for  $c$ -K<sub>2</sub>Sn<sub>2</sub>O<sub>3</sub>,  $r$ -K<sub>2</sub>Sn<sub>2</sub>O<sub>3</sub>, and Rb<sub>2</sub>Sn<sub>2</sub>O<sub>3</sub> and  $5 \times 5 \times 5$  for TiSnO<sub>3</sub>. The latter having been taken from the phonon database of Petretto *et al.* [94]. All the mobility and scattering potential calculations were performed with the inclusion of dynamical quadrupoles (Q\*). It has been shown that the integration of

$Q^*$ , the next order of correction to dynamical dipoles, in the computation of the mobility is essential to obtain accurate results [48, 52]. As the computation of  $Q^*$  is still limited to norm-conserving pseudopotentials without non-linear core corrections (NLCC), a slight deviation in mobility can be expected but it is several orders of magnitude smaller compared to performing calculations without it.

# B

## ADDITIONAL RESULTS & FIGURES

### B.1 HIGH-THROUGHPUT STUDY

#### B.1.1 Numerical results

Materials	mp- <i>id</i>	Space Group	Carrier	$\mu^{\text{IBTE}}$ ( $\text{cm}^2\text{V}^{-1}\text{s}^{-1}$ )	$\mu^{\text{CRTA}}/\tau$ ( $\times 10^{14}\text{cm}^2\text{V}^{-1}\text{s}^{-2}$ )	$\mu^{\text{SERTA}}$ ( $\text{cm}^2\text{V}^{-1}\text{s}^{-1}$ )	$\mu^{\text{MRTA}}$ ( $\text{cm}^2\text{V}^{-1}\text{s}^{-1}$ )
BaTe	mp-1000	Fm $\bar{3}m$	e	71.420	49.021	32.493	70.271
MgSe	mp-10760	Fm $\bar{3}m$	e	179.247	59.762	97.086	236.538
SrS	mp-1087	Fm $\bar{3}m$	e	66.191	43.000	37.933	82.481
CaSe	mp-1415	Fm $\bar{3}m$	e	90.817	45.840	49.482	105.771
BaS	mp-1500	Fm $\bar{3}m$	e	50.158	41.675	27.499	59.257
CaTe	mp-1519	Fm $\bar{3}m$	e	113.422	50.339	60.282	124.453
CaS	mp-1672	Fm $\bar{3}m$	e	93.495	42.981	58.797	128.928
PbSe	mp-2201	Fm $\bar{3}m$	e	970.852	136.126	366.402	912.222
			h	1224.676	146.361	461.043	1072.858
NaBr	mp-22916	Fm $\bar{3}m$	e	54.991	55.383	25.391	61.384
AgBr	mp-23231	Fm $\bar{3}m$	e	262.882	93.315	98.495	247.840
NaI	mp-23268	Fm $\bar{3}m$	e	82.157	65.583	34.871	85.097
RbI	mp-23302	Fm $\bar{3}m$	e	59.135	62.550	20.813	57.496
LiH	mp-23703	Fm $\bar{3}m$	e	629.026	63.530	625.860	668.881
			h	257.207	43.314	256.306	270.913
NaH	mp-23870	Fm $\bar{3}m$	e	224.236	37.416	208.533	281.247
SrO	mp-2472	Fm $\bar{3}m$	e	59.876	34.425	41.300	99.127
K <sub>3</sub> IO	mp-28171	Pm $\bar{3}m$	e	55.023	52.732	25.680	57.652
CsCdCl <sub>3</sub>	mp-568544	Pm $\bar{3}m$	e	71.372	70.726	29.121	70.834
TlBr	mp-568560	Fm $\bar{3}m$	e	62.842	56.848	24.153	60.869
			h	39.847	44.985	16.467	39.243
CsI	mp-614603	Fm $\bar{3}m$	e	43.815	50.434	14.792	42.560
CsCaH <sub>3</sub>	mp-644203	Pm $\bar{3}m$	e	238.566	38.374	159.009	345.400
CaCdO <sub>2</sub>	mp-753287	P <sub>4</sub> /mmm	e	524.143	93.033	324.964	829.307
BaSe	mp-1253	Fm $\bar{3}m$	e	51.710	44.441	24.404	52.907

Materials	mp- <i>id</i>	Space Group	Carrier	$\mu^{\text{IBTE}}$ ( $\text{cm}^2\text{V}^{-1}\text{s}^{-1}$ )	$\mu^{\text{CRTA}}/\tau$ ( $\times 10^{14}\text{cm}^2\text{V}^{-1}\text{s}^{-2}$ )	$\mu^{\text{SERTA}}$ ( $\text{cm}^2\text{V}^{-1}\text{s}^{-1}$ )	$\mu^{\text{MRTA}}$ ( $\text{cm}^2\text{V}^{-1}\text{s}^{-1}$ )
MgO	mp-1265	Fm $\bar{3}m$	e	335.014	49.449	249.259	661.399
MgSe	mp-1315	Fm $\bar{3}m$	e	161.903	49.677	99.164	253.131
BaO	mp-1342	Fm $\bar{3}m$	e	45.699	36.568	29.595	68.895
SrTe	mp-1958	Fm $\bar{3}m$	e	87.838	50.777	41.630	88.205
TePb	mp-19717	Fm $\bar{3}m$	e	767.879	113.258	326.872	692.426
			h	821.565	130.865	380.792	742.284
PbS	mp-21276	Fm $\bar{3}m$	e	716.716	116.924	315.099	732.011
			h	970.055	135.590	409.376	972.705
KI	mp-22898	Fm $\bar{3}m$	e	53.472	52.961	20.748	53.321
CsBr	mp-22906	Pm $\bar{3}m$	e	49.171	57.964	17.833	48.193
AgCl	mp-22922	Fm $\bar{3}m$	e	131.972	67.404	55.888	137.639
TlCl	mp-23167	Pm $\bar{3}m$	e	101.805	79.755	43.198	102.253
			h	37.997	43.075	16.915	39.275
KBr	mp-23251	Fm $\bar{3}m$	e	36.883	46.137	15.194	38.085
KMgH <sub>3</sub>	mp-23737	Pm $\bar{3}m$	e	918.722	48.875	616.618	1553.698
			h	204.472	25.865	165.499	275.177
BaLiH <sub>3</sub>	mp-23818	Pm $\bar{3}m$	e	733.900	45.475	530.702	1009.339
			h	828.027	54.252	622.285	1075.864
RbCaH <sub>3</sub>	mp-23949	Pm $\bar{3}m$	e	85.735	35.125	43.730	99.709
KH	mp-24084	Fm $\bar{3}m$	e	187.805	34.077	158.555	307.775
RbAu	mp-30373	Pm $\bar{3}m$	e	177.172	76.587	79.886	165.883
			h	494.129	118.425	189.764	465.391
TlCl	mp-569639	Fm $\bar{3}m$	e	47.071	51.777	20.415	48.201
			h	28.704	39.295	13.344	29.935
CsBr	mp-571222	Fm $\bar{3}m$	e	32.908	46.682	11.718	32.308
KZnF <sub>3</sub>	mp-5878	Pm $\bar{3}m$	e	30.398	38.912	16.291	36.717
Mg <sub>3</sub> NF <sub>3</sub>	mp-7604	Pm $\bar{3}m$	e	110.175	44.297	73.129	170.656
CsCdF <sub>3</sub>	mp-8399	Pm $\bar{3}m$	e	32.196	43.026	15.918	35.941
Na <sub>3</sub> BrO	mp-985586	Pm $\bar{3}m$	e	60.907	57.061	27.305	61.161
RbBr	mp-22867	Fm $\bar{3}m$	e	34.377	46.729	12.825	34.012
TlBr	mp-22875	Pm $\bar{3}m$	e	145.634	94.114	55.569	138.408
			h	48.178	47.696	18.494	47.108

Materials	mp- <i>id</i>	Space Group	Carrier	$\mu^{\text{IBTE}}$ ( $\text{cm}^2\text{V}^{-1}\text{s}^{-1}$ )	$\mu^{\text{CRTA}}/\tau$ ( $\times 10^{14}\text{cm}^2\text{V}^{-1}\text{s}^{-2}$ )	$\mu^{\text{SERTA}}$ ( $\text{cm}^2\text{V}^{-1}\text{s}^{-1}$ )	$\mu^{\text{MRTA}}$ ( $\text{cm}^2\text{V}^{-1}\text{s}^{-1}$ )
LiI	mp-22899	Fm $\bar{3}m$	e	36.774	31.262	19.852	47.732
RbI	mp-22903	Fm $\bar{3}m$	e	48.757	52.319	17.189	47.502
RbH	mp-24721	Fm $\bar{3}m$	e	184.333	37.189	152.335	307.423
CaO	mp-2605	Fm $\bar{3}m$	e	85.794	31.518	63.057	152.445
CsAu	mp-2667	Pm $\bar{3}m$	e	195.725	77.645	77.829	181.937
			h	371.009	108.983	143.418	345.754
SrSe	mp-2758	Fm $\bar{3}m$	e	64.900	46.068	32.530	69.642
TlI	mp-571102	Fm $\bar{3}m$	e	86.899	59.860	33.195	83.347
			h	57.812	50.673	24.439	55.674
K <sub>3</sub> AuO	mp-9200	Pm $\bar{3}m$	e	60.168	46.759	26.770	59.241

**Table B.1:** Room-temperature phonon-limited carrier mobilities for the semiconductors of our dataset, obtained with our automated workflow and solving the IBTE or using the CRTA, SERTA and MRTA. The mp-*id* of the materials in the Materials Project is also given, together with the space group and the type of carriers. The convergence studies can be found in the Supplementaries of Ref. [42].

### B.1.2 Additional figures

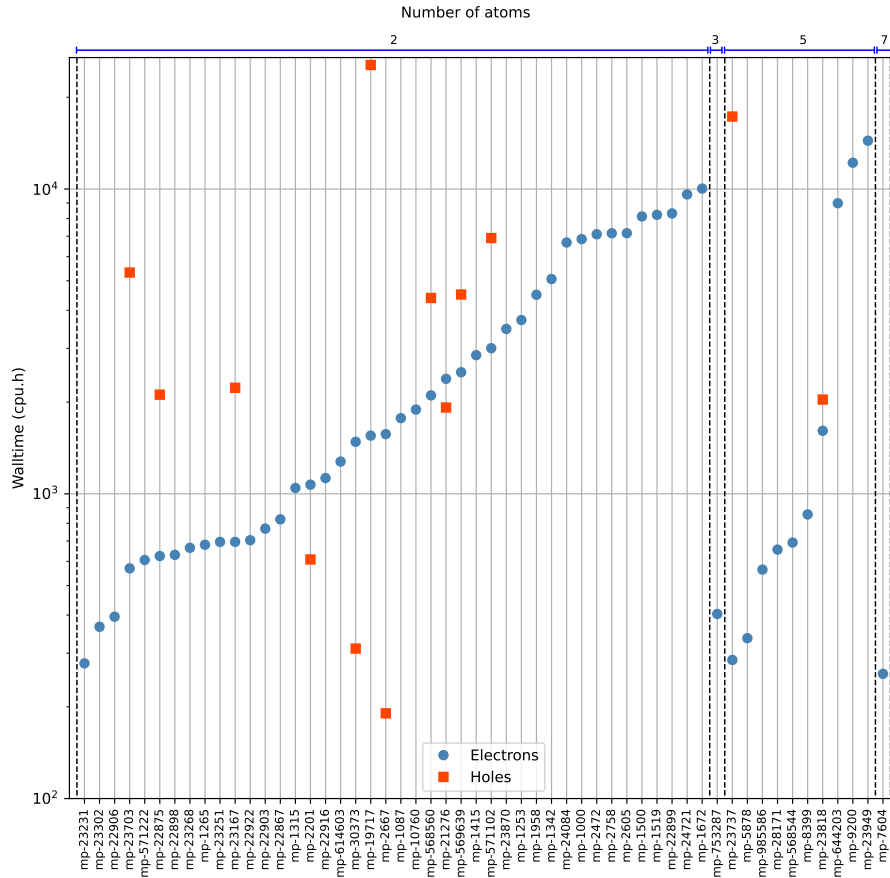


**Figure B.1:** Total needed wall-time to reach converged mobilities for the materials of our dataset, using our automated workflow, and within all the transport approximations detailed in the manuscript.

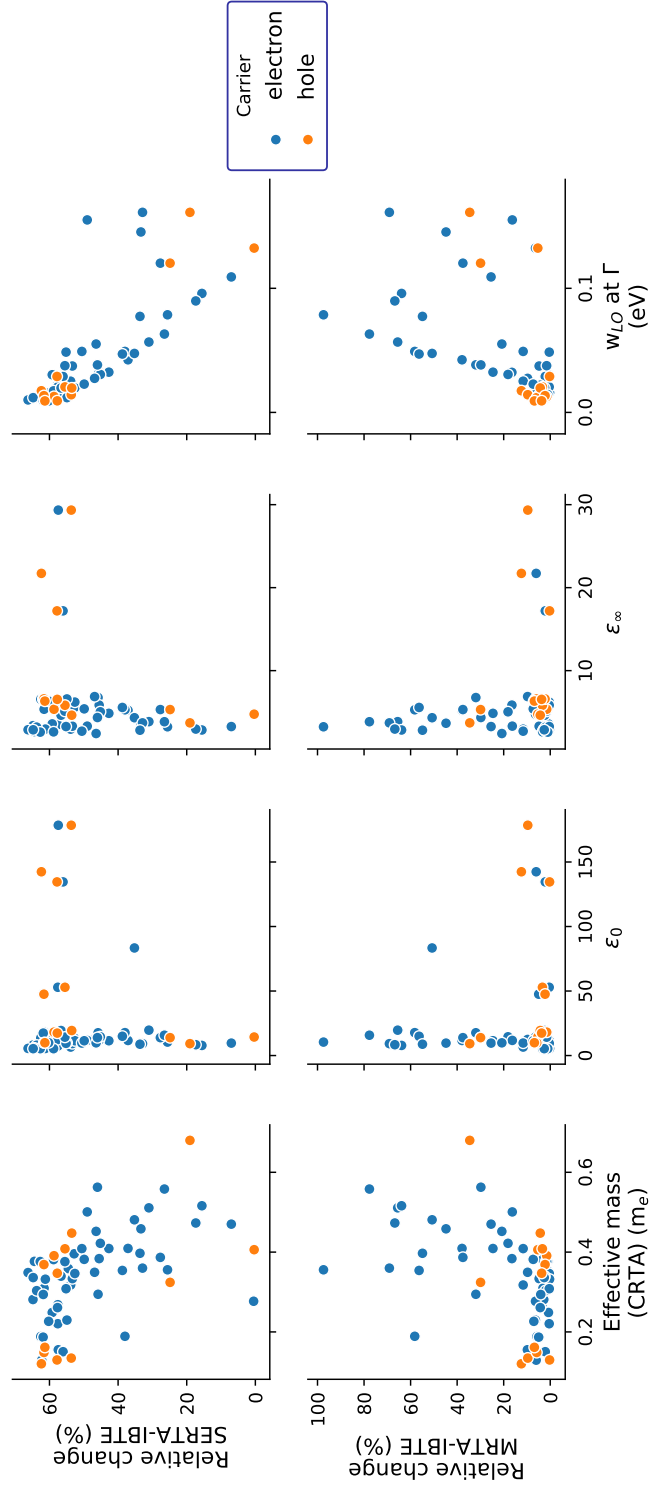


**Figure B.2:** Relative change between the SERTA/MRTA and the IBTE against well-known cheap material descriptors (i.e., the effective mass  $m_e$ , the static and high-frequency dielectric constants  $\epsilon_0$  and  $\epsilon_\infty$ , and the maximum LO frequency  $\omega_{LO}$ ).

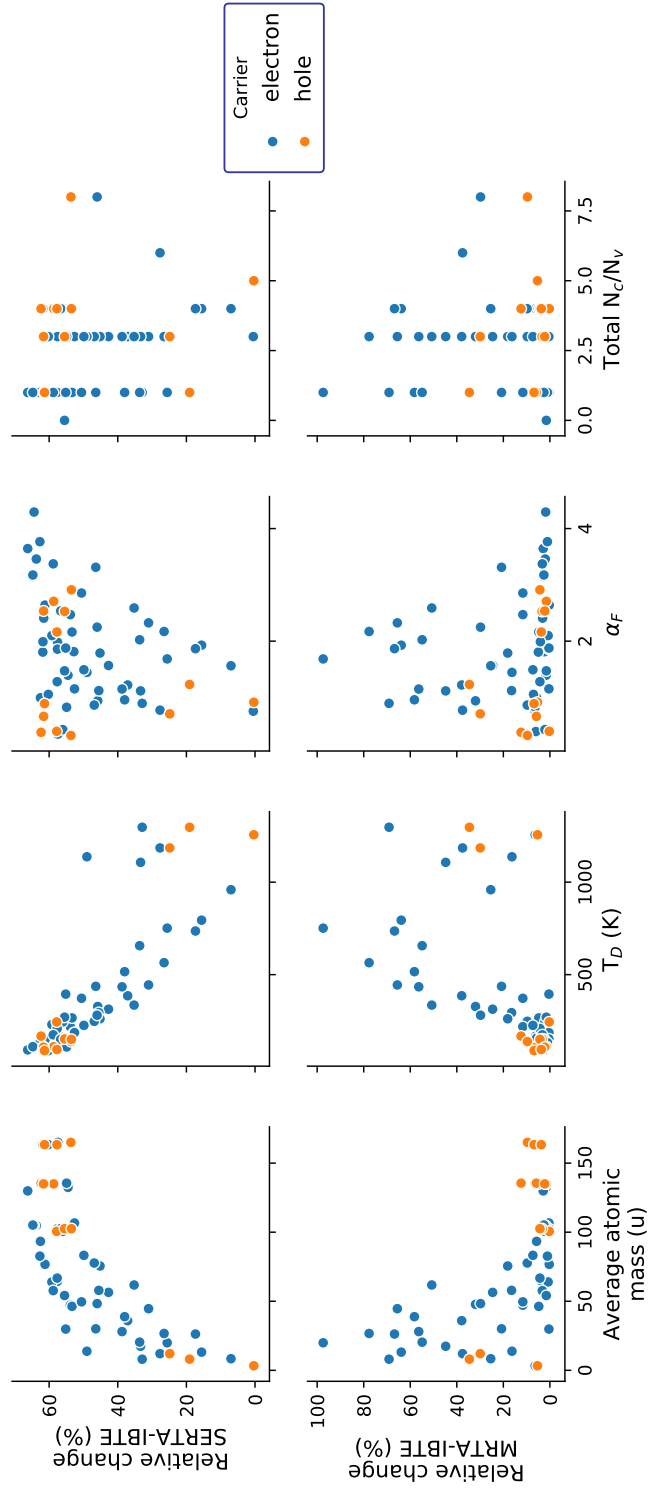


**Figure B.3:** Relative change between the SERTA/MRTA and the IBTE against well-known cheap material descriptors (i.e., the average atomic mass, the Debye temperature  $T_D$ , the Fröhlich constant  $\alpha_F$  and the total number of pockets taken into account in our calculations  $N_c$  or  $N_v$ ).

B.2 POTENTIAL NEW STATE-OF-THE-ART P-TYPE MATERIALS IN TIN (II) OXIDES

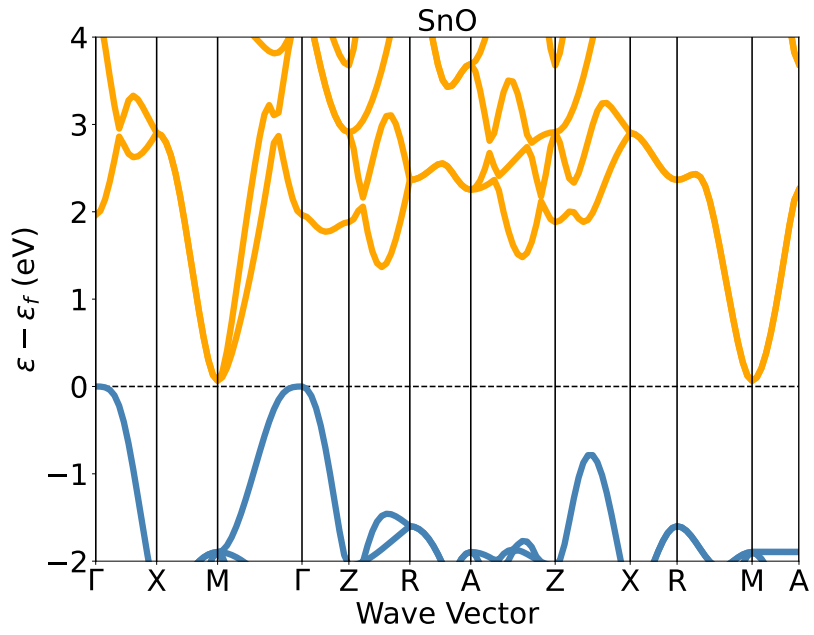
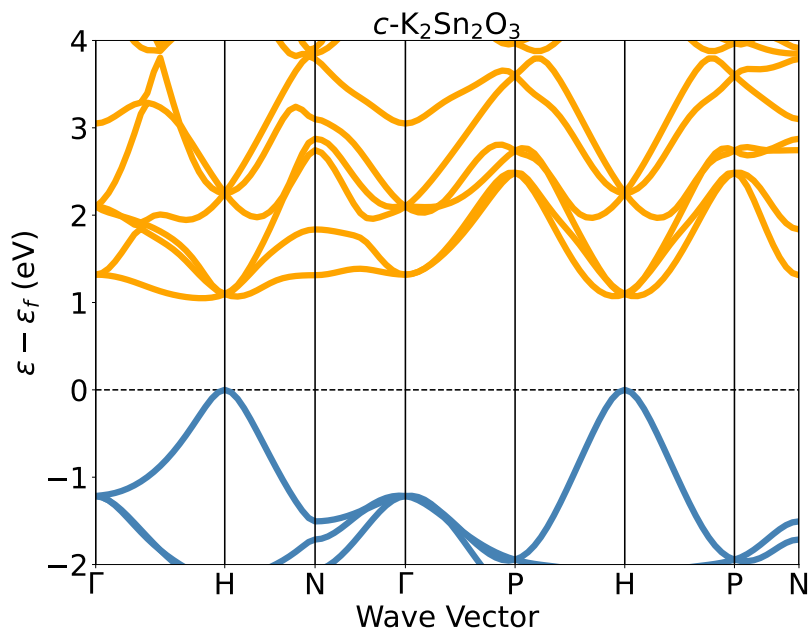
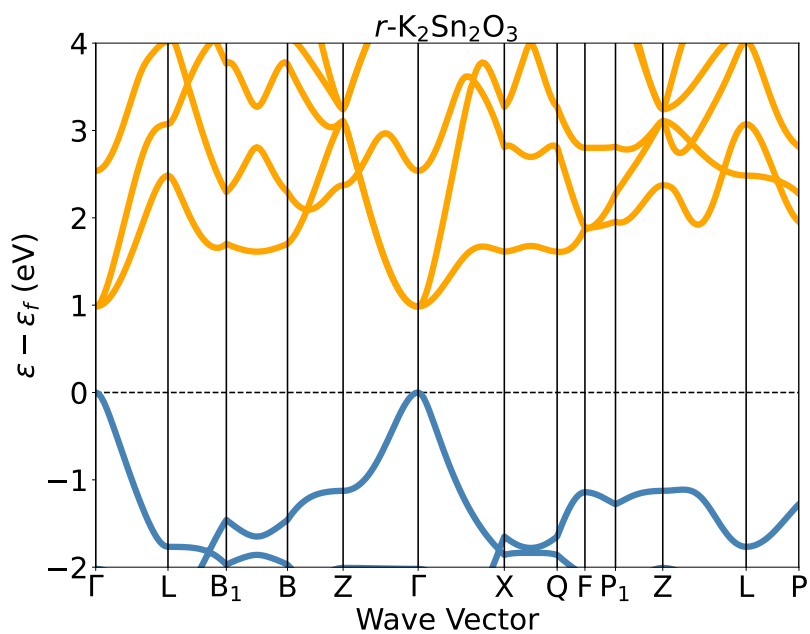


Figure B.4: Electronic band structure of SnO.



**Figure B.5:** Electronic band structure of  $c\text{-K}_2\text{Sn}_2\text{O}_3$ .



**Figure B.6:** Electronic band structure of  $r\text{-K}_2\text{Sn}_2\text{O}_3$ .

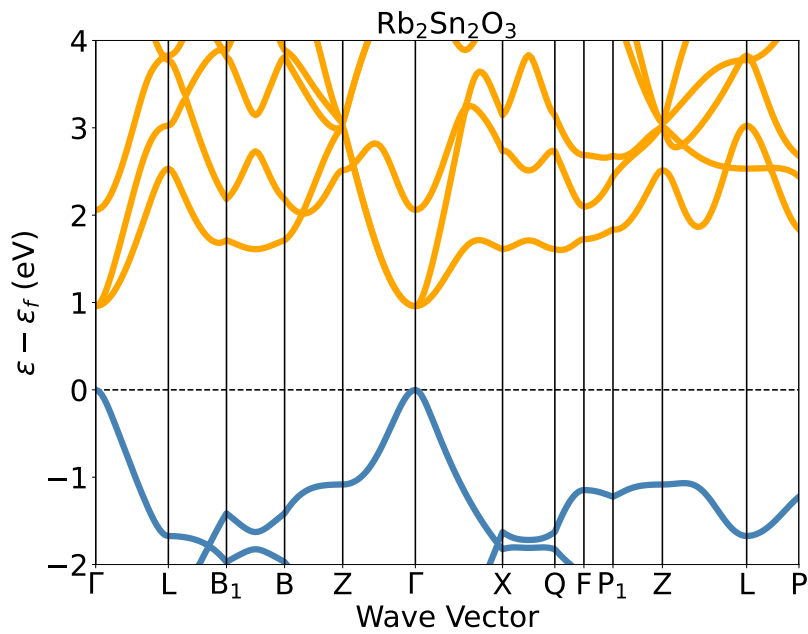


**Figure B.7:** Electronic band structure of  $\text{Rb}_2\text{Sn}_2\text{O}_3$ .

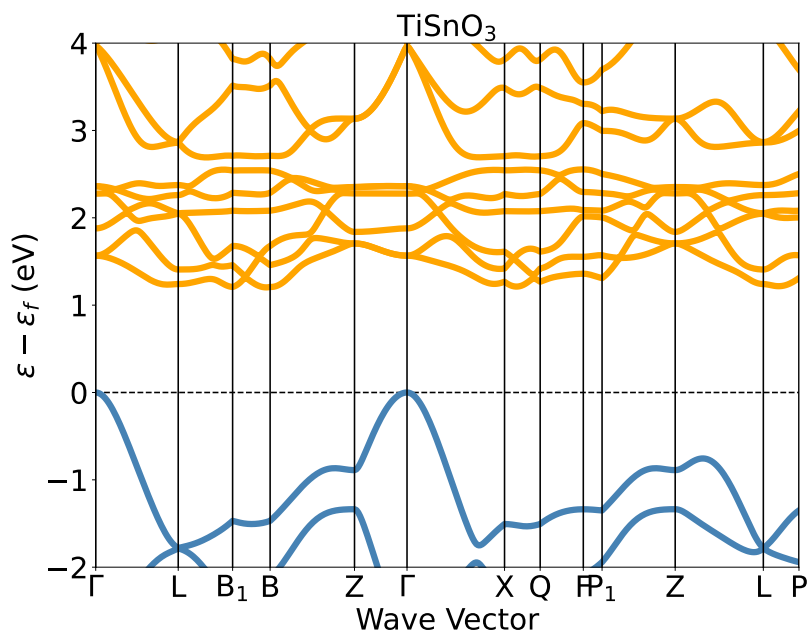


**Figure B.8:** Electronic band structure of  $\text{TiSnO}_3$ .

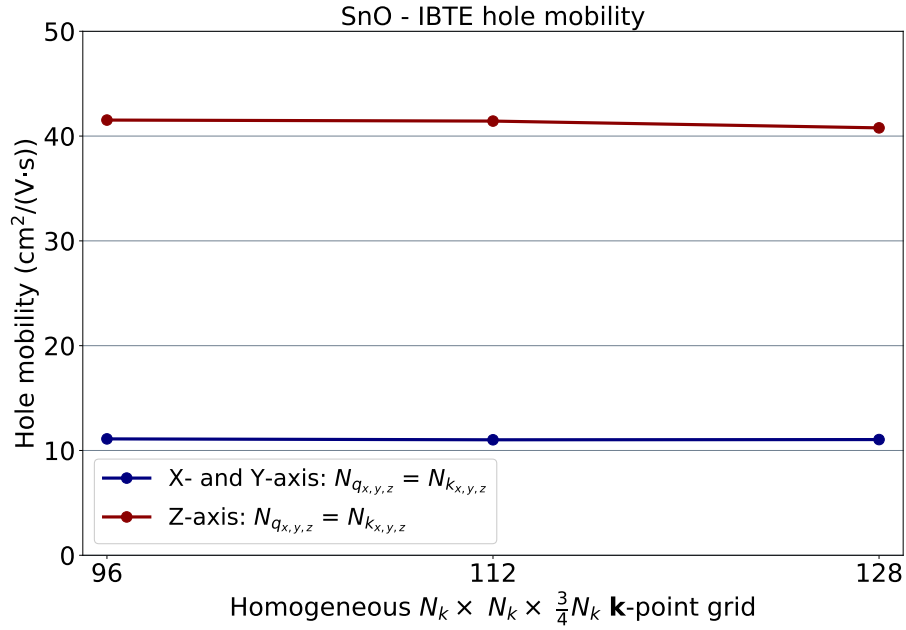


**Figure B.9:** Convergence of the IBTE hole mobility as a function of the  $\mathbf{k}$ - and  $\mathbf{q}$ -point grids in SnO. The values presented correspond to the Cartesian components of the IBTE mobility tensor and not the eigenvalues.

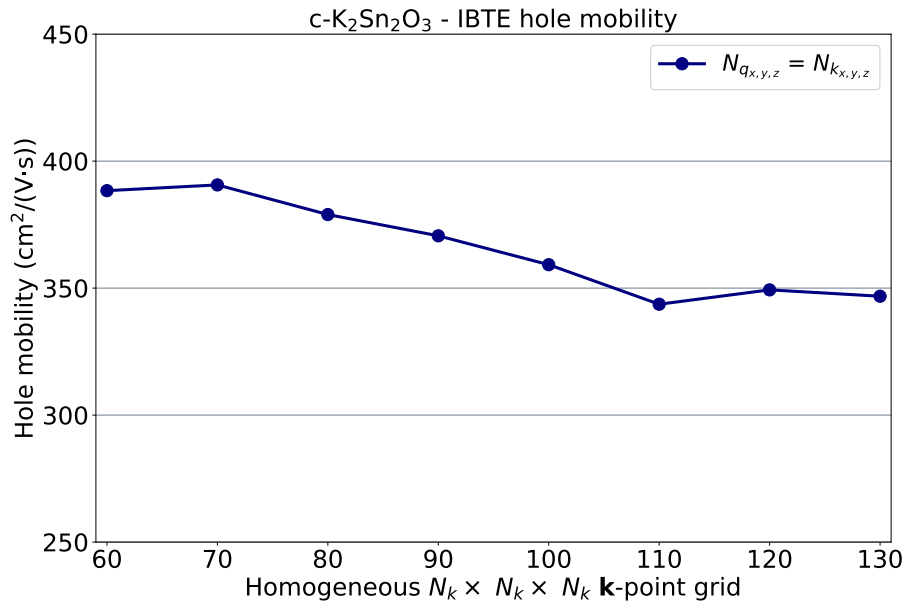


**Figure B.10:** Convergence of the IBTE hole mobility as a function of the  $\mathbf{k}$ - and  $\mathbf{q}$ -point grids in  $c$ -K<sub>2</sub>Sn<sub>2</sub>O<sub>3</sub>. The values presented correspond to the Cartesian components of the IBTE mobility tensor and not the eigenvalues.

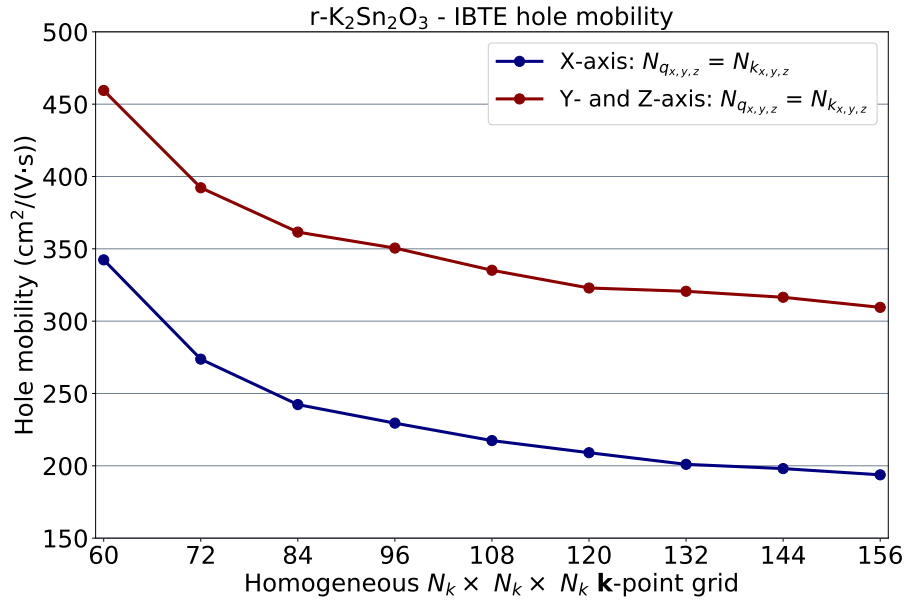


**Figure B.11:** Convergence of the IBTE hole mobility as a function of the  $\mathbf{k}$ - and  $\mathbf{q}$ -point grids in  $r$ -K<sub>2</sub>Sn<sub>2</sub>O<sub>3</sub>. The values presented correspond to the Cartesian components of the IBTE mobility tensor and not the eigenvalues.

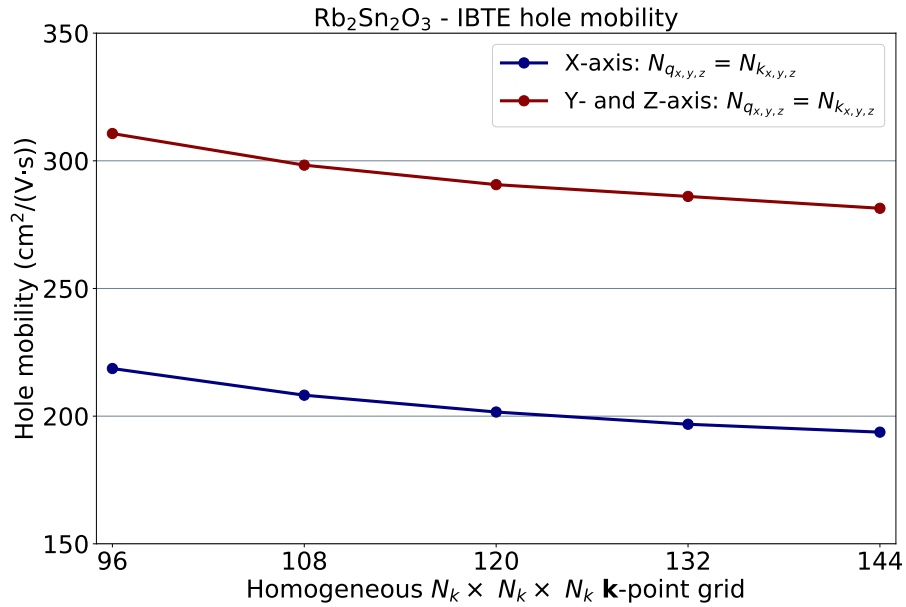


**Figure B.12:** Convergence of the IBTE hole mobility as a function of the  $\mathbf{k}$ - and  $\mathbf{q}$ -point grids in Rb<sub>2</sub>Sn<sub>2</sub>O<sub>3</sub>. The values presented correspond to the Cartesian components of the IBTE mobility tensor and not the eigenvalues.

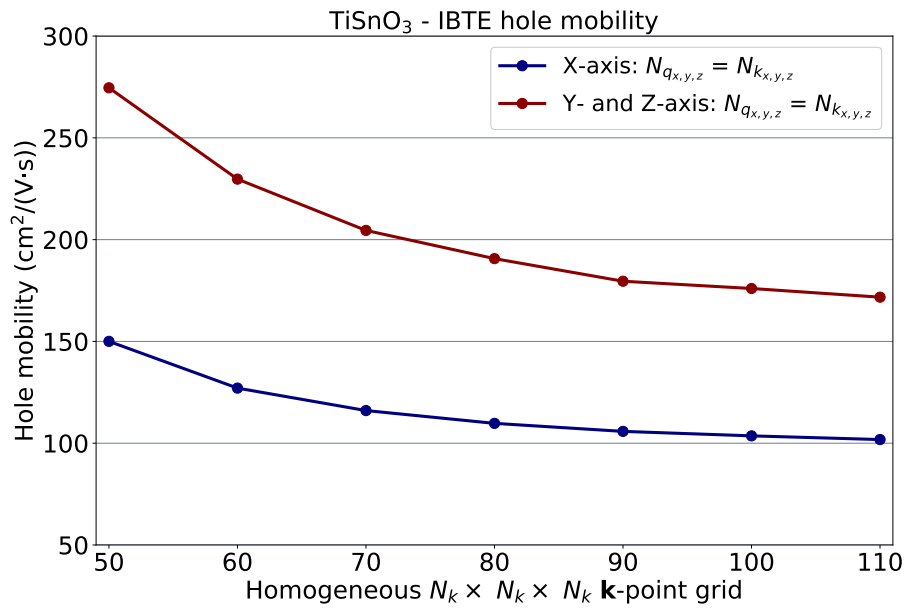


**Figure B.13:** Convergence of the IBTE hole mobility as a function of the  $\mathbf{k}$ - and  $\mathbf{q}$ -point grids in TiSnO<sub>3</sub>. The values presented correspond to the Cartesian components of the IBTE mobility tensor and not the eigenvalues.

## BIBLIOGRAPHY

---

- [1] P. Y. Yu and M. Cardona, *Fundamentals of Semiconductors* (Springer Berlin Heidelberg, 2010).
- [2] L. Zhang, Y. Zhou, L. Guo, W. Zhao, A. Barnes, H.-T. Zhang, C. Eaton, Y. Zheng, M. Brahlek, H. F. Haneef, N. J. Podraza, M. H. W. Chan, V. Gopalan, K. M. Rabe, and R. Engel-Herbert, *Nature Materials* **15**, 204 (2015).
- [3] K. Ellmer, *Nature Photonics* **6**, 809 (2012).
- [4] G. Brunin, F. Ricci, V.-A. Ha, G.-M. Rignanese, and G. Hautier, *npj Computational Materials* **5**, 1 (2019).
- [5] T. Minami, *Semiconductor Science and Technology* **20**, S35 (2005).
- [6] H. J. Kim, U. Kim, H. M. Kim, T. H. Kim, H. S. Mun, B.-G. Jeon, K. T. Hong, W.-J. Lee, C. Ju, K. H. Kim, and K. Char, *Applied Physics Express* **5**, 061102 (2012).
- [7] J. Zhang, J. Willis, Z. Yang, X. Lian, W. Chen, L.-S. Wang, X. Xu, T.-L. Lee, L. Chen, D. O. Scanlon, and K. H. Zhang, *Cell Reports Physical Science* **3**, 100801 (2022).
- [8] H. Kawazoe, H. Yanagi, K. Ueda, and H. Hosono, *MRS Bulletin* **25**, 28 (2000).
- [9] L. Chen, J. Yang, S. Klaus, L. J. Lee, R. Woods-Robinson, J. Ma, Y. Lum, J. K. Cooper, F. M. Toma, L.-W. Wang, I. D. Sharp, A. T. Bell, and J. W. Ager, *Journal of the American Chemical Society* **137**, 9595 (2015).
- [10] E. Fortunato, D. Ginley, H. Hosono, and D. C. Paine, *MRS Bulletin* **32**, 242 (2007).
- [11] N. F. Quackenbush, J. P. Allen, D. O. Scanlon, S. Sallis, J. A. Hewlett, A. S. Nandur, B. Chen, K. E. Smith, C. Weiland, D. A. Fischer, J. C. Woicik, B. E. White, G. W. Watson, and L. F. J. Piper, *Chemistry of Materials* **25**, 3114 (2013).

- [12] H. Kawazoe, M. Yasukawa, H. Hyodo, M. Kurita, H. Yanagi, and H. Hosono, *Nature* **389**, 939 (1997).
- [13] J. Shi, E. A. Rubinstein, W. Li, J. Zhang, Y. Yang, T.-L. Lee, C. Qin, P. Yan, J. L. MacManus-Driscoll, D. O. Scanlon, and K. H. Zhang, *Advanced Science* **9**, 2104141 (2022).
- [14] M.-L. Liu, L.-B. Wu, F.-Q. Huang, L.-D. Chen, and I.-W. Chen, *Journal of Applied Physics* **102**, 116108 (2007).
- [15] X. Zhang and L.-D. Zhao, *Journal of Materiomics* **1**, 92 (2015).
- [16] X.-L. Shi, J. Zou, and Z.-G. Chen, *Chemical Reviews* **120**, 7399 (2020).
- [17] G. J. Snyder and E. S. Toberer, *Nature Materials* **7**, 105 (2008).
- [18] C. Gayner and K. K. Kar, *Progress in Materials Science* **83**, 330 (2016).
- [19] G. Tan, L.-D. Zhao, and M. G. Kanatzidis, *Chemical Reviews* **116**, 12123 (2016).
- [20] Y. Wu, Z. Chen, P. Nan, F. Xiong, S. Lin, X. Zhang, Y. Chen, L. Chen, B. Ge, and Y. Pei, *Joule* **3**, 1276 (2019).
- [21] M. Hong, T. C. Chasapis, Z.-G. Chen, L. Yang, M. G. Kanatzidis, G. J. Snyder, and J. Zou, *ACS Nano* **10**, 4719 (2016).
- [22] M. Mukherjee, A. Srivastava, and A. K. Singh, *Journal of Materials Chemistry C* **10**, 12524–12555 (2022).
- [23] M. Zhou, G. J. Snyder, L. Li, and L.-D. Zhao, *Inorganic Chemistry Frontiers* **3**, 1449–1463 (2016).
- [24] A. Basit, J. Xin, G. Murtaza, L. Wei, A. Hameed, W. Guoyu, and J. Y. Dai, *EcoMat* **5**, e12391 (2023).
- [25] G. Rogl and P. Rogl, *Current Opinion in Green and Sustainable Chemistry* **4**, 50–57 (2017).
- [26] S. M. Kauzlarich, K. P. Devlin, and C. J. Perez, Zintl phases for thermoelectric applications, in *Thermoelectric Energy Conversion* (Elsevier, 2021) p. 157–182.

- [27] H. Cheng, Q. Le, Z. Liu, Q. Qian, Y. Zhao, and J. Ouyang, *Journal of Materials Chemistry C* **10**, 433–450 (2022).
- [28] P. Ying, R. He, J. Mao, Q. Zhang, H. Reith, J. Sui, Z. Ren, K. Nielsch, and G. Schierning, *Nature Communications* **12**, 1121 (2021).
- [29] R. Moshwan, W.-D. Liu, X.-L. Shi, Y.-P. Wang, J. Zou, and Z.-G. Chen, *Nano Energy* **65**, 104056 (2019).
- [30] Y. Pei, X. Shi, A. LaLonde, H. Wang, L. Chen, and G. J. Snyder, *Nature* **473**, 66 (2011).
- [31] W. Liu, X. Tan, K. Yin, H. Liu, X. Tang, J. Shi, Q. Zhang, and C. Uher, *Physical Review Letters* **108**, 166601 (2012).
- [32] K. Xia, P. Nan, S. Tan, Y. Wang, B. Ge, W. Zhang, S. Anand, X. Zhao, G. J. Snyder, and T. Zhu, *Energy & Environmental Science* **12**, 1568 (2019).
- [33] D. Qin, B. Cui, X. Meng, P. Qin, L. Xie, Q. Zhang, W. Liu, J. Cao, W. Cai, and J. Sui, *Materials Today Physics* **8**, 128 (2019).
- [34] E. S. Toberer, C. A. Cox, S. R. Brown, T. Ikeda, A. F. May, S. M. Kauzlarich, and G. J. Snyder, *Advanced Functional Materials* **18**, 2795 (2008).
- [35] E. S. Toberer, A. F. May, and G. J. Snyder, *Chemistry of Materials* **22**, 624 (2009).
- [36] F. Bloch, *Zeitschrift für physik* **52**, 555 (1929).
- [37] X. Gonze and C. Lee, *Physical Review B* **55**, 10355 (1997).
- [38] S. Baroni, S. de Gironcoli, A. D. Corso, and P. Giannozzi, *Reviews of Modern Physics* **73**, 515 (2001).
- [39] R. LeSar, *Introduction to computational materials science: fundamentals to applications* (Cambridge University Press, 2013).
- [40] R. M. Martin, *Electronic Structure* (Cambridge University Press, 2020).
- [41] D. Chatfield, *Theoretical Chemistry Accounts: Theory, Computation, and Modeling (Theoretica Chimica Acta)* **108**, 367 (2002).

- [42] R. Claes, G. Brunin, M. Giantomassi, G.-M. Rignanese, and G. Hautier, *Physical Review B* **106**, 094302 (2022).
- [43] S. O. Kasap, *Principles of electronic materials and devices*, Vol. 2 (McGraw-Hill New York, 2006).
- [44] S. Poncé, W. Li, S. Reichardt, and F. Giustino, *Reports on Progress in Physics* **83**, 036501 (2020).
- [45] S. Poncé, E. R. Margine, and F. Giustino, *Physical Review B* **97**, 121201 (2018).
- [46] J. M. Ziman, *Principles of the theory of solids*, 2nd ed. (Cambridge University Press, 1972).
- [47] F. J. Blatt, in *Solid State Physics*, Vol. 4 (Elsevier, 1957) pp. 199–366.
- [48] G. Brunin, H. P. C. Miranda, M. Giantomassi, M. Royo, M. Stengel, M. J. Verstraete, X. Gonze, G.-M. Rignanese, and G. Hautier, *Physical Review B* **102**, 094308 (2020).
- [49] F. Giustino, *Reviews of Modern Physics* **89**, 015003 (2017).
- [50] W. Li, J. Carrete, N. A. Katcho, and N. Mingo, *Computer Physics Communications* **185**, 1747 (2014).
- [51] P. E. Blöchl, O. Jepsen, and O. K. Andersen, *Physical Review B* **49**, 16223 (1994).
- [52] G. Brunin, H. P. C. Miranda, M. Giantomassi, M. Royo, M. Stengel, M. J. Verstraete, X. Gonze, G.-M. Rignanese, and G. Hautier, *Physical Review Letters* **125**, 136601 (2020).
- [53] A. M. Ganose, J. Park, A. Faghaninia, R. Woods-Robinson, K. A. Persson, and A. Jain, *Nature Communications* **12**, 2222 (2021).
- [54] M. Fiorentini and N. Bonini, *Physical Review B* **94**, 085204 (2016).
- [55] A. Cepellotti, J. Coulter, A. Johansson, N. S. Fedorova, and B. Kozinsky, *Journal of Physics: Materials* **5**, 035003 (2022).
- [56] D. Rode, in *Semiconductors and Semimetals* (Elsevier, 1975) pp. 1–89.
- [57] K. Ghosh and U. Singiseti, *Journal of Applied Physics* **117**, 065703 (2015).

- [58] G. K. H. Madsen and D. J. Singh, *Computer Physics Communications* **175**, 67 (2006).
- [59] G. K. H. Madsen, J. Carrete, and M. J. Verstraete, *Computer Physics Communications* **231**, 140 (2018).
- [60] D. M. Smiadak, R. Claes, N. Perez, M. Marshall, W. Peng, W. Chen, G. Hautier, G. Schierning, and A. Zevalkink, *Materials Today Physics* , 100597 (2022).
- [61] R. Chmielowski, D. Péré, C. Bera, I. Opahle, W. Xie, S. Jacob, F. Capet, P. Roussel, A. Weidenkaff, G. K. Madsen, *et al.*, *Journal of Applied Physics* **117**, 125103 (2015).
- [62] G. Hautier, A. Miglio, G. Ceder, G.-M. Rignanese, and X. Gonze, *Nature Communications* **4**, 1 (2013).
- [63] F. Ricci, W. Chen, U. Aydemir, G. J. Snyder, G.-M. Rignanese, A. Jain, and G. Hautier, *Scientific Data* **4**, 1 (2017).
- [64] F. Ricci, A. Dunn, A. Jain, G.-M. Rignanese, and G. Hautier, *Journal of Materials Chemistry A* **8**, 17579 (2020).
- [65] A. Faghaninia, G. Yu, U. Aydemir, M. Wood, W. Chen, G.-M. Rignanese, G. J. Snyder, G. Hautier, and A. Jain, *Physical Chemistry Chemical Physics* **19**, 6743 (2017).
- [66] Z. M. Gibbs, F. Ricci, G. Li, H. Zhu, K. Persson, G. Ceder, G. Hautier, A. Jain, and G. J. Snyder, *npj Computational Materials* **3**, 1 (2017).
- [67] W. Chen, J.-H. Pöhls, G. Hautier, D. Broberg, S. Bajaj, U. Aydemir, Z. M. Gibbs, H. Zhu, M. Asta, G. J. Snyder, B. Meredig, M. A. White, K. Persson, and A. Jain, *Journal of Materials Chemistry C* **4**, 4414 (2016).
- [68] W. Li, *Physical Review B* **92**, 075405 (2015).
- [69] G. Samsonidze and B. Kozinsky, *Advanced Energy Materials* **8**, 1800246 (2018).
- [70] T. Deng, G. Wu, M. B. Sullivan, Z. M. Wong, K. Hippalgaonkar, J.-S. Wang, and S.-W. Yang, *npj Computational Materials* **6**, 10.1038/s41524-020-0316-7 (2020).

- [71] H. Lee, S. Poncé, K. Bushick, S. Hajinazar, J. Lafuente-Bartolome, J. Leveillee, C. Lian, F. Macheda, H. Paudyal, W. H. Sio, *et al.*, arXiv preprint arXiv:2302.08085 (2023).
- [72] J.-J. Zhou, J. Park, I.-T. Lu, I. Maliyov, X. Tong, and M. Bernardi, *Computer Physics Communications* **264**, 107970 (2021).
- [73] S. Poncé, E. R. Margine, C. Verdi, and F. Giustino, *Computer Physics Communications* **209**, 116 (2016).
- [74] A. A. Mostofi, J. R. Yates, Y.-S. Lee, I. Souza, D. Vanderbilt, and N. Marzari, *Computer Physics Communications* **178**, 685 (2008).
- [75] G. Pizzi, V. Vitale, R. Arita, S. Blügel, F. Freimuth, G. Géranton, M. Gibertini, D. Gresch, C. Johnson, T. Koretsune, J. Ibañez-Azpiroz, H. Lee, J.-M. Lihm, D. Marchand, A. Marrazzo, Y. Mokrousov, J. I. Mustafa, Y. Nohara, Y. Nomura, L. Paulatto, S. Poncé, T. Ponweiser, J. Qiao, F. Thöle, S. S. Tsirkin, M. Wierzbowska, N. Marzari, D. Vanderbilt, I. Souza, A. A. Mostofi, and J. R. Yates, *Journal of Physics: Condensed Matter* **32**, 165902 (2020).
- [76] A. Damle, L. Lin, and L. Ying, *Journal of Computational Physics* **334**, 1 (2017).
- [77] V. Vitale, G. Pizzi, A. Marrazzo, J. R. Yates, N. Marzari, and A. A. Mostofi, *npj Computational Materials* **6**, 10.1038/s41524-020-0312-y (2020).
- [78] J. Qiao, G. Pizzi, and N. Marzari, Projectability disentanglement for accurate and automated electronic-structure hamiltonians (2023).
- [79] J. Qiao, G. Pizzi, and N. Marzari, Automated mixing of maximally localized wannier functions into target manifolds (2023).
- [80] A. H. Romero, D. C. Allan, B. Amadon, G. Antonius, T. Applencourt, L. Baguet, J. Bieder, F. Bottin, J. Bouchet, E. Bousquet, F. Bruneval, G. Brunin, D. Caliste, M. Côté, J. Denier, C. Dreyer, P. Ghosez, M. Giantomassi, Y. Gillet, O. Gingras, D. R. Hamann, G. Hautier, F. Jollet, G. Jomard, A. Martin, H. P. C. Miranda, F. Naccarato, G. Petretto, N. A. Pike, V. Planes, S. Prokhorenko, T. Rangel, F. Ricci, G.-M. Rignanese, M. Royo, M. Stengel, M. Torrent, M. J. van Setten, B. V. Troeye, M. J. Verstraete, J. Wiktor, J. W.

Zwanziger, and X. Gonze, *The Journal of Chemical Physics* **152**, 10.1063/1.5144261 (2020).

- [81] X. Gonze, B. Amadon, G. Antonius, F. Arnardi, L. Baguet, J.-M. Beuken, J. Bieder, F. Bottin, J. Bouchet, E. Bousquet, N. Brouwer, F. Bruneval, G. Brunin, T. Cavignac, J.-B. Charraud, W. Chen, M. Côté, S. Cottenier, J. Denier, G. Geneste, P. Ghosez, M. Giantomassi, Y. Gillet, O. Gingras, D. R. Hamann, G. Hautier, X. He, N. Helbig, N. Holzwarth, Y. Jia, F. Jollet, W. Lafargue-Dit-Hauret, K. Lejaeghere, M. A. Marques, A. Martin, C. Martins, H. P. Miranda, F. Naccarato, K. Persson, G. Petretto, V. Planes, Y. Pouillon, S. Prokhorenko, F. Ricci, G.-M. Rignanese, A. H. Romero, M. M. Schmitt, M. Torrent, M. J. van Setten, B. V. Troeye, M. J. Verstraete, G. Zérah, and J. W. Zwanziger, *Computer Physics Communications* **248**, 107042 (2020).
- [82] C. Verdi and F. Giustino, *Physical Review Letters* **115**, 176401 (2015).
- [83] V. A. Jhalani, J.-J. Zhou, J. Park, C. E. Dreyer, and M. Bernardi, *Physical Review Letters* **125**, 136602 (2020).
- [84] J. Park, J.-J. Zhou, V. A. Jhalani, C. E. Dreyer, and M. Bernardi, *Physical Review B* **102**, 125203 (2020).
- [85] S. Poncé, F. Macheda, E. R. Margine, N. Marzari, N. Bonini, and F. Giustino, *Physical Review Research* **3**, 043022 (2021).
- [86] S. Poncé, M. Royo, M. Stengel, N. Marzari, and M. Gibertini, *Physical Review B* **107**, 155424 (2023).
- [87] M. Stengel, *Physical Review B* **88**, 174106 (2013).
- [88] R. M. Martin, *Physical Review B* **5**, 1607 (1972).
- [89] S. Poncé, M. Royo, M. Gibertini, N. Marzari, and M. Stengel, *Physical Review Letters* **130**, 166301 (2023).
- [90] M. Royo and M. Stengel, *Physical Review X* **11**, 041027 (2021).
- [91] T. Sohler, M. Calandra, and F. Mauri, *Physical Review B* **96**, 075448 (2017).
- [92] T. Sohler, D. Campi, N. Marzari, and M. Gibertini, *Physical Review Materials* **2**, 114010 (2018).

- [93] M. Giantomassi *et al.*, AbiPy project, <https://github.com/abinit/abipy> (2023).
- [94] G. Petretto, S. Dwaraknath, H. P. Miranda, D. Winston, M. Giantomassi, M. J. van Setten, X. Gonze, K. A. Persson, G. Hautier, and G.-M. Rignanese, *Scientific Data* **5**, 1 (2018).
- [95] G. Petretto, X. Gonze, G. Hautier, and G.-M. Rignanese, *Computational Materials Science* **144**, 331 (2018).
- [96] A. Jain, S. P. Ong, G. Hautier, W. Chen, W. D. Richards, S. Dacek, S. Cholia, D. Gunter, D. Skinner, G. Ceder, and K. A. Persson, *APL Materials* **1**, 011002 (2013).
- [97] M. van Setten, M. Giantomassi, E. Bousquet, M. Verstraete, D. Hamann, X. Gonze, and G.-M. Rignanese, *Computer Physics Communications* **226**, 39 (2018).
- [98] J. Ma, A. S. Nissimagoudar, and W. Li, *Physical Review B* **97**, 045201 (2018).
- [99] J. Willis, R. Claes, Q. Zhou, M. Giantomassi, G.-M. Rignanese, G. Hautier, and D. O. Scanlon, *Limits to hole mobility and doping in copper iodide* (2023).
- [100] J. Ma, Y. Chen, and W. Li, *Physical Review B* **97**, 205207 (2018).
- [101] T.-H. Liu, J. Zhou, B. Liao, D. J. Singh, and G. Chen, *Physical Review B* **95**, 075206 (2017).
- [102] J.-J. Zhou and M. Bernardi, *Physical Review B* **94**, 201201 (2016).
- [103] H. Fröhlich, *Advances in Physics* **3**, 325 (1954).
- [104] W. A. Harrison, *Physical Review* **104**, 1281 (1956).
- [105] C. Herring and E. Vogt, *Physical Review* **101**, 944 (1956).
- [106] P. Vogl, *Physical Review B* **13**, 694 (1976).
- [107] Y. Hu, J. Hwang, Y. Lee, P. Conlin, D. G. Schlom, S. Datta, and K. Cho, *Journal of Applied Physics* **126**, 185701 (2019).
- [108] Y. Hu, X. Yao, D. G. Schlom, S. Datta, and K. Cho, *Chemistry of Materials* **33**, 212 (2020).

- [109] M. Schlipf, S. Poncé, and F. Giustino, *Physical Review Letters* **121**, 086402 (2018).
- [110] B. Guster, P. Melo, B. A. A. Martin, V. Brousseau-Couture, J. C. de Abreu, A. Miglio, M. Giantomassi, M. Côté, J. M. Frost, M. J. Verstraete, and X. Gonze, *Physical Review B* **104**, 235123 (2021).
- [111] A. M. Ganose, J. Park, and A. Jain, arXiv preprint arXiv:2210.01746 (2022).
- [112] F. Macheda and N. Bonini, *Physical Review B* **98**, 201201 (2018).
- [113] D. C. Desai, B. Zviazhynski, J.-J. Zhou, and M. Bernardi, *Physical Review B* **103**, L161103 (2021).
- [114] H. Brooks, in *Physical Review*, Vol. 83 (American Physical Soc One Physics Ellipse, College PK, MD 20740-3844 USA, 1951) pp. 879–879.
- [115] J. Leveillee, X. Zhang, E. Kioupakis, and F. Giustino, *Physical Review B* **107**, 125207 (2023).
- [116] A. Jain, S. P. Ong, W. Chen, B. Medasani, X. Qu, M. Kocher, M. Brafman, G. Petretto, G.-M. Rignanese, G. Hautier, D. Gunter, and K. A. Persson, *Concurrency and Computation: Practice and Experience* **27**, 5037 (2015).
- [117] G. Pizzi, A. Cepellotti, R. Sabatini, N. Marzari, and B. Kozinsky, *Computational Materials Science* **111**, 218–230 (2016).
- [118] K. Mathew, J. H. Montoya, A. Faghaninia, S. Dwarakanath, M. Aykol, H. Tang, I. heng Chu, T. Smidt, B. Bocklund, M. Horton, J. Dagdelen, B. Wood, Z.-K. Liu, J. Neaton, S. P. Ong, K. Persson, and A. Jain, *Computational Materials Science* **139**, 140 (2017).
- [119] J. T. Devreese, Fröhlich polarons. lecture course including detailed theoretical derivations – 10th edition (2016).
- [120] D. Emin, *Polarons in condensed matter* (2022).
- [121] W. H. Sio, C. Verdi, S. Poncé, and F. Giustino, *Physical Review Letters* **122**, 246403 (2019).
- [122] W. H. Sio, C. Verdi, S. Poncé, and F. Giustino, *Physical Review B* **99**, 235139 (2019).

- [123] L. E. Bell, *Science* **321**, 1457 (2008).
- [124] L.-D. Zhao, S.-H. Lo, Y. Zhang, H. Sun, G. Tan, C. Uher, C. Wolverton, V. P. Dravid, and M. G. Kanatzidis, *Nature* **508**, 373 (2014).
- [125] J. H. Dennis, Anisotropy of thermoelectric power in bismuth telluride (1961).
- [126] D.-Y. Chung, S. D. Mahanti, W. Chen, C. Uher, and M. G. Kanatzidis, *MRS Proceedings* **793**, S6 (2003).
- [127] J. Xin, G. Li, G. Auffermann, H. Borrmann, W. Schnelle, J. Gooth, X. Zhao, T. Zhu, C. Felser, and C. Fu, *Materials Today Physics* **7**, 61 (2018).
- [128] S. M. Kauzlarich (1996).
- [129] J. Shuai, H. Geng, Y. Lan, Z. Zhu, C. Wang, Z. Liu, J. Bao, C.-W. Chu, J. Sui, and Z. Ren, *Proceedings of the National Academy of Sciences* **113**, E4125 (2016).
- [130] B. R. Ortiz, P. Gorai, V. Stevanović, and E. S. Toberer, *Chemistry of Materials* **29**, 4523 (2017).
- [131] U. Aydemir, A. Zevalkink, A. Ormeci, Z. M. Gibbs, S. Bux, and G. J. Snyder, *Chemistry of Materials* **27**, 1622 (2015).
- [132] A. Zevalkink, G. S. Pomrehn, S. Johnson, J. Swallow, Z. M. Gibbs, and G. J. Snyder, *Chemistry of Materials* **24**, 2091 (2012).
- [133] J. Sun and D. J. Singh, *Journal of Materials Chemistry A* **5**, 17088 (2017).
- [134] B. Xu, R. Li, G. Yu, S. Ma, Y. Wang, Y. Wang, and L. Yi, *Journal of the Physical Society of Japan* **86**, 024601 (2017).
- [135] G. Yang, G. Zhang, C. Wang, and Y. Wang, *Solid State Communications* **237-238**, 28 (2016).
- [136] R. A. Ribeiro and M. A. Avila, *Philosophical Magazine* **92**, 2492 (2012).
- [137] A. Zevalkink, J. Swallow, and G. J. Snyder, *Dalton Transactions* **42**, 9713 (2013).
- [138] C. Uher, ed., *Materials Aspect of Thermoelectricity* (CRC Press, 2016).

- [139] G. Hautier, A. Miglio, D. Waroquiers, G.-M. Rignanese, and X. Gonze, *Chemistry of Materials* **26**, 5447 (2014).
- [140] D. S. Parker, A. F. May, and D. J. Singh, *Physical Review Applied* **3**, 064003 (2015).
- [141] B. M. Askerov, *Electron transport phenomena in semiconductors* (World scientific, 1994).
- [142] Z. Hashin and S. Shtrikman, *Physical Review* **130**, 129 (1963).
- [143] R. E. Newnham, *Properties of materials: anisotropy, symmetry, structure* (Oxford university press, 2005).
- [144] K. Lee, S. Kamali, T. Ericsson, M. Bellard, and K. Kovnir, *Chemistry of Materials* **28**, 2776 (2016).
- [145] R. McKinney, P. Gorai, E. S. Toberer, and V. Stevanovic', *Chemistry of Materials* **31**, 2048 (2019).
- [146] M. de Jong, W. Chen, T. Angsten, A. Jain, R. Notestine, A. Gamst, M. Sluiter, C. K. Ande, S. van der Zwaag, J. J. Plata, C. Toher, S. Curtarolo, G. Ceder, K. A. Persson, and M. Asta, *Scientific Data* **2**, 150009 (2015).
- [147] L. Seixas, L. B. Abdalla, T. M. Schmidt, A. Fazzio, and R. H. Miwa, *Journal of Applied Physics* **113**, 023705 (2013).
- [148] D. Ibrahim, J.-B. Vaney, S. Sassi, C. Candolfi, V. Ohorodniichuk, P. Levinsky, C. Semprimoschnig, A. Dauscher, and B. Lenoir, *Applied Physics Letters* **110**, 032103 (2017).
- [149] L. Ivanova, Y. V. Granatkina, and Y. A. Sidorov, *Neorganicheskie Materialy* **35**, 44 (1999).
- [150] L. E. Shelimova, T. E. Svechnikova, P. P. Konstantinov, O. G. Karpinskii, E. S. Avilov, M. A. Kretova, and V. S. Zemskov, *Inorganic Materials* **43**, 125 (2007).
- [151] D. O. Scanlon, A. Walsh, B. J. Morgan, G. W. Watson, D. J. Payne, and R. G. Egdell, *Physical Review B* **79**, 035101 (2009).
- [152] T. Arnold, D. J. Payne, A. Bourlange, J. P. Hu, R. G. Egdell, L. F. J. Piper, L. Colakerol, A. D. Masi, P.-A. Glans, T. Learmonth, K. E. Smith, J. Guo, D. O. Scanlon, A. Walsh, B. J. Morgan, and G. W. Watson, *Physical Review B* **79**, 075102 (2009).

- [153] D. Shin, J. S. Foord, D. J. Payne, T. Arnold, D. J. Aston, R. G. Egdell, K. G. Godinho, D. O. Scanlon, B. J. Morgan, G. W. Watson, E. Mugnier, C. Yaicle, A. Rougier, L. Colakerol, P. A. Glans, L. F. J. Piper, and K. E. Smith, *Physical Review B* **80**, 233105 (2009).
- [154] D. O. Scanlon, B. J. Morgan, G. W. Watson, and A. Walsh, *Physical Review Letters* **103**, 096405 (2009).
- [155] D. O. Scanlon, A. Walsh, and G. W. Watson, *Chemistry of Materials* **21**, 4568 (2009).
- [156] D. O. Scanlon and G. W. Watson, *The Journal of Physical Chemistry Letters* **1**, 3195 (2010).
- [157] D. O. Scanlon and G. W. Watson, *The Journal of Physical Chemistry Letters* **1**, 2582 (2010).
- [158] D. O. Scanlon, K. G. Godinho, B. J. Morgan, and G. W. Watson, *The Journal of Chemical Physics* **132**, 024707 (2010).
- [159] K. G. Godinho, J. J. Carey, B. J. Morgan, D. O. Scanlon, and G. W. Watson, *J. Mater. Chem.* **20**, 1086 (2010).
- [160] D. O. Scanlon and G. W. Watson, *Journal of Materials Chemistry* **21**, 3655 (2011).
- [161] K. G. Godinho, B. J. Morgan, J. P. Allen, D. O. Scanlon, and G. W. Watson, *Journal of Physics: Condensed Matter* **23**, 334201 (2011).
- [162] D. O. Scanlon, J. Buckeridge, C. R. A. Catlow, and G. W. Watson, *J. Mater. Chem. C* **2**, 3429 (2014).
- [163] J. Y. Zhang, W. W. Li, R. L. Z. Hoye, J. L. MacManus-Driscoll, M. Budde, O. Bierwagen, L. Wang, Y. Du, M. J. Wahila, L. F. J. Piper, T.-L. Lee, H. J. Edwards, V. R. Dhanak, and K. H. L. Zhang, *Journal of Materials Chemistry C* **6**, 2275 (2018).
- [164] Y. Li, D. J. Singh, M.-H. Du, Q. Xu, L. Zhang, W. Zheng, and Y. Ma, *Journal of Materials Chemistry C* **4**, 4592 (2016).
- [165] K. H. L. Zhang, Y. Du, A. Papadogianni, O. Bierwagen, S. Sallis, L. F. J. Piper, M. E. Bowden, V. Shutthanandan, P. V. Sushko, and S. A. Chambers, *Advanced Materials* **27**, 5191 (2015).
- [166] M. N. Amini, H. Dixit, R. Saniz, D. Lamoen, and B. Partoens, *Physical Chemistry Chemical Physics* **16**, 2588 (2014).

- [167] A. Bhatia, G. Hautier, T. Nilgianskul, A. Miglio, J. Sun, H. J. Kim, K. H. Kim, S. Chen, G.-M. Rignanese, X. Gonze, and J. Suntivich, *Chemistry of Materials* **28**, 30 (2015).
- [168] B. A. D. Williamson, J. Buckeridge, J. Brown, S. Ansbro, R. G. Palgrave, and D. O. Scanlon, *Chemistry of Materials* **29**, 2402 (2016).
- [169] J. B. Varley, A. Miglio, V.-A. Ha, M. J. van Setten, G.-M. Rignanese, and G. Hautier, *Chemistry of Materials* **29**, 2568 (2017).
- [170] B. A. D. Williamson, G. J. Limburn, G. W. Watson, G. Hyett, and D. O. Scanlon, *Matter* **3**, 759 (2020).
- [171] J. Willis and D. O. Scanlon, *Journal of Materials Chemistry C* **9**, 11995 (2021).
- [172] J. Willis, I. Bravić, R. R. Schnepf, K. N. Heinselman, B. Monserrat, T. Unold, A. Zakutayev, D. O. Scanlon, and A. Crovetto, *Chemical Science* **13**, 5872 (2022).
- [173] A. Crovetto, J. M. Adamczyk, R. R. Schnepf, C. L. Perkins, H. Hempel, S. R. Bauers, E. S. Toberer, A. C. Tamboli, T. Unold, and A. Zakutayev, *Advanced Materials Interfaces* **9**, 2200031 (2022).
- [174] K. Bädeker, *Annalen der Physik* **327**, 749 (1907).
- [175] M. Grundmann, F.-L. Schein, M. Lorenz, T. Böntgen, J. Lenzner, and H. von Wenckstern, *Physica Status Solidi (a)* **210**, 1671 (2013).
- [176] C. Yang, M. Kneiß, M. Lorenz, and M. Grundmann, *Proceedings of the National Academy of Sciences* **113**, 12929 (2016).
- [177] K. Ahn, G. H. Kim, S.-J. Kim, J. Kim, G.-S. Ryu, P. Lee, B. Ryu, J. Y. Cho, Y.-H. Kim, J. Kang, H. Kim, Y.-Y. Noh, and M.-G. Kim, *Chemistry of Materials* **34**, 10517 (2022).
- [178] M. Ferhat, A. Zaoui, M. Certier, J. Dufour, and B. Khelifa, *Materials Science and Engineering: B* **39**, 95 (1996).
- [179] H. Yu, X. Cai, Y. Yang, Z.-H. Wang, and S.-H. Wei, *Computational Materials Science* **203**, 111157 (2022).

- [180] A. Crovetto, H. Hempel, M. Rusu, L. Choubrac, D. Kojda, K. Habicht, and T. Unold, *ACS Applied Materials & Interfaces* **12**, 48741 (2020).
- [181] N. Yamada, R. Ino, and Y. Ninomiya, *Chemistry of Materials* **28**, 4971 (2016).
- [182] W. Peng, L. Li, S. Yu, P. Yang, K. Xu, and W. Luo, *Vacuum* **183**, 109862 (2021).
- [183] A. Vora-ud, K. Chaarmart, W. Kasemsin, S. Boonkirdram, and T. Seetawan, *Physica B: Condensed Matter* **625**, 413527 (2022).
- [184] C.-H. Choi, J. Y. Gorecki, Z. Fang, M. Allen, S. Li, L.-Y. Lin, C.-C. Cheng, and C.-H. Chang, *Journal of Materials Chemistry C* **4**, 10309 (2016).
- [185] P. Storm, M. S. Bar, G. Benndorf, S. Selle, C. Yang, H. von Wenckstern, M. Grundmann, and M. Lorenz, *APL Materials* **8**, 091115 (2020).
- [186] S. Inagaki, M. Nakamura, N. Aizawa, L. C. Peng, X. Z. Yu, Y. Tokura, and M. Kawasaki, *Applied Physics Letters* **116**, 192105 (2020).
- [187] P. Storm, M. S. Bar, S. Selle, H. von Wenckstern, M. Grundmann, and M. Lorenz, *Physica Status Solidi (RRL) – Rapid Research Letters* **15**, 2100214 (2021).
- [188] D. Chen, Y. Wang, Z. Lin, J. Huang, X. Chen, D. Pan, and F. Huang, *Crystal Growth and Design* **10**, 2057 (2010).
- [189] Y. Lv, Z. Xu, L. Ye, Z. Zhang, G. Su, and X. Zhuang, *CrystEngComm* **17**, 862 (2015).
- [190] A. Liu, H. Zhu, W.-T. Park, S.-J. Kim, H. Kim, M.-G. Kim, and Y.-Y. Noh, *Nature Communications* **11**, 4309 (2020).
- [191] T. He, Y. Zhou, P. Yuan, J. Yin, L. Gutiérrez-Arzaluz, S. Chen, J.-X. Wang, S. Thomas, H. N. Alshareef, O. M. Bakr, and O. F. Mohammed, *ACS Energy Letters* **8**, 1362 (2023).
- [192] F.-L. Schein, H. von Wenckstern, and M. Grundmann, *Applied Physics Letters* **102**, <https://doi.org/10.1063/1.4794532> (2013).
- [193] A. Annadi, N. Zhang, D. Boon Kiang Lim, and H. Gong, *ACS Applied Materials & Interfaces* **12**, 6048 (2020).

- [194] J. H. Lee, W.-J. Lee, T. H. Kim, T. Lee, S. Hong, and K. H. Kim, *Journal of Physics: Condensed Matter* **29**, 384004 (2017).
- [195] K. Ding, Q. Hu, D. Chen, Q. Zheng, X. Xue, and F. Huang, *IEEE Electron Device Letters* **33**, 1750 (2012).
- [196] J.-H. Cha and D.-Y. Jung, *ACS Applied Materials & Interfaces* **9**, 43807 (2017).
- [197] C. Yang, M. Kneiß, F.-L. Schein, M. Lorenz, and M. Grundmann, *Scientific Reports* **6**, 21937 (2016).
- [198] A. Liu, H. Zhu, M.-G. Kim, J. Kim, and Y.-Y. Noh, *Advanced Science* **8**, 2100546 (2021).
- [199] D. A. Keen and S. Hull, *Journal of Physics: Condensed Matter* **7**, 5793 (1995).
- [200] C. Moditswe, C. M. Muiva, P. Luhanga, and A. Juma, *Ceramics International* **43**, 5121 (2017).
- [201] S. Ves, D. Glötzel, M. Cardona, and H. Overhof, *Physical Review B* **24**, 3073 (1981).
- [202] A. Blacha, M. Cardona, N. Christensen, S. Ves, and H. Overhof, *Physica B+C* **117-118**, 63 (1983).
- [203] G. Kresse and J. Hafner, *Physical Review B* **47**, 558 (1993).
- [204] G. Kresse and J. Hafner, *Physical Review B* **49**, 14251 (1994).
- [205] G. Kresse and J. Furthmüller, *Computational Materials Science* **6**, 15 (1996).
- [206] G. Kresse and J. Furthmüller, *Physical Review B* **54**, 11169 (1996).
- [207] G. Kresse and D. Joubert, *Physical Review B* **59**, 1758 (1999).
- [208] G. Kresse and J. Hafner, *Journal of Physics: Condensed Matter* **6**, 8245 (1994).
- [209] L. D. Whalley, J. M. Frost, B. J. Morgan, and A. Walsh, *Physical Review B* **99**, 085207 (2019).
- [210] B. Hennion, F. Moussa, B. Prevot, C. Carabatos, and C. Schawb, *Physical Review Letters* **28**, 964 (1972).

- [211] T. Fukumoto, S. Nakashima, K. Tabuchi, and A. Mitsuishi, *Physica Status Solidi (b)* **73**, 341 (1976).
- [212] R. Hanson, J. Hallberg, and C. Schwab, *Applied Physics Letters* **21**, 490 (1972).
- [213] J. M. Skelton, D. S. D. Gunn, S. Metz, and S. C. Parker, *Journal of Chemical Theory and Computation* **16**, 3543 (2020).
- [214] G. Onida, L. Reining, and A. Rubio, *Reviews of modern physics* **74**, 601 (2002).
- [215] Y. Li, J. Sun, and D. J. Singh, *Physical Review Materials* **2**, 035003 (2018).
- [216] F. Meng, J. Ma, J. He, and W. Li, *Physical Review B* **99**, 045201 (2019).
- [217] M. Prasad and S. Gupta, *Physica Status Solidi (a)* **94**, K65 (1986).
- [218] P. Knauth, Y. Massiani, and M. Pasquinelli, *Physica Status Solidi (a)* **165**, 461 (1998).
- [219] C. Yang, D. Souchay, M. Kneiß, M. Bogner, H. M. Wei, M. Lorenz, O. Oeckler, G. Benstetter, Y. Q. Fu, and M. Grundmann, *Nature Communications* **8**, 16076 (2017).
- [220] Z. H. Li, J. X. He, X. H. Lv, L. F. Chi, K. O. Egbo, M.-D. Li, T. Tanaka, Q. X. Guo, K. M. Yu, and C. P. Liu, *Nature Communications* **13**, 6346 (2022).
- [221] K. Matsuzaki, N. Tsunoda, Y. Kumagai, Y. Tang, K. Nomura, F. Oba, and H. Hosono, *Journal of the American Chemical Society* **144**, 16572 (2022).
- [222] M. Almasoudi, A. Saeed, N. Salah, A. Alshahrie, P. M. Z. Hasan, A. Melaibari, and K. Koumoto, *ACS Applied Energy Materials* **5**, 10177 (2022).
- [223] M. Wang, H. Wei, Y. Wu, C. Yang, P. Han, F. Juan, Y. Chen, F. Xu, and B. Cao, *Physica B: Condensed Matter* **573**, 45 (2019).
- [224] O. Madkhali, M. Jullien, A. E. Giba, J. Ghanbaja, S. Mathieu, C. Gendarme, S. Migot, Y. Alajlani, N. Can, F. Alnjiman, D. Horwat, A. Redjaimia, and J. Pierson, *Surfaces and Interfaces* **27**, 101500 (2021).

- [225] D. Ahn, J. D. Song, S. S. Kang, J. Y. Lim, S. H. Yang, S. Ko, S. H. Park, S. J. Park, D. S. Kim, H. J. Chang, and J. Chang, *Scientific Reports* **10**, 3995 (2020).
- [226] J. E. N. Swallow, B. A. D. Williamson, S. Sathasivam, M. Birkett, T. J. Featherstone, P. A. E. Murgatroyd, H. J. Edwards, Z. W. Lebens-Higgins, D. A. Duncan, M. Farnworth, P. Warren, N. Peng, T.-L. Lee, L. F. J. Piper, A. Regoutz, C. J. Carmalt, I. P. Parkin, V. R. Dhanak, D. O. Scanlon, and T. D. Veal, *Materials Horizons* **7**, 236 (2020).
- [227] M. Fukumoto, S. Nakao, K. Shigematsu, D. Ogawa, K. Morikawa, Y. Hirose, and T. Hasegawa, *Scientific Reports* **10**, 6844 (2020).
- [228] A. J. Jackson, B. J. Parrett, J. Willis, A. M. Ganose, W. W. W. Leung, Y. Liu, B. A. D. Williamson, T. K. Kim, M. Hoesch, L. S. I. Veiga, R. Kalra, J. Neu, C. A. Schmittenmaer, T.-L. Lee, A. Regoutz, T.-C. Lee, T. D. Veal, R. G. Palgrave, R. Perry, and D. O. Scanlon, *ACS Energy Letters* **7**, 3807 (2022).
- [229] H.-A. Lee, K. Yatsu, T. I. Kim, H.-I. Kwon, and I.-J. Park, *ACS Applied Materials & Interfaces* **14**, 56416 (2022).
- [230] H. J. Lee, S. Lee, K. H. Lee, and K. Hong, *Journal of Materials Chemistry C* **10**, 7815 (2022).
- [231] S. M. Rozati and S. A. M. Ziabari, *Materials Chemistry and Physics* **292**, 126789 (2022).
- [232] H. Liu, V. Avrutin, N. Izyumskaya, U. Özgür, and H. Morkoç, *Superlattices and Microstructures* **48**, 458 (2010).
- [233] S. Salahuddin, K. Ni, and S. Datta, *Nature Electronics* **1**, 442 (2018).
- [234] Y. Ogo, H. Hiramatsu, K. Nomura, H. Yanagi, T. Kamiya, M. Hirano, and H. Hosono, *Applied Physics Letters* **93**, 032113 (2008).
- [235] H. Zhou, K. Maize, G. Qiu, A. Shakouri, and P. D. Ye, *Applied Physics Letters* **111**, 092102 (2017).
- [236] N. Suzuki, S. Ohira, M. Tanaka, T. Sugawara, K. Nakajima, and T. Shishido, *physica status solidi c* **4**, 2310 (2007).

- [237] S. Ohira, N. Suzuki, N. Arai, M. Tanaka, T. Sugawara, K. Nakajima, and T. Shishido, *Thin Solid Films* **516**, 5763 (2008).
- [238] A. Walsh, D. J. Payne, R. G. Egdel, and G. W. Watson, *Chemical Society Reviews* **40**, 4455 (2011).
- [239] V.-A. Ha, F. Ricci, G.-M. Rignanese, and G. Hautier, *Journal of Materials Chemistry C* **5**, 5772 (2017).
- [240] Y. Hu, D. Schlom, S. Datta, and K. Cho, *Journal of Materials Chemistry C* **11**, 4830 (2023).
- [241] F. Izumi, *Journal of Solid State Chemistry* **38**, 381 (1981).
- [242] H. Giefers, F. Porsch, and G. Wortmann, *Physica Scripta* **2005**, 538 (2005).
- [243] X. Wang, F. Zhang, I. Loa, K. Syassen, M. Hanfland, and Y.-L. Mathis, *physica status solidi (b)* **241**, 3168 (2004).
- [244] W. J. Moore Jr and L. Pauling, *Journal of the American Chemical Society* **63**, 1392 (1941).
- [245] E. P. y Blancá, A. Svane, N. Christensen, C. Rodriguez, O. Cappannini, and M. Moreno, *Physical Review B* **48**, 15712 (1993).
- [246] Q.-J. Liu, Z.-T. Liu, and L.-P. Feng, *Computational Materials Science* **47**, 1016 (2010).
- [247] Y. W. Li, Y. Li, T. Cui, L. J. Zhang, Y. M. Ma, and G. T. Zou, *Journal of Physics: Condensed Matter* **19**, 425230 (2007).
- [248] J. B. Varley, A. Schleife, A. Janotti, and C. G. V. de Walle, *Applied Physics Letters* **103**, 082118 (2013).
- [249] K. Momma and F. Izumi, *Journal of Applied Crystallography* **44**, 1272 (2011).
- [250] L. Diehl, S. Bette, F. Pielnhofer, S. Betzler, I. Moudrakovski, G. A. Ozin, R. Dinnebier, and B. V. Lotsch, *Chemistry of Materials* **30**, 8932 (2018).
- [251] R. Hoppe and B. Nowitzki, *Zeitschrift für anorganische und allgemeine Chemie* **509**, 145 (1984).

- [252] F. Pielnhöfer, L. Diehl, A. Jiménez-Solano, A. Bussmann-Holder, J. C. Schön, and B. V. Lotsch, *APL Materials* **9**, 021103 (2021).
- [253] J.-Y. Kim, B. Bae, and E.-J. Yun, *Science of Advanced Materials* **8**, 272 (2016).
- [254] S. A. Miller, P. Gorai, U. Aydemir, T. O. Mason, V. Stevanović, E. S. Toberer, and G. J. Snyder, *Journal of Materials Chemistry C* **5**, 8854 (2017).
- [255] A. B. Mei, L. Miao, M. J. Wahila, G. Khalsa, Z. Wang, M. Barone, N. J. Schreiber, L. E. Noskin, H. Paik, T. E. Tiwald, Q. Zheng, R. T. Haasch, D. G. Sangiovanni, L. F. J. Piper, and D. G. Schlom, *Physical Review Materials* **3**, 105202 (2019).
- [256] L. Y. Liang, Z. M. Liu, H. T. Cao, and X. Q. Pan, *ACS Applied Materials & Interfaces* **2**, 1060 (2010).
- [257] M. Minohara, A. Samizo, N. Kikuchi, K. K. Bando, Y. Yoshida, and Y. Aiura, *The Journal of Physical Chemistry C* **124**, 1755 (2019).
- [258] M. Minohara, N. Kikuchi, Y. Yoshida, H. Kumigashira, and Y. Aiura, *Journal of Materials Chemistry C* **7**, 6332 (2019).
- [259] M. Budde, P. Mazzolini, J. Feldl, C. Golz, T. Nagata, S. Ueda, G. Hoffmann, F. Hatami, W. T. Masselink, M. Ramsteiner, and O. Bierwagen, *Physical Review Materials* **4**, 10.1103/physrevmaterials.4.124602 (2020).
- [260] Y. Pei, W. Liu, J. Shi, Z. Chen, and G. Wang, *Journal of Electronic Materials* **45**, 5967 (2016).
- [261] J. A. Caraveo-Frescas, P. K. Nayak, H. A. Al-Jawhari, D. B. Granato, U. Schwingenschlögl, and H. N. Alshareef, *ACS Nano* **7**, 5160 (2013).
- [262] P.-J. Chen and H.-T. Jeng, *Scientific reports* **5**, 16359 (2015).
- [263] X. Gong, H. Li, N. Zou, R. Xu, W. Duan, and Y. Xu, *Nature Communications* **14**, 2848 (2023).
- [264] Y. Zhong, Z. Tao, W. Chu, X. Gong, and H. Xiang, *Accelerating the calculation of electron-phonon coupling by machine learning methods* (2023).

- [265] S. Sharifzadeh, A. Haldar, Q. Clark, M. Zacharias, and F. Giustino, Machine learning electron-phonon interactions in 2d materials (2023).
- [266] D. G. Shankland, *Int. J. Quantum Chem.* **5**, 497 (1971).
- [267] R. N. Euwema, D. J. Stukel, T. C. Collins, J. S. DeWitt, and D. G. Shankland, *Phys. Rev.* **178**, 1419 (1969).
- [268] D. D. Koelling and J. H. Wood, *J. Comput. Phys.* **67**, 253 (1986).
- [269] J. P. Perdew, K. Burke, and M. Ernzerhof, *Physical Review Letters* **77**, 3865 (1996).
- [270] S. P. Ong, W. D. Richards, A. Jain, G. Hautier, M. Kocher, S. Cholia, D. Gunter, V. L. Chevrier, K. A. Persson, and G. Ceder, *Computational Materials Science* **68**, 314 (2013).
- [271] X. Gonze, F. Jollet, F. A. Araujo, D. Adams, B. Amadon, T. Applencourt, C. Audouze, J.-M. Beuken, J. Bieder, A. Bokhanchuk, E. Bousquet, F. Bruneval, D. Caliste, M. Côté, F. Dahm, F. D. Pieve, M. Delaveau, M. D. Gennaro, B. Dorado, C. Espejo, G. Geneste, L. Genovese, A. Gerossier, M. Giantomassi, Y. Gillet, D. Hamann, L. He, G. Jomard, J. L. Janssen, S. L. Roux, A. Levitt, A. Lherbier, F. Liu, I. Lukačević, A. Martin, C. Martins, M. Oliveira, S. Poncé, Y. Pouillon, T. Rangel, G.-M. Rignanese, A. Romero, B. Rousseau, O. Rubel, A. Shukri, M. Stankovski, M. Torrent, M. V. Setten, B. V. Troeye, M. Verstraete, D. Waroquiers, J. Wiktor, B. Xu, A. Zhou, and J. Zwanziger, *Computer Physics Communications* **205**, 106 (2016).
- [272] J. P. Perdew, A. Ruzsinszky, G. I. Csonka, O. A. Vydrov, G. E. Scuseria, L. A. Constantin, X. Zhou, and K. Burke, *Physical Review Letters* **100**, 136406 (2008).
- [273] A. M. Ganose, A. J. Jackson, and D. O. Scanlon, *Journal of Open Source Software* **3**, 717 (2018).